

Suspension phased injection in pulsed arc jet

Introduction

The following chapter focuses on the improvement of suspension plasma spraying method. The principle is to inject the suspension droplets at the right moment in the cycle of the periodic plasma jet oscillations.

The previous chapter has shown the possibility to obtain very regular plasma oscillations. A new dc torch has been designed with a larger cathode cavity ($V_g = 17.8 \text{ cm}^3$) to reinforce the Q factor and to decrease the specific frequency of the Helmholtz mode. Moreover, the use of nitrogen as plasma forming gas has allowed to reinforce the Helmholtz and dominate the acoustic modes. The presented experiments have highlighted the possibility of coupling the Helmholtz with restrike oscillations into a new resonant mode, which has been called "mosquito" mode. The arc voltage signal, produced in this "mosquito" mode, is a very repeatable saw-tooth shape signal. Moreover, the thermal losses determination has allowed to define the local specific enthalpy of different moments of this periodic plasma oscillations. The calculations have highlighted that the obtained plasma is characterized by the enthalpy modulated with a ratio $h_{\max}/h_{\min} \simeq 18$.

The following chapter will present the application of these regular plasma oscillations to the suspension treatment and coatings deposition process. As has been highlighted in the previous chapters, the conventional SPS method demonstrates the difficulties due to e.g. the discrepancies in the particles trajectories and the heat transfers, what makes the control of coatings properties more difficult to achieve. The purpose of this work is to develop a new system which may allow to increase the reproducibility and reliability of the process by the use of the regular plasma oscillations synchronized with the suspension injection. The activation of the suspension droplet emission at the chosen moment of the periodic plasma, following the requirements for the thermal treatment of the particular material, may be able to increase the control of the heat and momentum transfers between plasma and materials, thus, of the coatings properties. Therefore, it is important to optimize the system which will allow to synchronize the suspension injection with the arc voltage signal. Moreover, the different kinds of the time-resolved and synchronized diagnostic methods are required to study the thermal and dynamic treatments of the material in the periodic plasma. Consequently, the system schematically presented in Figure 3.1 has been developed in the framework of this thesis to work with this periodic plasma produced in "Mosquito" mode.

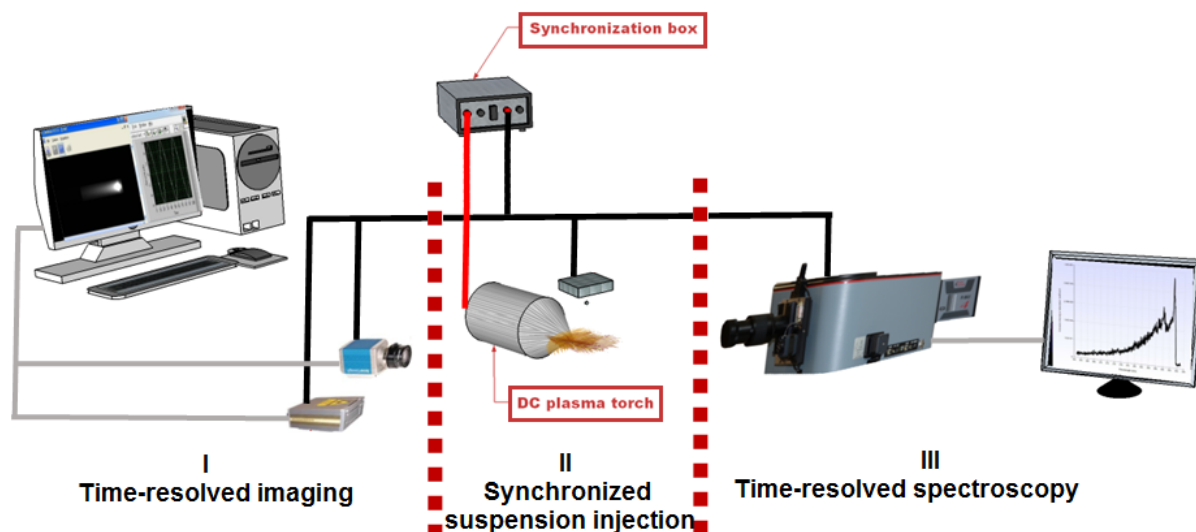


Figure 3.1: Schematic view of the experimental setup.

It consists of three important parts:

I Time-resolved imaging system

It consists of the camera and the laser. This part of the system requires the choice of the devices suitable to observe and register the oscillating plasma with the periods of around $700 \mu\text{s}$. Moreover, the experiments have to be performed to obtain the synchronization of the camera with the laser.

II Synchronized suspension injection

The periodic plasma oscillations allow to obtain a new approach to the injection of reactive material in the arc jet. The suspension droplet can be inserted at the chosen moment of this regular plasma jet, what may lead to the control of dynamic and thermal interaction between the plasma and the material. However, it requires the injection system capable to control the moment of material introduction to the plasma. This requirement has been found in the piezoelectric-based DOD (Drop-On-Demand) ink-jet printer provided by Ceradrop Company (Limoges, France). In the paragraph devoted to this part of the system a new injector will be described. Moreover, the observation of the suspension droplets without the plasma and inside the plasma jet will be presented.

III Time-resolved spectroscopy

Chapter 2 has highlighted that the plasma produced in "Mosquito" mode is characterized by the enthalpy highly modulated. To experimentally determine this estimation the time-resolved optical emission spectroscopy has been implemented in the system. This method has been used to make the measurements of the plasma temperature and to determine the plasma species. However, this technique requires

careful calibration methods, what will be presented with the first spectroscopic measurements of the periodic plasma.

The principle of this new system is to inject the suspension droplet at the right moment of the periodic plasma jet. Therefore, the emission of the feeding material has to be synchronized with the arc voltage signal. Moreover, to observe the modulated plasma and the interaction between the plasma and the injected suspension the time-resolved imaging system and time-resolved optical emission spectroscopy have to be also synchronized with the plasma.

Consequently, the synchronization system has been implemented in the framework of this thesis, what will be described in the following paragraphs.

All assumptions and characterization given above have been used to construct a new system which may be an alternative method to the conventional suspension plasma spraying method. To determine the possibilities of this new technique the first attempts of the material deposition have been performed, what will be presented in the final part of this chapter.

I Time-resolved imaging system

To observe the periodic plasma oscillations obtained in "mosquito" mode the time-resolved and synchronous imaging system has been implemented. The study of the oscillating plasma with the periods of around $700 \mu s$ is possible by the choice of the fast shutter camera.

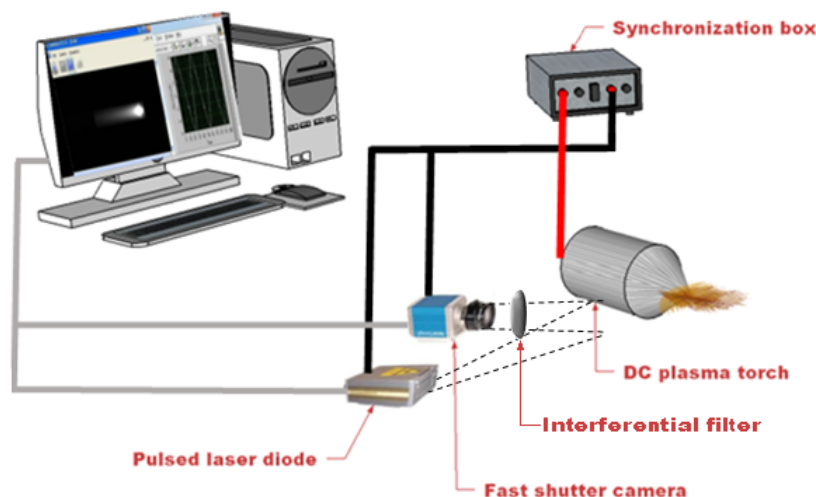


Figure 3.2: Schematic view of the experimental setup of time-resolved imaging system.

The time-resolved imaging system is presented in Figure 3.2. It consists of a fast shutter camera, high-power laser diode and an interferential filter (801 nm). The laser and the filter have been combined with the fast shutter camera to permit the observation of the suspension treatment within the plasma jet. The principle is to observe the suspension penetration within the plasma jet by illuminating droplets using the laser shots. The interferential filter (801 nm) centered on the laser wavelength permits to eliminate on the image the light coming from the pure nitrogen plasma.

I.1 Camera

Fast shutter camera Pixelfly (PCO, Germany) can be applied in many scientific areas, e.g. luminescence spectroscopy, particle image velocimetry (PIV), high resolution microscopy. The camera is equipped with the CCD matrix with the high resolution of 1392 x 1040 pixels, what enables to observe the details of the suspension droplet. Pixelfly camera can work in three operation modes: async (asynchronous) mode, double/shutter mode, video mode. In order to synchronize the camera with the laser the async mode has been used, which enables to control the CCD matrix exposure time in the range from 5 μ s to 65 ms. The functioning of CCD can be divided into two phases: exposure and readout. During the first phase (CCD-Exposure in Figure 3.3) the CCD collects passively incoming photons and stores electrons in its cells. After the exposure time, the cells are read out one line at a time (CCD-Readout in Figure 3.3) and are shifted down the entire area of the CCD matrix.

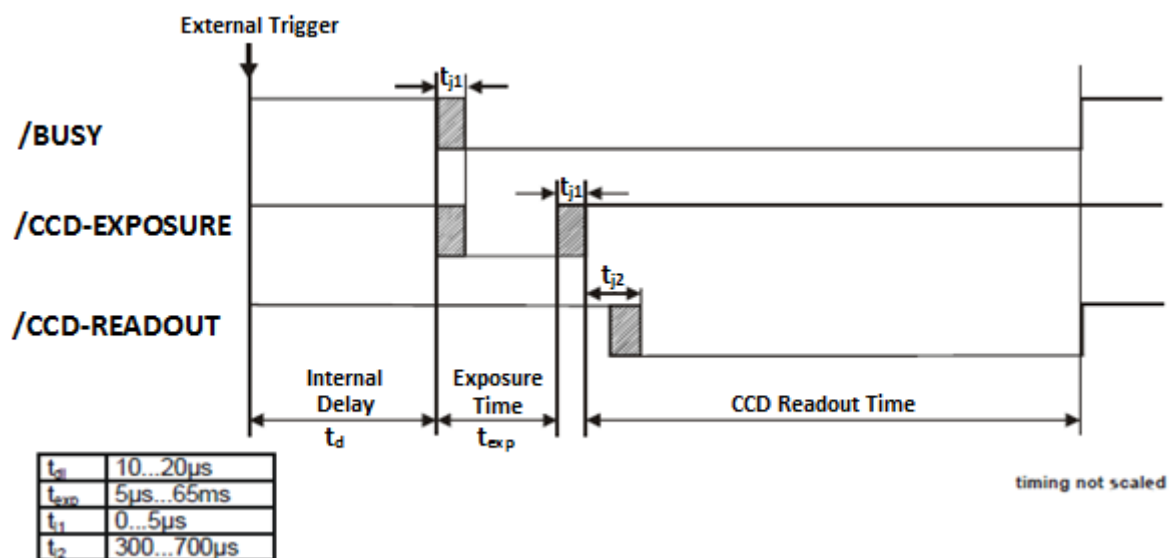


Figure 3.3: Timing diagram of the async mode.

Camera Pixelfly is connected via USB 2.0 connector to computer and controlled by program Camware. This software allows to trigger the camera by the internal or external signal. In the case of the time-resolved imaging the second option has been chosen. Camware enables also to record images, save one image which is displayed in the active window or save the sequence of 75 images which is useful in the observation of the plasma jet.

To study the plasma with higher resolution, e.g. to record the treatment of suspension droplets inside the plasma jet, the Infinimax long-distance microscope system (Infinity, Boulder, USA) has been used. It consists of the objective and large format amplifier which can be additionally mounted. The use of the objective results in the increase of magnification up to 2.9x. The optional amplifier extends the magnification, what is highlighted in Figure 3.4.

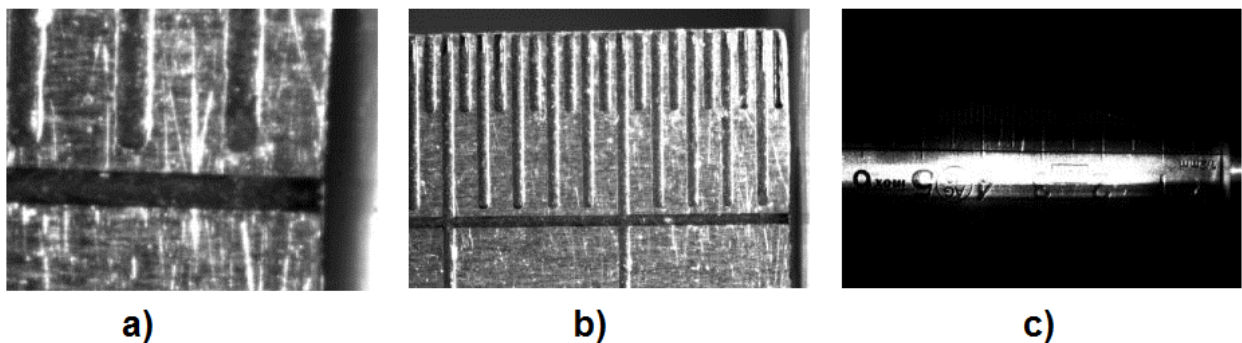


Figure 3.4: Pictures taken by Pixelfly camera at different magnifications with mounted a) Infinimax and the amplifier, b) Infinimax objective, c) Pixelfly camera synchronized with the laser sheet.

Figure 3.4 a) has been taken by the camera Pixelfly with the mounted Infinimax and the amplifier. It is possible to observe a magnified object at the distance of 3 mm from the torch nozzle. In Figure 3.4 b) the result of using the camera with Infinimax objective is shown where the magnification decreases. The distance from the torch equals 22 mm. The last figure, 3.4 c), presents the picture taken by the camera Pixelfly. The magnification decreases 2.9 times compared to the figure b). Figure 3.4 c) presents also the use of the laser synchronized with the camera.

I.2 Laser

High power laser diode (HiWatch, Oseir, Finland) is designed for demanding illumination applications. The parameters of this laser unit are presented in Table 3.1.

Table 3.1: Parameters of a laser diode.

Parameter	Value
Emission wavelength	801 ± 2 nm
Output geometry	8 x 1 mm
Emission power	50 W
Single pulse length	0.025-1 μ s
Max. pulse frequency	20 MHz
Time delay	36 ns

The emission wavelength of the laser is in the range of 801 ± 2 nm which corresponds to the infra-red (IR) spectral region. The response time of the laser diode is negligible and equals 36 ns. The HiWatch laser is controlled by a driver module, presented in Figure 3.5.

The diode is energized when the MOSFET transistor is turned on by the signal sent to the gate input. The current flows from the energy storage capacitor, through the laser diode, current limiting resistor, MOSFET and the current sense resistor, back to the energy storage capacitor. The output pulse width and frequency follow the signal which is directed to input gate. The driver provides variable output current from 5A to 50A with pulse widths up to 1 μ s and frequencies up to 1MHz.

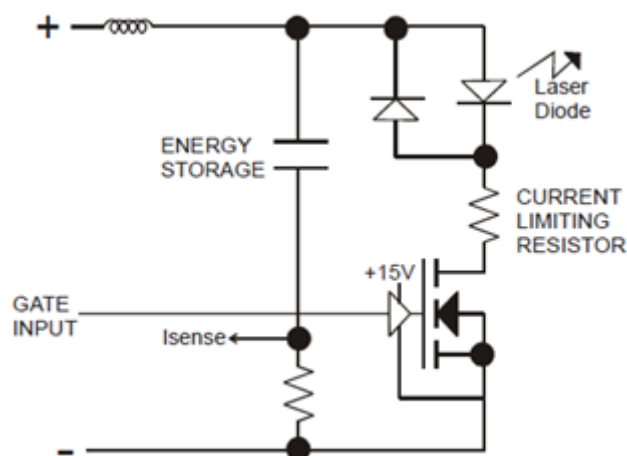


Figure 3.5: Diagram of power supply module of the laser diode.

The width of the pulse emitted by the laser depends mainly on the width of signal put to the input gate. It is possible to obtain 50 ns laser pulse by providing 50 ns input to the driver module. The width of pulse transmitted to the input gate should be smaller than

1 μ s due to recharging of the energy storage capacitor (Figure 3.5). It is also possible to input any binary waveform which will be replicated in the emission. In this case, it is important to take into consideration the dependence presented in Figure 3.6.

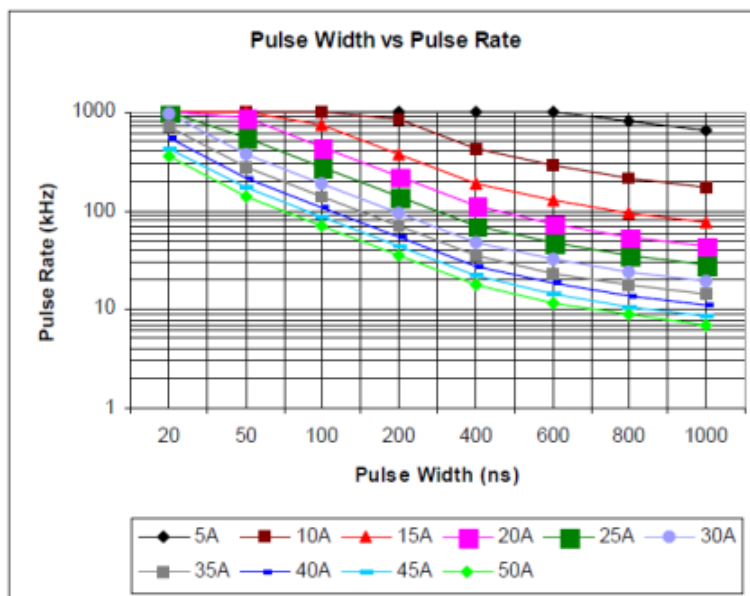


Figure 3.6: Dependence of the pulse width, pulse rate and current.

The pulse width, frequency and the driver output current (therefore the power emitted by the laser diode) are the dependent parameters, related to the available charge of the drivers energy storage network. This dependence shows that in the time-revolved imaging method, it is important to choose an appropriate value of the pulse rate for the synchronization of the camera and the laser.

I.3 Synchronization procedure of time-resolved imaging system

To observe different moments of the periodic plasma oscillations the time-resolved imaging should be synchronized with the arc voltage signal. Moreover, the suspension droplets should be illuminated by the laser shot during the registration by the camera. Therefore, the laser and the camera should be also synchronized.

To make the synchronization of the laser diode with the fast shutter camera the accurate time delay, t_d , of each device has to be determined. t_d is defined as the time between sending the external trigger signal to the instrument and the response of this instrument. The time delay of the laser has been determined by the producer and equal to 36 ns. However, the t_d of the camera has been given in the range between 10 μ s and 20 μ s. The laser pulse duration equals up to 1 μ s. Therefore, it can be noticed that the precise time of the camera delay is the important parameter in the synchronization procedure.

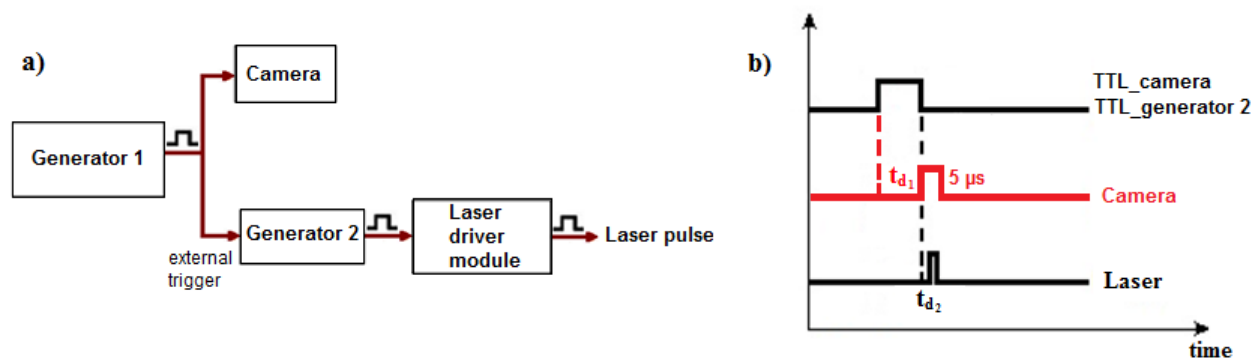


Figure 3.7: Investigation method of the camera delay time: a) the experimental setup, b) the timing diagram.

Figure 3.7 presents the investigation procedure to determine the delay time of the camera, t_{d1} . The principle is to synchronize the camera with the laser by using two generators. Generator #1, Figure 3.7, sends the triggering signal to the camera and the generator #2. The pulse reaches both devices at the same time, what is measured by the oscilloscope. The camera is triggered by a rising edge of the signal and the generator #2 by a falling edge. The generator #2 inputs the pulse to TRIG connector of the laser diode driver module, what results in the emission of the laser shot. t_{d2} is the laser time delay equals 36 ns. It has to be mentioned that the camera is controlled by Camware software and the option of the external trigger of the camera has been chosen.

The exposure time of the camera is regulated to minimal value of 5 μs. The width of the trigger pulse sent by the generator #1 simulates the time delay of the camera. The camera has been recording the image for different widths of the signal in the range of 10 to 20 μs. The width of the trigger pulse for which the image of the laser beam has been obtained using camera is 14 μs, what is in the range of camera delay time given by the producer.

As has been mentioned, the time-resolved imaging system has to be synchronized with the arc voltage. To obtain this synchronization the TTL signal has to be formed from the arc voltage, which is measured by the bridge circuit connected between the cathode of the torch and the ground.

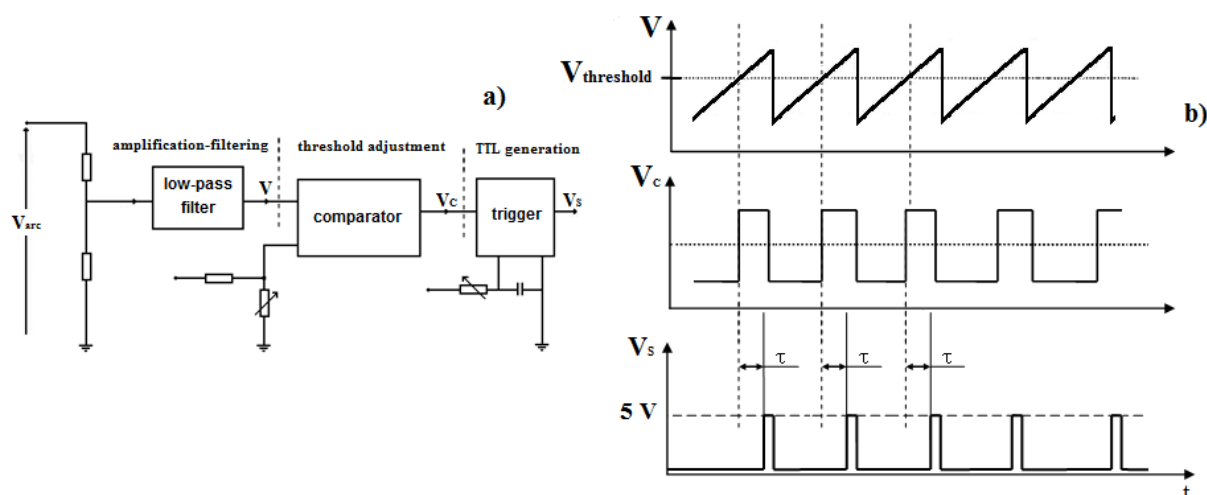


Figure 3.8: The principle of the synchronization device: a) the schematic view, b) the functioning of the system.

To generate the initial TTL signal the synchronization device has been designed, which is presented in Figure 3.8, and composed of:

- the amplification-filtering unit to isolate the Helmholtz mode component from the raw signal, V_{arc} ,
- the threshold adjustment unit which consists of the comparator to set the trigger level, $V_{threshold}$,
- the generation of the pulse at the fundamental frequency, f_H , unit which produces a TTL pulse V_s (5 V , $10\ \mu\text{s}$). It permits to generate the signal with an adjustable delay, τ , relative to the threshold

TTL signal, generated by this synchronization box by the adjustment of the threshold level and the time delay, is then sent to the control panel (Ceradrop, France), Console Ceradrop presented in Figure 3.9.

The Ceradrop console can generate two trigger signals (Output #1 to activate the camera and Output #2 connected to the laser in 3.9) with the adjustable pulse width. The console permits to change the time delay relative to Triggering signal, in Figure 3.9, formed from the arc voltage by using the synchronization box. Moreover, it is possible to choose the time delay between two triggering signals from output 1 and output 2 to synchronize the camera with the laser sheet. The results of the experiments have shown that the delay between these two devices equals $14\ \mu\text{s}$. Therefore, the time between the triggering signals of output 1 and output 2 is regulated to this value. The developed synchronization system permits to select the moment of the periodic arc voltage signal by changing the threshold level and the time delay.

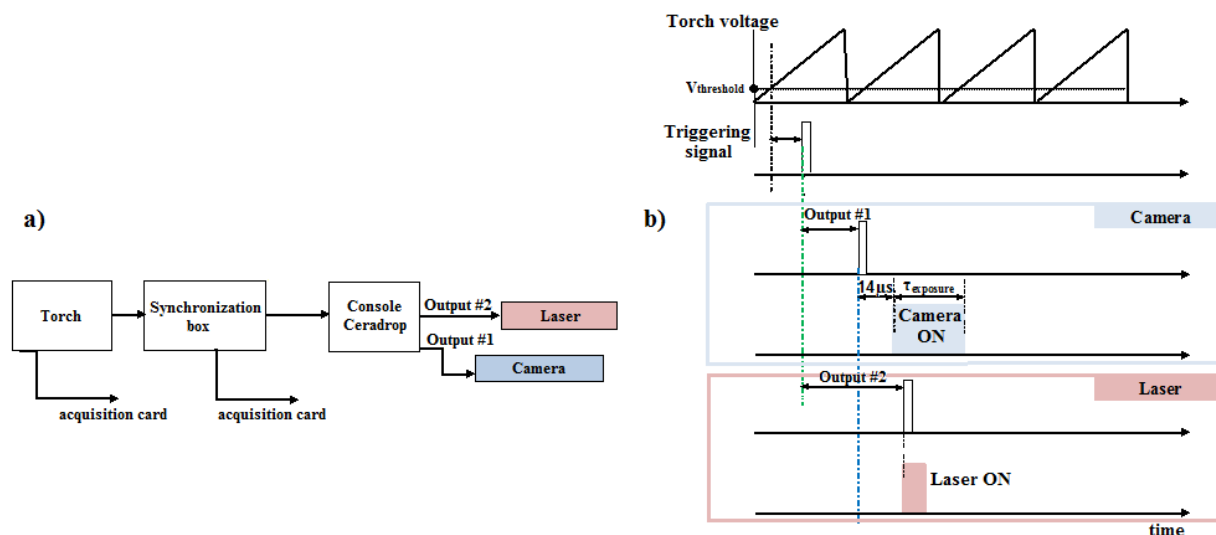


Figure 3.9: Schematic view of the synchronous time-resolved imaging procedure: a) the experimental setup, b) the timing diagram.

The obtained TTL signal triggers the Ceradrop console which after 14 μs activates the camera and the laser.

I.4 Pulsed and laminar plasma jet

The time-resolved imaging system synchronized with the arc voltage signal allows to observe the different moments of the periodic plasma oscillations. As has been presented, Helmholtz and restrike modes locked together oscillate at the frequency of 1.4 kHz. Therefore, one period of the plasma oscillation is around 700 μs , what can be observed in Figure 3.10. It presents time-resolved imaging of this periodic plasma obtained in "mosquito" mode.

As can be noticed this very regular arc voltage signal obtained by coupling Helmholtz and restrike modes together, presented in Figure 2.37 c), results in the pulsed plasma jet. The different pulses of this periodic plasma are able to be observed by the camera triggered at a given moment of this periodic arc voltage signal. Figure 3.10 presents the voltage signal obtained in "mosquito" mode with indicated TTL pulses sent to the camera. The aperture time of the camera is regulated at 60 μs and 75 pictures are recorded in each situation: from a) to e) in Figure 3.10. The picture a) corresponds to a trigger of 70 μs after a falling front of the voltage. The moments b) to e) have been taken with respective time delays: 210, 310, 520 and 770 μs , which corresponds to 70 μs in the next period, taking into account that one period of the pulsed plasma jet is around 700 μs . Figure 3.10 a) presents the moment after re-arcing and shows an extinguishing plasma ball. The arc is very short and located in the rear part of the nozzle.

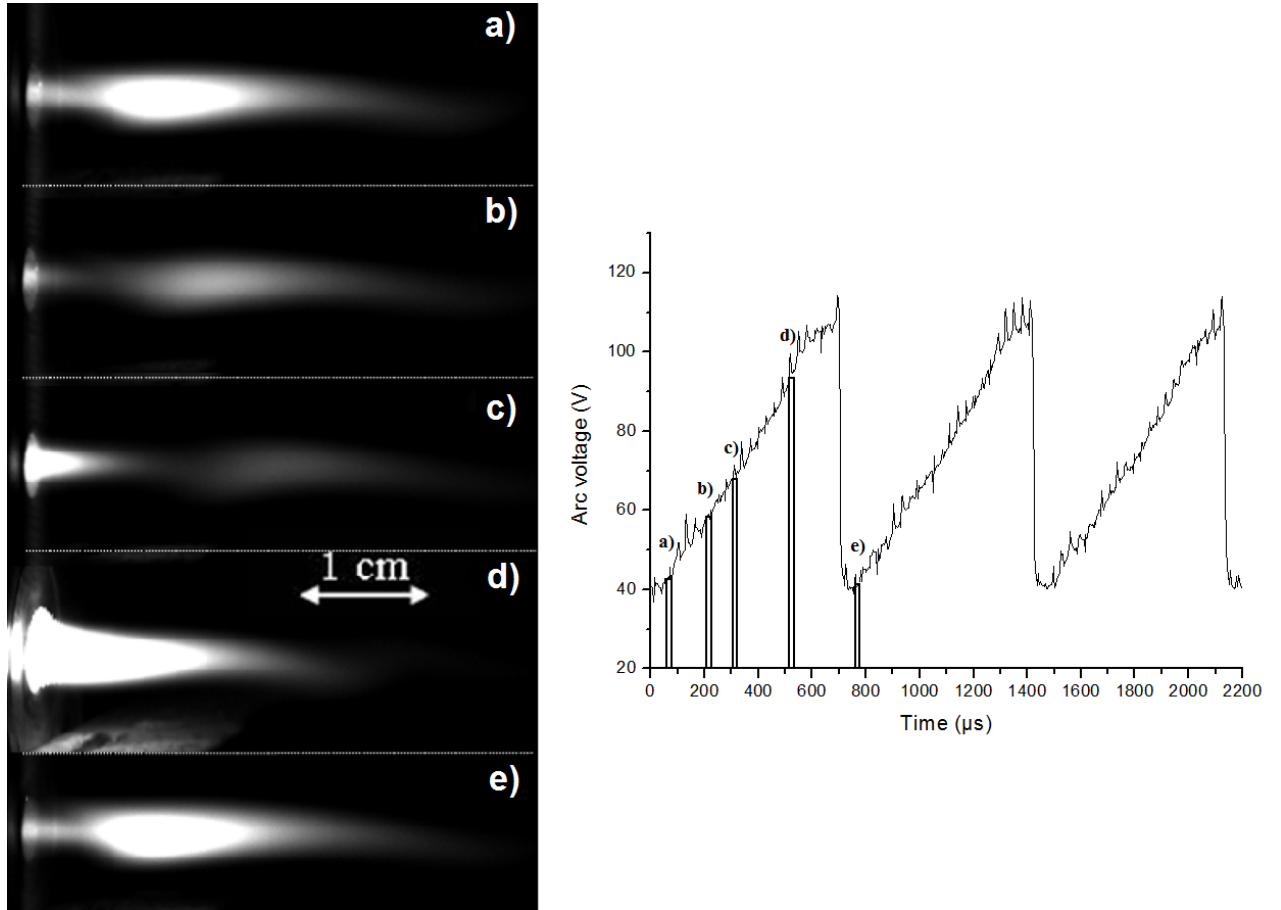


Figure 3.10: Time-resolved imaging (camera exposure time: $60 \mu\text{s}$) of pulsed arc jets for different trigger time delays indicated in the temporal evolution of the arc voltage signal: (a) $70 \mu\text{s}$, (b) $210 \mu\text{s}$, (c) $310 \mu\text{s}$, (d) $520 \mu\text{s}$ and (e) $70 \mu\text{s}$ in the next period, $700 \mu\text{s}$ after (a) [79].

Pictures b) - d) demonstrate the progressive development of the arc and Figure 3.10 e) represents a situation similar to a) but for the following cycle. This sequence testifies the strong modulation of the plasma, which from high luminescence appears to be almost lighted off. The examination of the series of 75 pictures has shown a very regular evolution of the plasma in each cycle.

Figure 3.11 is obtained by a standard camera with an exposure time of 10^{-2} s, what results in the superposition of 13 cycles presented in Figure 3.10. It shows the laminar feature of the plasma flow, what can be experimentally verified by the Reynolds number, defined for the plasma torch in [80], as follows:

$$Re = \frac{4\dot{m}}{\pi\eta d} \quad (3.1)$$

where η is the dynamic viscosity of the plasma equals around $1.7 \times 10^{-4} \text{ kg}\cdot\text{m}^{-1}\cdot\text{s}^{-1}$, what has been defined from the energy balance measurements and data found in [17].



Figure 3.11: Laminar feature of pulsed arc jet. Operating parameters: $d_{\text{nozzle}} = 4 \text{ mm}$, $I = 15 \text{ A}$, $N_2: 0.042 \text{ g.s}^{-1}$, $\bar{U} = 73.7 \text{ V}$, exposure time of camera = 10^{-2} s , the superposition of 13 cycles presented in Figure 3.10 [74].

Reynolds number allows defining different flow regimes, such as laminar or turbulent flow. The laminar flow occurs at low Reynolds numbers. The transition from laminar to turbulent flow starts at about $Re > 2100$ and the flow is considered to become fully turbulent at $Re > 4000$.

For plasma parameters, given in Table 2.12, Reynolds number is estimated to approximately 78, what defines the laminar flow of the plasma.

II Synchronized suspension injection

In the introduction to this chapter has been highlighted that the obtained periodic plasma oscillations require the appropriate injection method, capable to control the moment of material introduction to the plasma jet. The analysis of different injection techniques, presented in the literature review in chapter 1, has resulted in selecting the piezoelectric-based DOD ink-jet printer, provided by Ceradrop Company (Limoges, France), due to the possibility of the emission of each droplet triggered at the frequency of the pulsed plasma, i.e. 1.4 kHz. The following paragraph describes this new injector. Moreover, the idea of development of the plasma spraying method is to insert the material at the chosen moment of the pulsed plasma jet, presented above.

Therefore, the synchronization of the suspension injection with the arc voltage signal has to be implemented in this method. Figure 3.12 shows the schematic view of the developed system with added suspension injection. This experimental setup allows to obtain the synchronization of the material insertion to chosen moment of the plasma jet with the camera and the laser. It results in the possibility of the observation of the suspension-plasma interaction, what will be presented in the following paragraphs.

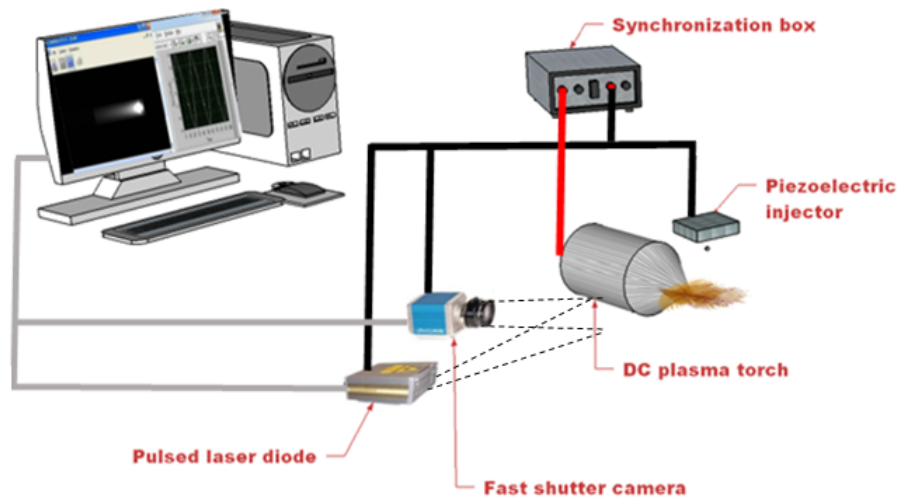


Figure 3.12: Schematic view of the experimental setup with added synchronized suspension injection.

II.1 Injection system

This ink-jet type technique, commonly applied in the printing devices, is now being used in a wide variety of industries for micro-droplet generation [81–83]. In the system developed in this thesis the injector prepared by Ceradrop Company (Limoges, France) has been used. Figure 3.13 schematically presents the injector based on drop-on-demand technique. The liquid is ejected out of small orifices (diameter equal to $50\mu\text{m}$) to form pulsed jets due to the pressure generated by a voltage pulse driven piezoelectric actuator (voltage excitation equals 120 V).

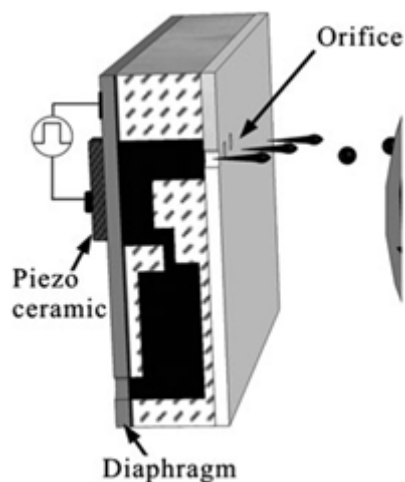


Figure 3.13: Schematic view of piezoelectric DOD printhead [39].

It has to be mentioned that voltage pulses are carefully shaped to avoid satellite droplets and to adjust the velocity of single calibrated droplet between 2 and 10 m.s⁻¹. The pulse shape must also be adapted to the rheological properties of the suspension, what will be presented in the following paragraphs. The piezoelectric injector can be triggered at frequencies up to 20 kHz and comprises a ramp of 128 individual micro-nozzles, disposed perpendicular to the plasma jet axis, with a step of 0.5 mm. The injection system is protected from heat flux coming from the plasma by a water-cooled copper screen, presented in Figure 3.14, in which a horizontal slit, 10 mm long and 1 mm wide, is machined.

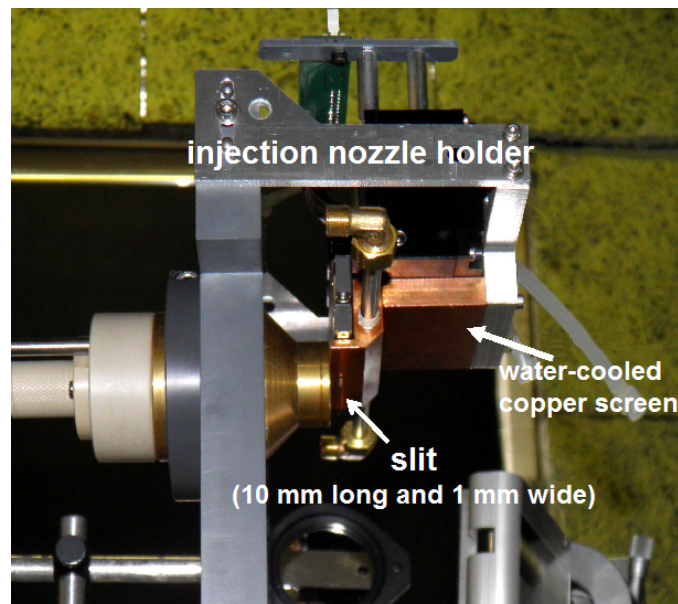


Figure 3.14: "Mosquitorch", a newly designed dc plasma torch, with a water-cooled copper screen.

II.2 Synchronization system

The principle of synchronous suspension injection is to inject the droplet of the feeding material at the right moment of the periodic plasma jet oscillations. This synchronization process is possible for the following postulate:

$$f_H = f_i \quad (3.2)$$

where:

- f_H is the frequency of Helmholtz resonant mode equals the plasma frequency,
- f_i the frequency of suspension injection.

Figure 3.15 presents the schematic view of the synchronous suspension injection system. The emission of the droplet is triggered by the TTL signal formed from the arc voltage by using the synchronization box. This triggering pulse is sent to Ceradrop console which activates the piezoelectric injector.

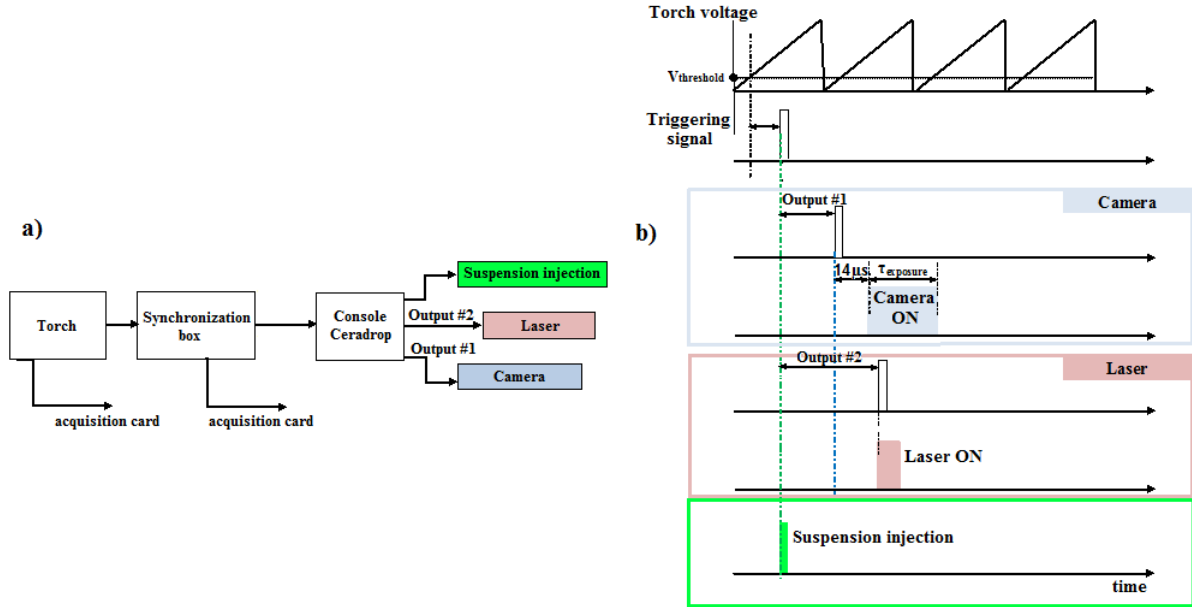


Figure 3.15: Schematic view of the synchronous injection procedure: a) the experimental setup, b) the timing diagram.

The system permits to select the moment at which the suspension droplet is injected to the pulsed plasma jet by using the function of the time delay in the synchronization box. It results in the suspension emission after an adjustable delay, $\tau_{droplet}$, counted after a falling front of the arc voltage signal, as follows:

$$\tau_{droplet} = nT + \tau_j \quad (3.3)$$

where T is the arc voltage period and τ_j is the time at which a droplet penetrates the plasma.

As presented in Figure 3.15 the triggerring signal generated from the arc voltage activates all outputs of Ceradrop console, what permits to obtain the synchronization of the suspension injection with the camera and the laser shot. In the Ceradrop console it is possible to choose the time delay of the outputs 1 and 2 in relation to the triggerring signal and the suspension injection as well. To observe the suspension-plasma interaction the delay time has been regulated to 0 s.

II.3 Observation of the suspension droplets without the plasma

II.3.1 Suspension properties and size distribution

The suspension used in the experiments, prepared by Ceradrop Company (Limoges, France), is composed of titanium dioxide (90% TiO₂ rutile phase) powder and it consists of 5 wt% of powder and 95 wt% of water. The properties of the suspension are specified in Table 3.2.

Table 3.2: Parameters of the suspension.

TiO ₂ concentration vol%	Conductivity $\mu\text{S}\cdot\text{cm}^{-1}$	Viscosity mPa.s	Surface tension mN.m ⁻¹	Density g.cm ⁻³
5	480	7.57	34.067	1.204

The particle size distribution of the injected feedstock material has to be adjusted with the diameter of the printing head nozzle, which equals 50 μm in Ceradrop injector. To avoid the clogging of the nozzle the particles sizes of the suspension have to be analyzed.

They have been determined by using Mastersizer 2000 (Malvern Instruments Ltd., UK) which is based on the technique of laser diffraction. The scattering pattern in this method depends on the ratio of particle diameter, D , and the wavelength of the incident light, λ . According to D/λ the scattering of particles is predicted by the Fraunhofer or Mie models. In Mastersizer 2000 the Mie model ($D/\lambda \simeq 1$) is applied for the particles smaller than 3 μm . Therefore, this model has been used to determine the particle size distribution of the suspension, presented in Figure 3.16.

The peak of the particle size distribution curve is centered on 66 nm (d_{50}). The dispersion size ($d_{90} - d_{10}$) is equal to 48 nm.

II.3.2 Trajectory of a single droplet

In the ink jet printers, the suspension formulation has to be optimized in order to avoid the sedimentation, clogging and to be compatible with the printing head. Moreover, the injection of a single calibrated droplet is the important parameter in this kind of method. To obtain the emission of a single droplet two conditions have to be fulfilled:

- the rheological properties of the suspension (e.g. viscosity, surface tension) have to be adjusted to obtain the ratio $\text{Re}/\sqrt{\text{We}}$ ranged between 1 and 10
- the voltage driven pulse sent to the piezoelectric injector has to be optimized

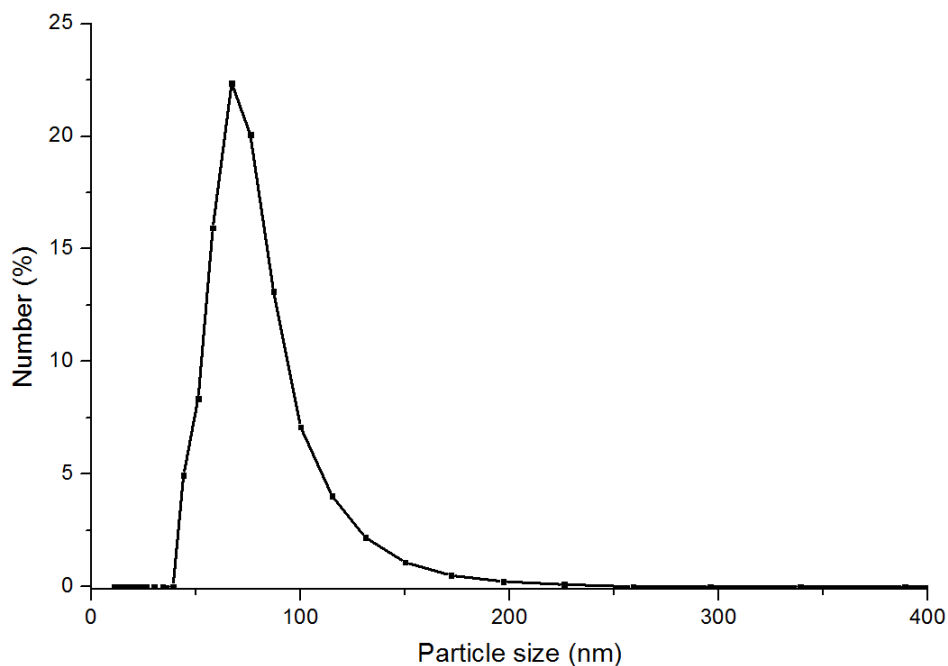


Figure 3.16: The particle size distribution of TiO₂ suspension.

The first condition requires the definition of the ratio Re/\sqrt{We} . It is the dimensionless number which enables to analyze the fluid flows. It consists of respectively Reynolds and Weber numbers, defined by the following equations:

$$Re = \frac{v.r.\rho}{\eta} \quad (3.4)$$

where:

v is the suspension velocity,
 r the radius of the nozzle,
 ρ the suspension density,
 η the suspension viscosity.

and Weber number, obtained by:

$$We = \frac{v^2.r.\rho}{\sigma} \quad (3.5)$$

where:

σ is the suspension surface tension.

Noguera *et al.* have shown the different cases of the suspension injection observed according to the value of ratio Re/\sqrt{We} , presented in Figure 3.17.

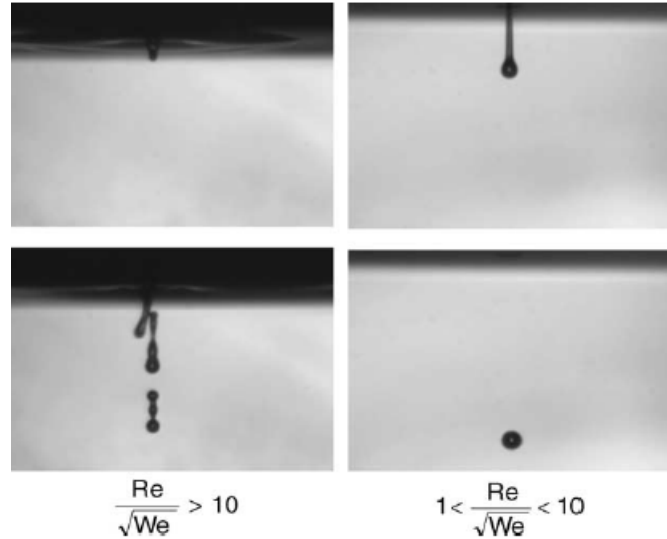


Figure 3.17: Effect of the ratio Re/\sqrt{We} on the suspension injection [81].

When the ratio Re/\sqrt{We} is too high, bigger than 10, a continuous column of the suspension is injected, what is not the purpose of this thesis.

The properties of the suspension used in the experiment, presented in Table 3.2, have been optimized to obtain the ratio equals:

$$\frac{Re}{\sqrt{We}} = 5.98 \quad (3.6)$$

It is one of the condition to obtain the emission of a single droplet. Figure 3.18 presents the suspension droplets before a) and after b) the optimization of the injection parameters.

To eliminate satellite droplets the voltage driving pulse has been optimized in collaboration with Ceradrop. A voltage trapezoidal pulse, shown in Figure 3.19, has been applied.

The magnitude of the voltage (V_{max}), the pulse times, which include the rise time, duration time and fall time (respectively τ_1 , τ_2 and τ_3 in Figure 3.19) and the frequency have been defined and sent to the controller. During the rising time (τ_1) the piezoelectric material (PZT: lead zirconate titanate) moves inward due to shearing stress by applying an electric field in the direction perpendicular to the polarization direction of the piezoelectric material. It results in positive pressure for the liquid in the chamber.

The PZT has no deformation during τ_2 . As the voltage drops from V_{max} to 0 during τ_3 , the piezoelectric material moves outward, what results in the generation of a negative pressure in the liquid of the chamber. The appropriate optimization of these parameters is important in the injection process since the liquid column is ejected by the positive pressure and then the break-up into droplets by the negative pressure.

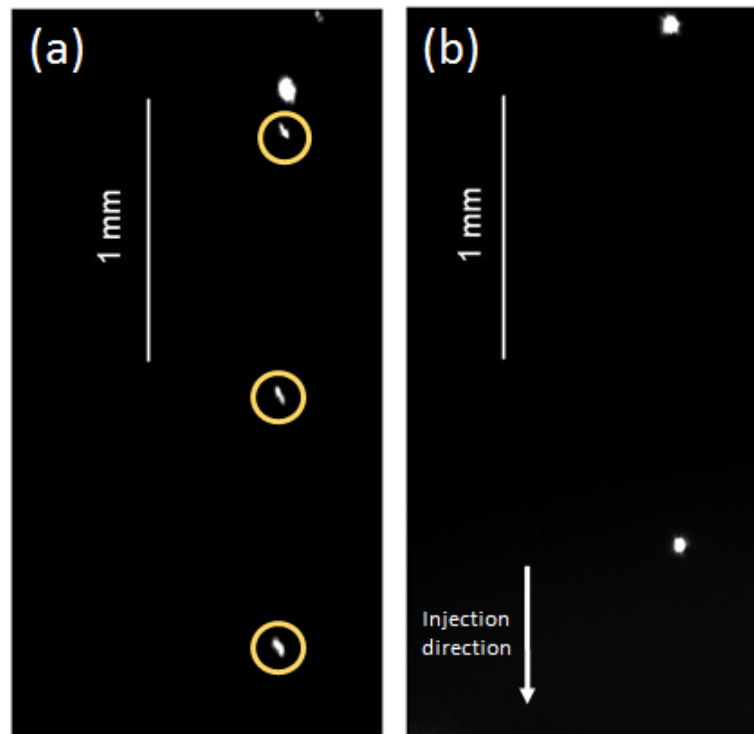


Figure 3.18: Observation of droplets injection by the camera and laser illumination: a) satellite droplets marked by the circles, b) single drops with no satellites as the result of correctly optimized parameters.

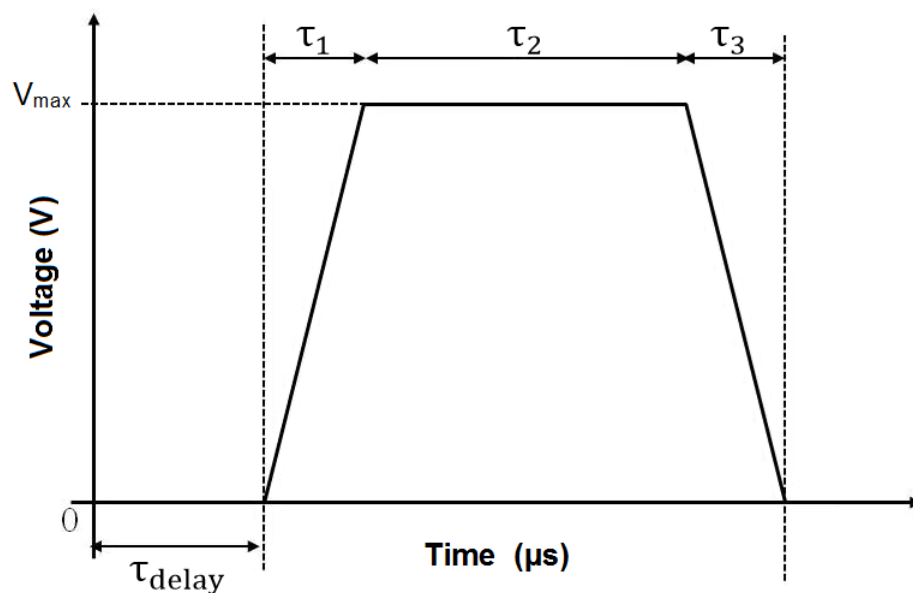


Figure 3.19: Form of the voltage pulse driven piezoelectric actuator.

To observe the suspension injection without producing the plasma but by the synchronized camera and laser with the injector the signal similar to the arc voltage has to be generated. The TTL signal, sent to the Ceradrop console, has been formed by Agilent 33250A

Waveform Generator (Palo Alto, CA, USA). The ramp signal has been generated with the frequency regulated to 1.4 kHz, what has been intended to simulate the arc voltage signal. From produced in this way signal the TTL pulse has been formed by the synchronization box and sent to Ceradrop platform.

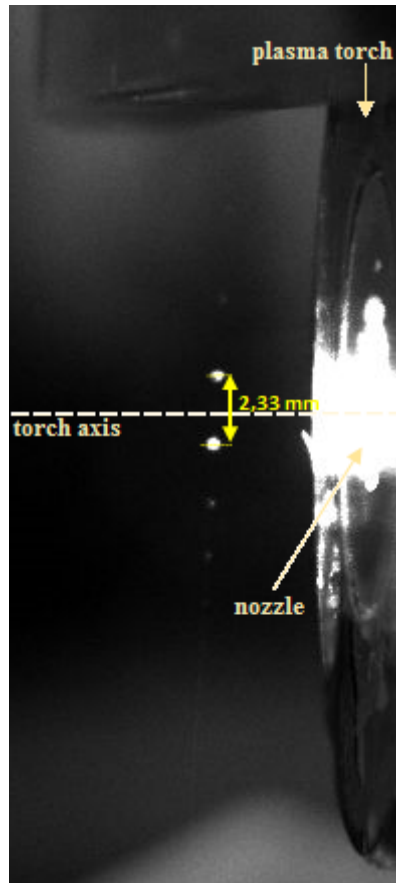


Figure 3.20: Measurement of droplet velocity. The brightness at the nozzle exit is due to the laser reflection. The picture taken by Infinimax objective.

It has allowed to activate the piezoelectric injector, the camera and the laser. The time-resolved imaging system has been used to observe the suspension injection and to make the measurements of the droplet velocity. The suspension injection frequency, f_i , according to Equation 3.2, is equal to 1.4 kHz. Figure 3.20 presents two suspension droplets illuminated by the laser and recorded by the camera. The measured distance, d_d , between them equals 2.33 mm, what gives the droplet velocity, v_d , of $3.26 \text{ m}\cdot\text{s}^{-1}$, obtained as follows: $v_d = d_d \cdot f_i$.

II.4 Observation of the suspension droplets inside the plasma

The following section presents the suspension injection inside the pulsed plasma jet. Figure 3.21 demonstrates the use of the suspension injection synchronized with the arc voltage signal. It shows four successive pictures taken by a standard, not synchronized, camera (aperture time $1/6000$ s, 24 frames per second). The photos present the individual plasma pulses containing TiO_2 particles resulting from heat treatment of injected droplets. In the first picture the moment of the synchronized suspension injection into the plasma ball is given. Then, in the successive pictures the plasma/droplet interaction is presented, what is characterized by a strong radiation. As can be observed in each photo, the material can be transported by the plasma jet over a long distance, i.e. more than 80 mm.

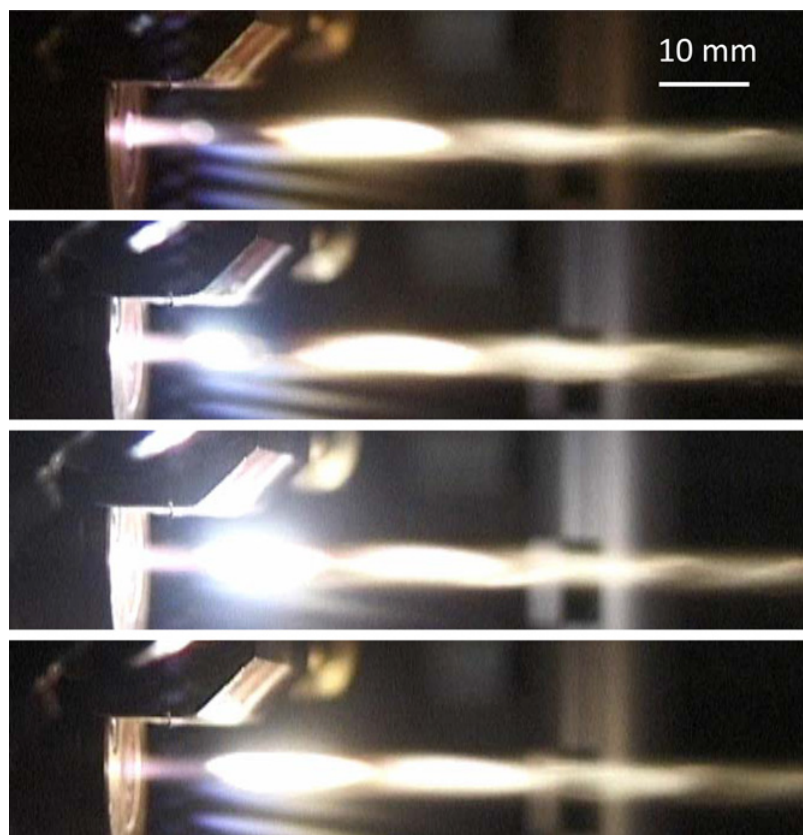


Figure 3.21: Imaging of synchronous suspension injection in the pulsed plasma jet taken by a standard camera: aperture time $1/6000$ s, 24 frames per second.

To better analyze the synchronized injection systems and the time-resolved imaging, the timing diagram for droplet emission and imaging is presented in Figure 3.22.

As has been mentioned, the emission of suspension droplet is triggered from sampling of the torch voltage after an adjustable delay, τ_{droplet} , counted after a falling front, as follows:

$$\tau_{\text{droplet}} = nT + \tau_j \quad (3.7)$$

where:

T is the arc voltage period, presented in Figure 3.22,
 τ_j the time at which a droplet penetrates the plasma.

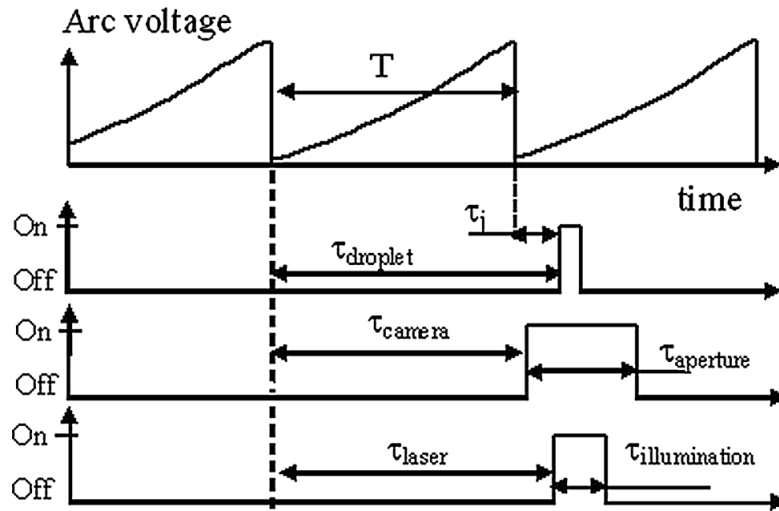


Figure 3.22: Timing for droplet emission and synchronous imaging [79].

The suspension injected to the plasma jet is observed by time-resolved and synchronous imaging system. The delay time of the camera, τ_{camera} in Figure 3.22, and of the laser, τ_{laser} , are adjusted with the emission of suspension droplet. As the obtained results have highlighted, τ_{camera} and τ_{laser} are respectively of $14 \mu\text{s}$ and 36 ns . τ_{aperture} is an adjustable time in the range of $5 \mu\text{s}$ and 65 ms , at which camera aperture is opened. $\tau_{\text{illumination}}$ is the laser pulse duration, which can be chosen up to $1 \mu\text{s}$. In the following experiments $\tau_{\text{illumination}}$ equals to exact $1 \mu\text{s}$.

In Figure 3.23 the time-resolved imaging of the dynamic interactions between the plasma jet and the droplets is presented. The pictures 3.23 a-d are obtained with a low-magnification objective (with the resolution presented in Figure 3.4 c)) for the different time delays over one period with $10 \mu\text{s}$ camera aperture time and $1 \mu\text{s}$ laser pulse duration. It has to be noted that the camera aperture of $10 \mu\text{s}$ is low enough to ensure that the plasma is immobile during the observation. To obtain the reliable results hundreds of pictures related to 3.23 a-d, triggered with the same τ_j , have been recorded. The laser shot has been used to visualize the solid particles left in the jet after solvent vaporization. However, their individual images are strongly oversized by diffraction, scattering, or resolution due to pixel size [79].

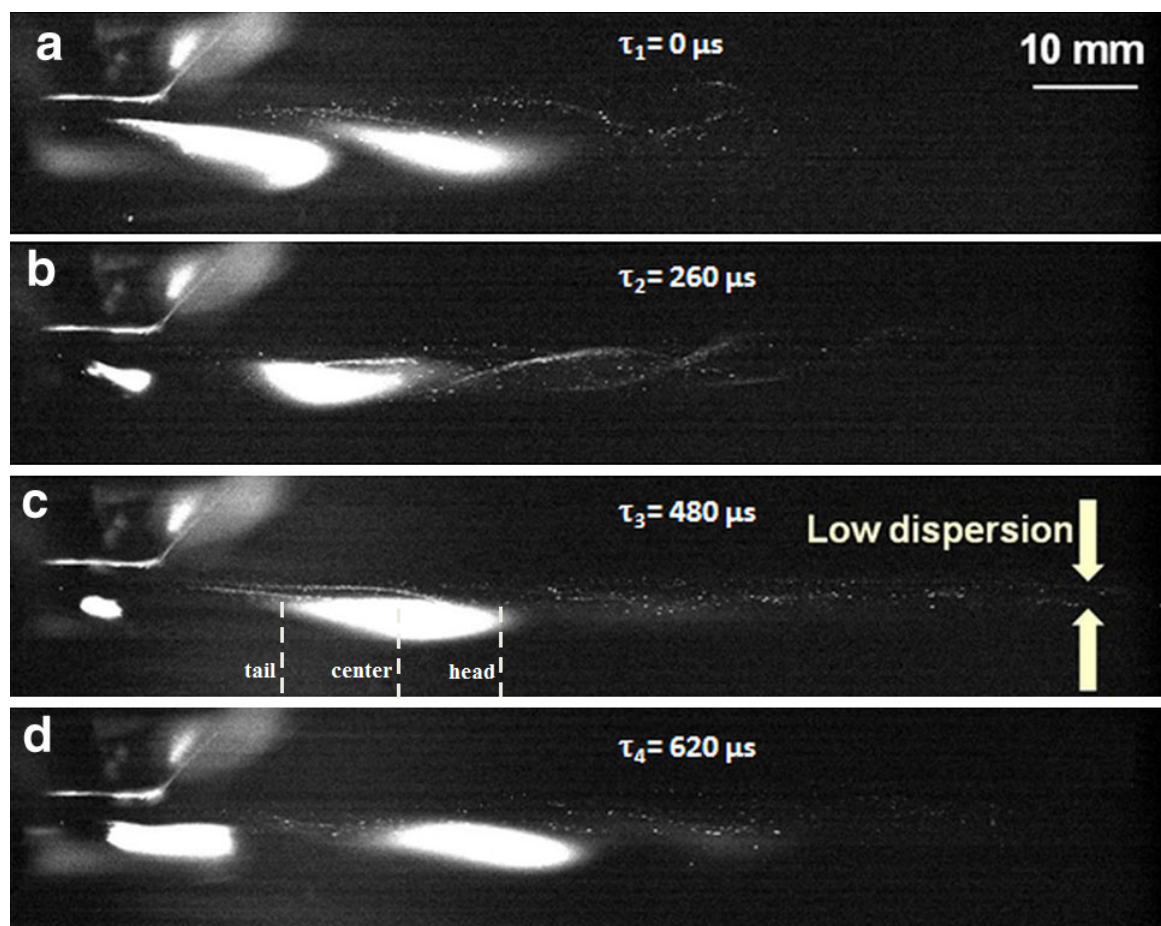


Figure 3.23: Time-resolved imaging of synchronized suspension injection with laser illumination for different injection time delay τ_j .

The image analysis has permitted to estimate the velocities of the center of mass of plasma balls with the vapors coming from the droplet vaporization. The velocities vary between around 30 m.s^{-1} for the case presented in 3.23 a) and 50 m.s^{-1} for 3.23 c). Moreover, it can be observed that each plasma ball is stretched while moving. Therefore, not only velocities of the center of mass of plasma balls should be defined. The velocities concerning the distance between the tails and between the heads of two succeeding balls should be also determined. This gives for Figure 3.23 c), respectively, 35 m.s^{-1} for the end of the balls, calculated above 50 m.s^{-1} for the center and 70 m.s^{-1} for the head. This means also that velocity of this pulsed plasma jet is time- and space-modulated. The obtained results correspond to the order of magnitude of mean plasma velocity evaluated from the following formula [55]:

$$\bar{v} = h_0 \frac{\dot{m}(\gamma - 1)}{P_a \cdot S \cdot \gamma} \quad (3.8)$$

where:

γ is the nitrogen plasma isentropic coefficient,
 P_a the pressure at the nozzle exit (atmospheric pressure).

Assuming that $\gamma \simeq 1.3$ and $h_0 \simeq 13.3 \text{MJkg}^{-1}$ the calculated mean plasma velocity is estimated to around 100m.s^{-1} . Moreover, this expression indicates also that velocity must be modulated because the specific enthalpy changes with time due to the voltage variations.

Table 3.3: Summary of experimental conditions.

Plasma	Time-resolved imaging system	Synchronized injection
N_2 : 2 slm	$\tau_{\text{illumination}} = 1 \mu\text{s}$	$\tau_1 = 0 \mu\text{s}$
$I = 15 \text{A}$	$\tau_{\text{aperture}} = 10 \mu\text{s}$	$\tau_2 = 260 \mu\text{s}$
$d_{\text{nozzle}} = 4 \text{mm}$	interferential filter = 801 nm	$\tau_3 = 480 \mu\text{s}$
	Frequency of image	$\tau_3 = 620 \mu\text{s}$
$f = 1410 \text{Hz}$	acquisition = 75 Hz	$f_i = 1410 \text{Hz}$

Table 3.3 summarizes the conditions of the experiment shown in Figure 3.23 a-d. It demonstrates that the trajectories and related thermal history of injected materials depend on the moment when droplets penetrate into the plasma. In case of $\tau_1 = 0 \mu\text{s}$, the most significant part of materials travels in the plasma fringes giving rise to large dispersion of trajectories ($\sim 10 \text{mm}$) and limited axial distance of material transport ($\sim 40\text{-}60 \text{mm}$). In case of $\tau_2 = 260 \mu\text{s}$, the treatment materials in the plasma core is improved with a lower radial dispersion and a slightly increased transport distance. The pulsed plasma jet is trapping particles all along its own axis, what can be observed as alternate and intricate trajectories. This effect seems to be due to the pulsed emission of the plasma balls that alternate their curvatures by interacting between each others. This gives a certain spatial coherence for the plasma jet and also recalls some visual effects such as the Von Karman Street in vortices emission. In Figure 3.23 c) ($\tau_3 = 480 \mu\text{s}$), a low material dispersion is observed corresponding to the longest transport distance. At last, the case of $\tau_4 = 620 \mu\text{s}$, because it is almost the $700 \mu\text{s}$ period, resembles the first case $\tau_1 = 0 \mu\text{s}$.

Moreover, the influence of the moment at which a droplet penetrates the pulsed arc jet has been investigated using the camera with mounted Infinimax objective (Figure 3.4 b)). The results are presented in Figure 3.24.

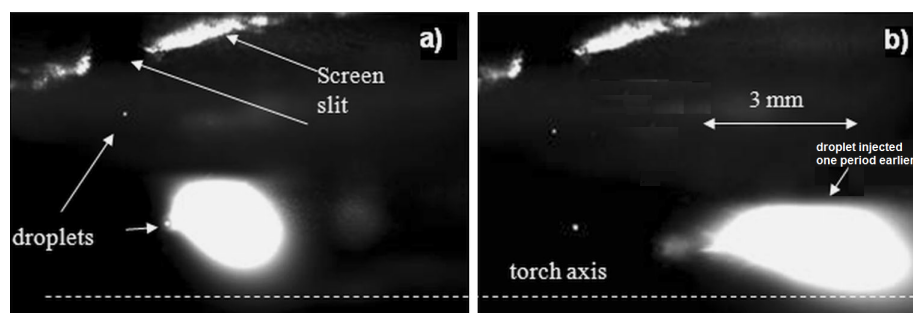


Figure 3.24: Influence of the local instantaneous specific enthalpy on droplet thermal treatment: (a) high level of enthalpy, (b) low level. Camera exposure time: $5 \mu\text{s}$, laser illumination: $1 \mu\text{s}$ [74, 79].

The camera and the laser are delayed by the same time after the droplet emission but the suspension penetrates the plasma earlier in Figure 3.24 a) than in b), what has been obtained by changing τ_j . The droplet, which is possible to observe due to the illumination by the laser, enters the plasma 4 mm downstream of the nozzle exit. The picture a) and b) are observed through a narrow band-pass filter centered on the laser wavelength. As has been mentioned in the previous sections, this configuration permits to eliminate on the image the light coming from the pure nitrogen plasma. Therefore, Figure 3.24 shows merely the seeded plasma balls characterized by a strong increase of the brightness, which resulted from the interaction of the nitrogen plasma with the material contained in the suspension droplet. In Figure 3.24 a) the lower droplet penetrates the plasma at a moment corresponding to a situation presented in Figure 3.10 d). This moment has been chosen due to high level of local specific enthalpy. Therefore, Figure 3.24 b) corresponds to the plasma characterized by a low enthalpy level, shown in Figure 3.10 a). In case presented in Figure 3.24 a) the almost immediate vaporization process of the droplet has been observed, what differs from the situation shown in b). In this case, the vaporization-seeding process does not concern the injected droplet but the one introduced one period earlier, what gives the plasma ball at the right of Figure b).

Figure 3.25 a-d displays four successive pictures taken by the high-speed camera (6000 frame/s) with an exposure time of $100 \mu\text{s}$. The time between each picture is about $166 \mu\text{s}$. The observation area is shifted by approximately 1 cm downstream of the torch exit, compared to results presented in Figure 3.23. τ_{droplet} is adjusted so that each droplet reaches the plasma axis $\tau_j = 260 \mu\text{s}$ after a voltage falling front. On the left of Figure 3.25 a), the tip of the arc jet is presented that contains no droplet. The spherical shape, which follows immediately on the right, is the result of a droplet injected in the preceding period. The right part of the picture shows the result of the plasma interaction with a droplet injected two periods before. Figure 3.25 b) follows a) by $166 \mu\text{s}$.

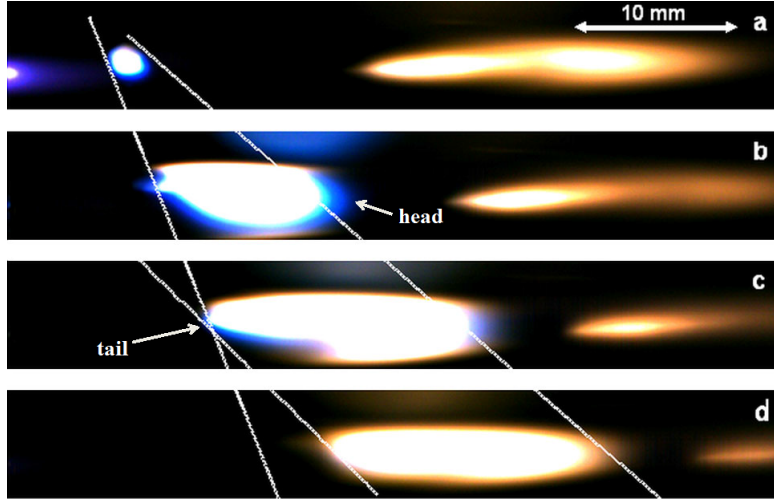


Figure 3.25: Fast imaging (6000 frame/s, time aperture: 100 μs) of synchronized suspension injection in nitrogen pulsed arc plasma jet for the injection time delay $\tau_j = 260 \mu\text{s}$. The white lines indicate that for each plasma ball the tail and the head of a single plasma ball do not travel at the same speed, as previously mentioned.

The spherical shape has been strongly expanded and lengthened due to vaporization process. However, the sharp details at the left of the plasma ball suggest that a certain amount of liquid still remains non-vaporized. The expansion is continued in Figure 3.25 c) and seems to reach a maximum in Figure 3.25 d). The dotted lines drawn on these pictures show that the front part of the plasma ball travels at a speed approximately twice that of the rear part, which is consistent with the expansion process. The rear part lags behind the plasma ball because it still contains a small amount of suspension under acceleration. Once the vaporization is complete, the plasma ball travels as a whole as it can be seen in Figure 3.25 c) and d). A picture taken 166 μs after the situation of Figure 3.25 d) should be similar to a).

The evolution of successive volumes over a sequence of four pictures is measured by the image analysis. Assuming that the resulting plasma balls have an ellipsoidal shape, the volume of the ball is given as follows: $V = \frac{4}{3}\pi\Delta x.\Delta y.\Delta z$, where z is the axial coordinate and the radial expansion is established to be isotropic: $\Delta x \sim \Delta y$. Figure 3.26 presents the measurements of the expansion rates of droplets during plasma treatment for the different injection time delays, τ_j , given in Figure 3.25.

The expansion rate is defined as: $(V_i - V_{i-1})/\Delta t$, with V_i determined as the volume at the instant $t_i = i \times \Delta t$, where $\Delta t = 166 \mu\text{s}$, $i \in [0; 3]$. t_0 corresponds to the moment presented in Figure 3.25 a). The standard deviation results from the measurements of the volumes for 10 similar sequences of pictures. The expansion rate, Figure 3.26, significantly depends on τ_j , particularly during the first 166 μs .

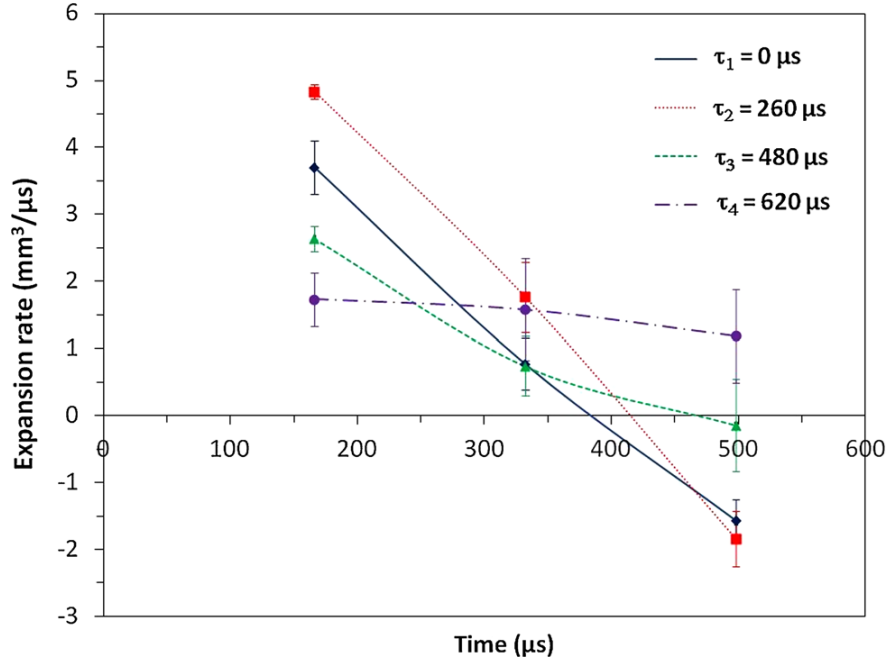


Figure 3.26: Dependence of measured expansion rates of plasma balls on the injection time delay τ_j .

Later, the expansion rate decreases and becomes negative for $\tau_1 = 0 \mu s$ and $\tau_2 = 260 \mu s$, what is related to the recombination process of plasma. As has been presented, the enthalpy of the plasma is strongly modulated in the proportion: $h_{\max}/h_{\min} \simeq 18$ with a mean value of 13.3 MJkg^{-1} . Therefore, the heat transfers to droplets and, consequently, the expansion rates are affected by this modulation.

Table 3.4 gives the calculated parameters describing the system of the suspension phased injection in pulsed arc jet.

Table 3.4: Parameters of suspension phased injection system.

Nitrogen mass flow rate	(kg.s^{-1})	4.2×10^{-5}
Nitrogen/one period	(kg)	3×10^{-8}
Energy/one plasma ball	(J)	0.5
Injection velocity	(m.s^{-1})	3.26
Injection frequency	(Hz)	1.4×10^3
Droplet diameter	(m)	50×10^{-6}
Suspension density	(g.cm^{-3})	1.204
Droplet mass	(kg)	8×10^{-11}
Suspension flow rate	(ml.min^{-1})	5.6×10^{-3}
Powder mass flow rate	(g.min^{-1})	3.4×10^{-4}

The nitrogen mass flow rate, measured by a Brooks Instrument mass flow controller, is around $4.2 \times 10^{-5} \text{ kg.s}^{-1}$. Therefore, the amount of nitrogen which flows during one period, $T = 700 \text{ } \mu\text{s}$, is approximately equal to $3 \times 10^{-8} \text{ kg}$ and the energy content in one plasma ball is 0.5 J , which is obtained by the division of the power net by the plasma frequency 1.4 kHz . The mass of a suspension droplet, entering to the plasma jet, is given by the formula: $m = \rho \cdot \frac{4}{3} \pi \left(\frac{d_d}{2}\right)^3$ and equals approximately $8 \times 10^{-11} \text{ kg}$. The energy needed for water vaporization is determined as follows: $E_{\text{vap}} = m_{\text{droplet}} \cdot L_v$, where the mass of the droplet, m_{droplet} , has been defined above and the water latent heat, L_v , has been given in chapter 1 in table 1.2 and is equal to around $2.26 \times 10^6 \text{ J.kg}^{-1}$. Therefore, the energy needed for water vaporization $E_{\text{vap}} \simeq 1.8 \times 10^{-4} \text{ J}$, what is much smaller than the energy content in one plasma ball 0.5 J . Consequently, it can be stated that the available energy of pulsed plasma jet is high enough to vaporize completely the solvent and liberate solid particles, what will be presented in the following sections.

II.5 Thermo-physical phenomena of suspension droplets

As has been presented in Chapter 1 the suspension droplets, injected to the plasma jet, undergo the fragmentation and vaporization processes. The fragmentation depends on the dimensionless Weber number which is determined by the following equation:

$$We = \frac{v_r^2 \cdot d_l \cdot \rho_p}{\sigma_l} \quad (3.9)$$

where:

- ρ_p is the plasma density,
- v_r the relative velocity between the plasma and the droplet,
- d_l the diameter of the liquid droplet,
- σ_l the surface tension of the liquid.

The determination of the modulation of the plasma enthalpy has presented that $h_{\text{min}} = 1.4 \text{ MJ/kg}$ and $h_{\text{max}} = 26 \text{ MJ/kg}$. By using the data found in [17] it is possible to determine the nitrogen plasma density, related to h_{min} and h_{max} , what is presented in Table 3.5.

Table 3.5: Properties of the nitrogen plasma [17].

Temperature	Density	Enthalpy
K	kg/m^3	MJ/kg
1500	2.27×10^{-1}	1.4
7100	3.24×10^{-2}	26

Introducing to Equation (3.9) the plasma density presented in Table 3.5 and suspension properties given in Table 3.2, calculated Weber number ranges between 0.04 and 0.48.



Figure 3.27: Treatment of the suspension droplet in the plasma jet characterized by high local instantaneous specific enthalpy.

As has been presented in Chapter 1, the critical value of We , over which the droplet undergoes the breakup process, equals 14. The obtained results have shown that in the present system the fragmentation process of the suspension droplet does not occur. Figure 3.27 confirms this postulate, where two suspension droplets, marked by yellow circles, seems not to undergo the breakup process.

Under these conditions, the process of solvent reduction from the suspension droplet is governed by the heat transfer and vaporization, which can be represented by the scheme shown in Figure 3.28.

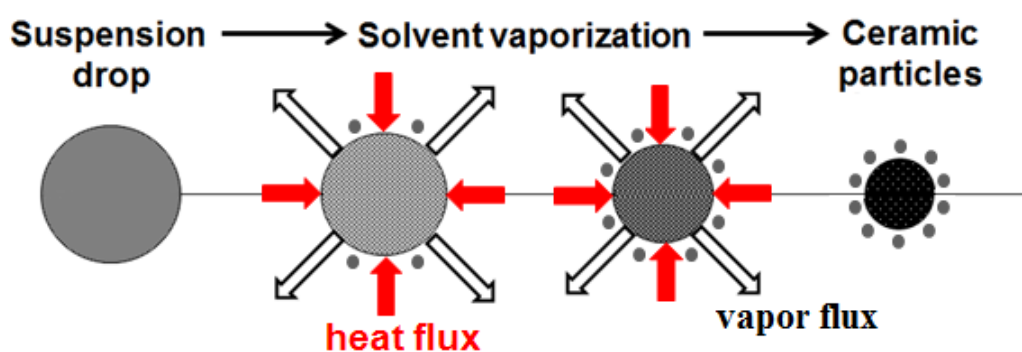


Figure 3.28: Schematic of suspension treatment by modulated plasma jet.

To estimate the vaporization time of the suspension in the plasma jet, certain assumptions have to be made. The diameter of the solid particle is determined as follows:

$$d_s = d_l \left[1 + \frac{1 - x_m}{x_m} \frac{\rho_s}{\rho_{solvent}} \right]^{-1/3} \quad (3.10)$$

where:

d_l is the diameter of the suspension droplet,
 x_m the mass fraction of the ceramic,
 ρ_s the solid density,
 $\rho_{solvent}$ the solvent density.

The thermal power transferred to a sphere of radius, r , is evaluated from the heat transfer coefficient by convection, h_c , as follows:

$$\Phi_{th} = h_c(T - T_l).4\pi r^2 \quad (3.11)$$

where:

T is the plasma temperature,
 T_l the temperature at the surface of the liquid,
 h_c the heat transfer coefficient given by : $h_c = \frac{Nu.\kappa}{d_l}$.

Introducing the enthalpy, h , and the heat capacity, c_p , to Equation 3.11, the thermal power is presented as follows:

$$\Phi_{th} = \frac{(Nu.\kappa)(h - h_l).4\pi r^2}{c_p.d_l} \quad (3.12)$$

where:

h is the plasma specific enthalpy, which can be determined by torch energy balance measurements or more locally from the temperature measurement by the emission spectroscopy,
 h_l the plasma enthalpy at the temperature of the droplet, which is much lower than h .

κ/c_p is, in fact, the ratio of the conduction potential, $\varphi(T) = \int_{T_{ref}}^T \kappa(T)dT$ (defined in chapter 1), to specific enthalpy, $h = \int_{T_{ref}}^T c_p(T)dT$. Using the thermodynamic and transport properties of N_2 , it can be shown, from a numerical point of view, that it gives: $\varphi(T) \simeq a_\varphi h(T)$, where a_φ is the coefficient determined in the model in chapter 1. For the nitrogen and the enthalpy range of the plasma produced in "Mosquito" mode, $a_\varphi = 2.8 \cdot 10^{-4} \text{ kg.m}^{-1}.\text{s}^{-1}$.

Knowing that $d_l = 2r$, the heat flux is given by:

$$\Phi_{th} = (Nu.a_\phi)h.2\pi r \quad (3.13)$$

During the vaporization phase of the solvent, the droplet diameter decreases from d_l to d_s . Considering the latent heat of vaporization of the solvent, L_v , and the liquid density, $\rho_{solvent}$, the decrease of the radius, r , due to the vaporization requires the energy as follows:

$$dE = 4\pi r^2 dr.\rho_{solvent}.L_v \quad (3.14)$$

what is given for the period of time dt by the heat flux Φ_{th} so that:

$$4\pi r^2 dr.\rho_{solvent}.L_v = -(Nu.a_\phi)h.2\pi r dt \quad (3.15)$$

Introducing the vaporization time, for which the solvent has disappeared completely ($r=d_s/2$) and knowing that this process starts at $t=0$ with $r=d_l/2$, it gives the following formula:

$$d_l^2 - d_s^2 = \frac{4Nu.a_\phi.h}{\rho_{solvent}.L_v} t_{vap} \quad (3.16)$$

Taking into account the mass fraction of the ceramic, x_m , the vaporization time is given as follows:

$$t_{vap} = \frac{\rho_{solvent}.L_v}{4Nu.a_\phi} \left[1 - \left(1 + \frac{1-x_m}{x_m} \frac{\rho_s}{\rho_{solvent}} \right)^{-2/3} \right] \frac{d_l^2}{h_p} \quad (3.17)$$

The factor $\left[1 - \left(1 + \frac{1-x_m}{x_m} \frac{\rho_s}{\rho_{solvent}} \right)^{-2/3} \right]$ is in the range between 0.73, for the mass fraction, x_m , of 0.4 and $\rho_s/\rho_{solvent}$ of 4, and 0.85 for the mass fraction of 0.2.

Moreover, Equation (3.17) highlights that the vaporization time depends on the square of the diameter of the initial suspension droplet and the plasma specific enthalpy, h . For the specific enthalpy of 1.4 MJ/kg and the diameter, d_g , of 50 μm the vaporization time equals 1.4 ms (for $x_m = 0.4$) or 1.65 ms (for $x_m = 0.2$). For the specific enthalpy of 26 MJ/kg, t_{vap} equals, respectively, 77 μs and 90 μs .

The calculation of t_{vap} highlights that the choice of the injection time delay can have an effect on solvent vaporization, what is verified by Figure 3.24. The obtained results by pulsed laminar plasma jet show the possibility of control of material injection into different zones of modulated plasma. This can allow controlling some of the thermo-physical processes occurring at the droplet scale, such as the evaporation.

III Time-resolved spectroscopy

The following section presents the last part of the experimental setup given in Figure 3.1, described in the introduction to this chapter. The measurements performed by the time-resolved optical emission spectroscopy, presented in Figure 3.29, will be highlighted.

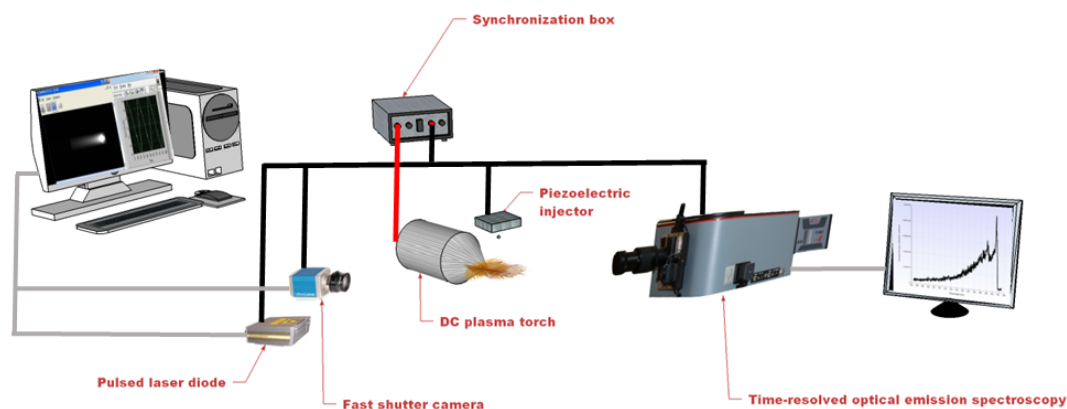


Figure 3.29: Schematic view of the experimental setup with added time-resolved optical emission spectroscopy.

The previous paragraphs have shown that the pulsed plasma jet is characterized by the specific enthalpy strongly modulated, what has been demonstrated by the results obtained from the energy balance measurements. To determine in more precise and local way this modulation the plasma temperature measurements have to be performed. However, in the case of plasma, the direct diagnosis of the temperature, e.g. by the thermometer, are often impossible. Among all available techniques the optical emission spectroscopy has been chosen, what will be presented in the following sections.

Moreover, the diagnosis of modulated plasma, produced by a "Mosquitorch", requires the method which allows to study the plasma in synchronized dynamic way. Therefore, the plasma temperature measurements have been carried out by time-resolved optical emission spectroscopy (TROES).

The following section will give the approach to the optical emission spectroscopy as the measurement technique of the gas temperature. Therefore, firstly, the preparation of the experimental setup to the measurements will be presented. The calibration of the system of the wavelength and intensity axis will be highlighted. Then, to determine the gas temperature the $N_2(C^3\Pi_u - B^3\Pi_g)$ system (the second positive system of nitrogen) or $N_2^+(B^2\Sigma_u^+ - X^2\Sigma_g^+)$ system (the first negative system of nitrogen) have to be defined. Consequently, the investigation of the species in the pulsed plasma produced by the "Mosquitorch" have been performed. All given above procedures have led to the gas temperature measurements. The use of the spectrograph working at medium spatial resolution permits to obtain reliable measurements of the rotational temperatures because

they are performed with a wide spatial range of the excited states, what will be presented in the following paragraphs.

III.1 Fundamentals of TROES

The following section will be focused on a merely part of the broad subject of the optical emission spectroscopy. The essential information about the fundamentals of the spectroscopic measurements, which has been studied for the gas temperature measurements, will be highlighted.

In the emission spectroscopy the light emitted from the plasma is recorded and analyzed. The total energy emitted through the surface of the plasma as the electromagnetic radiation is defined as a radiant flux, Φ (W), presented in Figure 3.30.

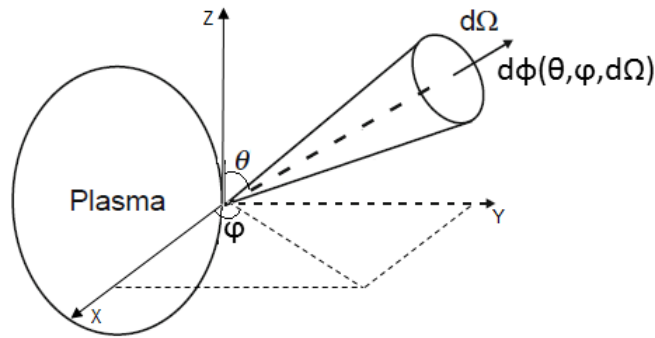


Figure 3.30: Definition of the radiance [84].

The radiant intensity, I ($\text{W}\cdot\text{sr}^{-1}$), is the flux per solid angle emitted from the plasma:

$$I(\theta, \phi) = \frac{d\Phi(\theta, \phi, d\Omega)}{d\Omega} \quad (3.18)$$

where:

Ω is the solid angle, defined in Figure 3.30.

The radiance, L , at the position \vec{r} , is the intensity radiated per unit area dA ($\text{W}\cdot\text{m}^{-2}\cdot\text{sr}^{-1}$). Therefore, it is the energy flow radiated by an unit area per unit solid angle determined as follows:

$$L(\theta, \phi) = \frac{I(\theta, \phi)}{dA \cdot \cos\theta_A} = \frac{d^2\Phi(\theta, \phi, d\Omega_A)}{d\Omega_A dA \cos\theta_A} \quad (3.19)$$

where:

dA is the surface element.

In the spectral measurements the radiance is defined as emitted at the wavelength, $d\lambda$, therefore the spectral radiance is determined as follows:

$$L_{\lambda}(\theta, \phi) = \frac{dL(\theta, \phi)}{d\lambda} \quad (3.20)$$

Moreover, the local emission, $\varepsilon(\theta, \phi)$, has to be defined. It is the intensity emitted by the plasma in a given direction and unit volume ($\text{W.m}^{-3}.\text{sr}^{-1}$), determined as follows:

$$\varepsilon(\theta, \phi) = \frac{I(\theta, \phi)}{dV} = \frac{d^2\Phi(\theta, \phi, d\Omega)}{d\Omega dV} \quad (3.21)$$

In the spectral measurements the emission coefficient, ε , of the line should be defined. The spectral line is emitted when a bound electron undergoes a transition from an upper level (p) of energy $E(p)$ to a lower level (q). With each transition a photon is emitted, and ε of the line thus is given by:

$$\varepsilon_{p \rightarrow q} = \frac{hc}{4\pi\lambda_0} n(p) A_{p \rightarrow q} \quad (3.22)$$

where:

- $A_{p \rightarrow q}$ is the characteristic atomic constant for that specific transition and known as atomic transition probability (unit s^{-1}) or Einstein coefficient of spontaneous emission,
- $n(p)$ the population density of the excited level p.

The quantity that is recorded by the spectrometer is the result of the light emitted all along the line of sight (assuming that the absorption is neglected). The absolute line intensity (unit $(\text{m}^3\text{s})^{-1}$) is defined as follows:

$$I^{(y)}_{p \rightarrow q} = \int_{\text{line of sight}} \varepsilon_{p \rightarrow q}(x, y) dx \quad (3.23)$$

where y is the height of the line of sight above the plasma axis. $I_{p \rightarrow q}$ is the intensity of the spectral line, which has the same unit that L. If the dependence of the intensity with the wavelength is needed, it is possible to introduce the spectral profile, $I(\lambda)$, so that:

$$I_{p \rightarrow q}(\lambda, y) = I_{p \rightarrow q}(y) \cdot \Phi(\lambda) \quad (3.24)$$

where: $\int_{\Delta\lambda} \Phi(\lambda) d\lambda = 1$

The molecular spectra are characterized by the complex structure: the states due to electronic excitation as well as the ground state, conventionally known as the X state, are split into vibrational levels, and these again into rotational ones. Figure 3.31 highlights the partial energy level diagram for N_2 , N_2^+ and N_2^- states versus their internuclear distance (R).

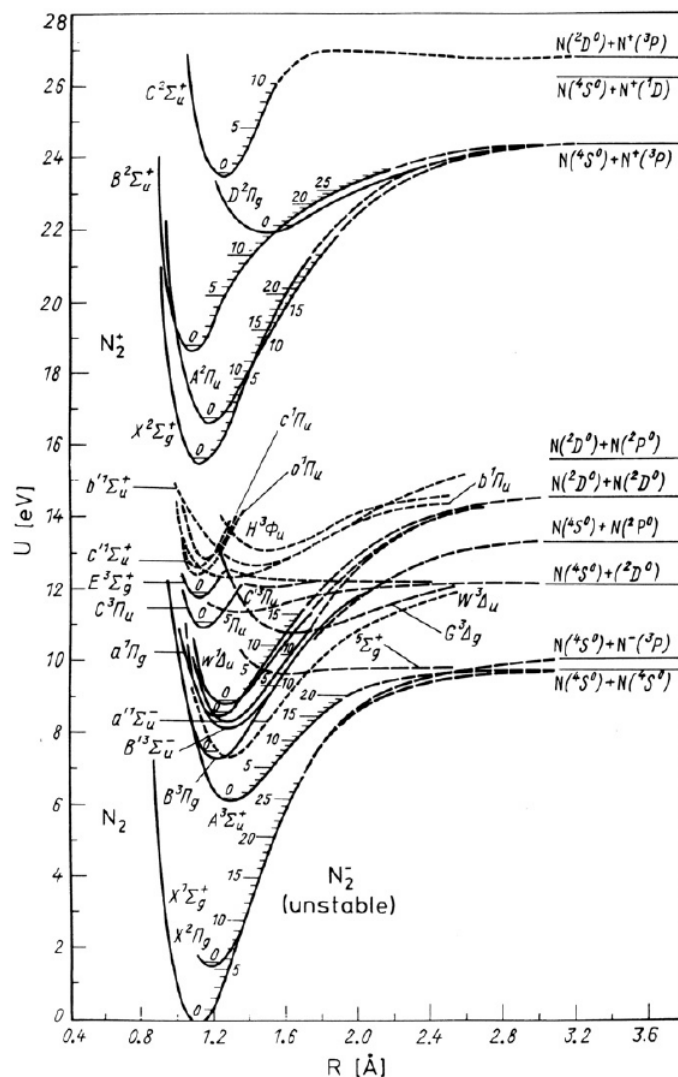


Figure 3.31: Diagram of potential energy curves of N_2 molecular state [85].

As can be seen in Figure 3.31 the electronic energy levels are defined by e.g. $X^2\Sigma_g^+$, $B^3\Pi_g$, $B^2\Sigma_u^+$. The electronic energy levels of atoms, 3.25, and diatomic molecules, 3.26, have their spectroscopic notation, as follows:

$$n\ell^{w2S+1}L_{L+S} \quad (3.25)$$

$$n\ell^{w2S+1}A_{A+\Sigma_{g,u}^{+,-}} \quad (3.26)$$

where:

n	is the main quantum number,
ℓ	the angular momentum,
w	the number of electrons in the shell,
S	the spin,
2S+1	the multiplicity,
L+S = J	the total angular momentum,
+, - and g, u	the symmetry of the electronic wave function.

The optically allowed transitions follow the selection rules for dipole transitions which can be summarized as: $\Delta L = 0, \pm 1, \Delta J = 0, \pm 1, \Delta S = 0$ for atoms and $\Delta L = 0, u \leftrightarrow g$ for molecules.

As has been mentioned above, the molecular electronic levels are divided into vibrational and rotational ones, with the transitions occurring between pairs of these levels. Each level is specified by its electronic state (e), vibrational (v) and rotational quantum number (J). The internal energy of a molecule in this so-called rovibronic level (e,v,J) is given by [86]:

$$T_{evJ} = T_e + G_v + F_J \quad (3.27)$$

Therefore, considering the transition from upper rovibronic level (e', v', J') to lower level (e'', v'', J'') the spectral emission coefficient can be determined, following the equation (3.22), by:

$$\varepsilon(\nu) = n_{e'v'J'} \frac{A_{e'v'J'-e''v''J''}}{4\pi} (T_{e'v'J'} - T_{e''v''J''}) \Phi(\nu - \nu_0) \quad (3.28)$$

where:

$n_{e'v'J'}$	is the population of the upper level,
$A_{e'v'J'-e''v''J''}$	the Einstein coefficient for spontaneous emission, defined above,
$T_{e'v'J'} - T_{e''v''J''}$	the energies of the upper and lower levels respectively, defined as follows: $T_{e'v'J'} - T_{e''v''J''} = h\nu_0 \simeq h\nu$,
$\Phi(\nu - \nu_0)$	the lineshape function.

The population $n_{e'v'J'}$ of the upper state in the further experiments will be assumed as Boltzmann distributed. Therefore, the following relation presents the calculation of $n_{e'v'J'}$ described by a Boltzmann distribution, as follows:

$$n_{e'v'J'} = n_{total} \frac{g_{e'} (2J' + 1) \exp\left[-\frac{T_{e'}}{kT_{el}} - \frac{G(v')}{kT_{vib}} - \frac{F(J')}{kT_{rot}}\right]}{\sigma \sum_{e,v,J} g_e (2J + 1) \exp\left[-\frac{T_e}{kT_{el}} - \frac{G(v)}{kT_{vib}} - \frac{F(J)}{kT_{rot}}\right]} L(J', P'_{ef}, P'_{gu}) \quad (3.29)$$

It assumes that the internal levels follow Boltzmann distribution at T_{el} , T_{vib} and T_{rot} . n_{total} defines the total population of the molecule, $L(J', P'_{ef}, P'_{gu})$ the line alternation factor due to nuclear spin defined in e.g. [87]. σ is a factor equals 2 for homonuclear molecules and 1 for heteronuclear molecules, $g_{e'}$ is the degeneracy of the electronic level defined as follows: $g_{e'} = (2 - \delta_{0,\Lambda'}) (2S + 1)$.

III.2 Experimental setup

The spectroscopic measurements have been carried out by the IsoPlane spectrograph (Princeton Instruments, Trenton, New Jersey), presented in Figure 3.32.

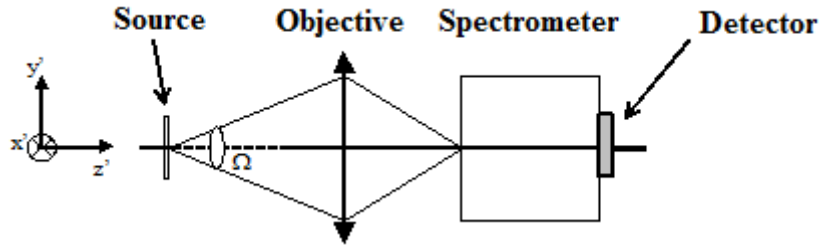


Figure 3.32: Schematic view of the emission spectroscopy system.

The objective consists of the quartz lens, characterized by the transmission $> 80\%$ from 200 to 1100 nm. The detector, Figure 3.32, is PI-MAX4 ICCD camera (Princeton Instruments) mounted directly at the image plane of the spectrograph exit. The pixel size influences the spectral resolution of the system. Therefore, the camera characterized by the imaging array of 1024×1024 and the pixel size of $13 \times 13 \mu\text{m}$ has been chosen. Moreover, the connection to the computer allows controlling the measurements by LigthField software and recording the spectra. LightField permits to regulate the following acquisition settings which define the response of the ICCD detector:

- Exposure time, τ_{exp}

The length of time between the beginning and the end of the acquisition sent by LightField to the camera, defining the exposure time of the sensor.

- Number of accumulations, N_{acc}

The number of times on which the photocathode is gated during the exposure. The charge is accumulated on CCD array when these gates occur during the exposure and then is readout at the end of it.

- Gate width, τ_{width}

The time during which light is detected by an intensifier, strengthened, and applied to the sensor.

- Gain, G

The determination of the amount of electron multiplication that is applied to improve the signal.

IsoPlane spectrograph (SCT 320, 320 mm focal length) consists of: the entrance and exit slit, the grating as the dispersive element, the imaging mirrors. The choice of the spectrometer grating, which is determined by the grooves per millimeter (lines/mm) is of importance for the spectral resolution and to determine the wavelength range of the spectral measurement. The fundamental grating equation is defined as follows:

$$m\lambda = d(\sin\alpha + \sin\beta) \quad (3.30)$$

where:

m	is the diffraction order,
d	the groove spacing,
α	the angle at which the beam of parallel radiation incident on the grating,
β	the angle of the spectral line.

The IsoPlane spectrograph is equipped with 300, 1200 and 2400 g/mm gratings. Figure 3.33 presents the principle of the spectroscopic measurement by the system used in this work. The image of the plasma is formed with a negative magnification (the result of image inversion) on the spectrometer entrance slit, characterized by the width, w_e , which can be changed from 10 μ s up to 12 mm to give the possibility to perform imaging with PIMAX camera. Then, the spectrometer forms the monochromatic image, centered around λ_1 with the magnification of 1, in the detector plane. As has been mentioned above, the detector is composed of the imaging array of 1024×1024 with the pixel size of $13 \times 13 \mu$ m, what can be grouped into lines of height, Δy_p , by the Lightfield function called binning. The "enlightened" area on the detector, in Figure 3.33, presents the plasma surface of $w'_e \cdot \Delta y'$.

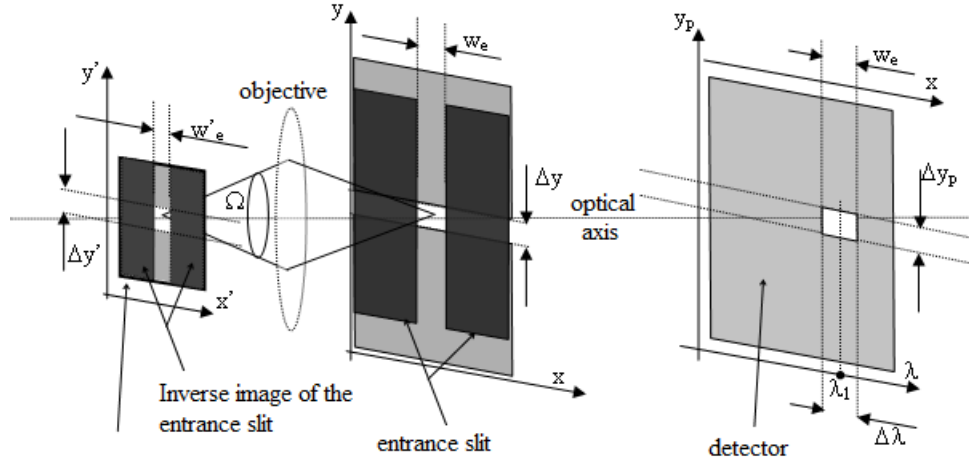


Figure 3.33: Schematic view of the image formation by the spectroscopy system.

III.2.1 Calibration

The important issue of the spectroscopic measurement is the calibration of the system. To obtain precise information about plasma parameters the calibration of the wavelength and intensity axis have been performed. In the case of wavelength axis the calibration has been done by recording spectra of a source with known wavelengths. The USB Light Source (Princeton Instruments, Trenton, New Jersey) has been used which consists of Hg and Ne-Ar lamps with well-defined atomic emission lines presented in Figure 3.34.

The mercury and neon-argon lamps have been used because of their wide wavelength range which covers the lines of nitrogen plasma and the plasma-suspension interaction. In case of the calibration of the intensity axis, a standard radiator of known radiance, L_0 , is placed close to the spectrometer entrance slit to fill the solid angle, Ω . Then, the flux, $\Phi_\lambda(\lambda)\Delta\lambda = L_{0\lambda}(\lambda)\Delta\lambda A_s \Omega$, over a spectral interval, $\Delta\lambda$, produces a signal S_0 at the exit of a detector. Keeping all settings constant, the respective flux in the same spectral interval from the plasma gives the signal, S_{plasma} . Therefore, the radiance of plasma is given by:

$$L_{plasma_\lambda}(\lambda) = \frac{S_{plasma}}{S_0} L_{0\lambda} \quad (3.31)$$

In the calibration process the tungsten strip lamp has been applied. It is the most commonly used secondary standard source, in which a strip of tungsten is mounted in a glass envelope with a window of fused silica, characterized by the transmission coefficient, α_T , around 0.9. The parameters of the tungsten lamp are commonly given by the constructor. However, these standard radiators age, therefore, to obtain precise spectrometer calibration it has been calibrated in the laboratory by the pyrometer.

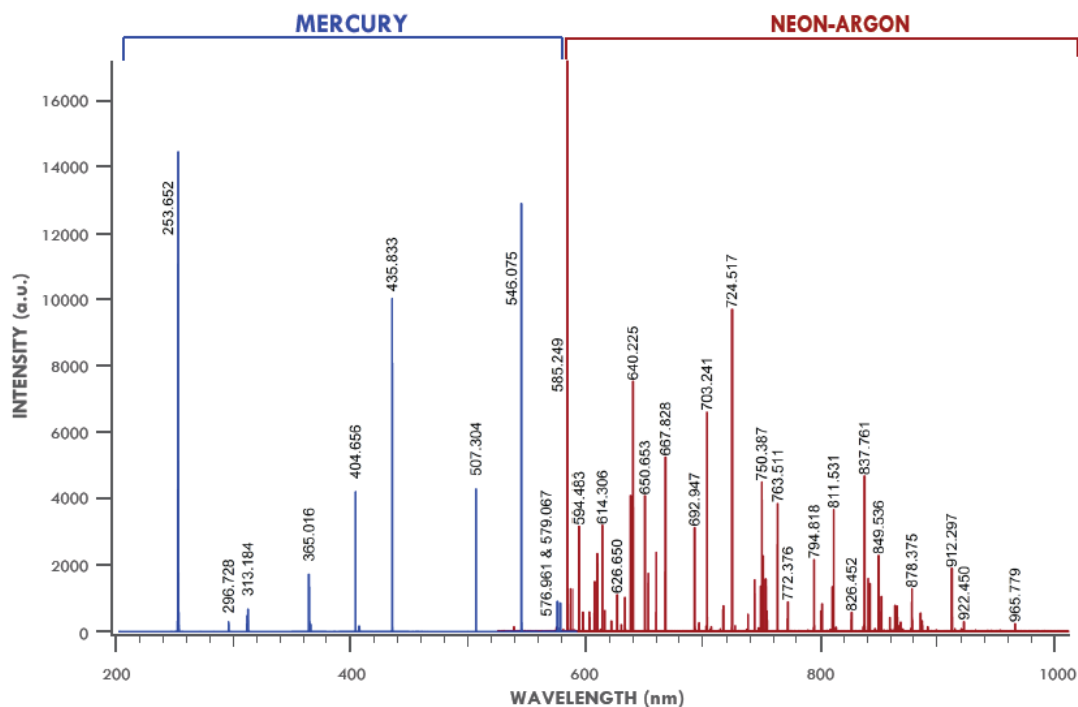


Figure 3.34: Wavelength calibration spectra of mercury and neon-argon lamps.

The lamp has been power supplied by a stabilized source. The current, presented in Figure 3.35, has been measured using a precision shunt.

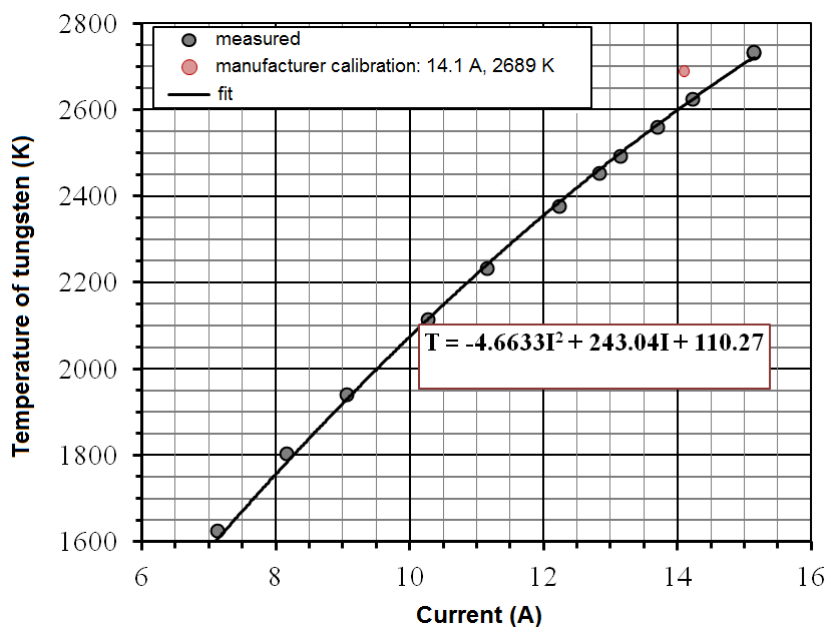


Figure 3.35: Calibration curve of tungsten strip lamp.

Afterwards, the spectral radiance of the tungsten strip lamp, $L_0(\lambda, T)$, has been obtained by multiplying the Planck function with the spectral emissivity of tungsten, $\varepsilon_0(\lambda, T)$, as follows:

$$L_0(\lambda, T) = \varepsilon_0(\lambda, T) \frac{2hc^2}{\lambda^5} \frac{1}{\exp\left(\frac{hc}{\lambda kT}\right) - 1} \quad (3.32)$$

$\varepsilon_0(\lambda, T)$ has been determined from the data given by De Vos [88]. The calibration procedure have been carried out for the parameters of the spectrometer and detector given in Table 3.6.

Table 3.6: Parameters of the spectroscopy system.

Slit width	w_e	10 μm - 12 mm		
Grating	g/mm	300	1200	2400
Reciprocal dispersion	$D_\lambda(\text{nm/mm})$	9.854	2.334	1.017
Central wavelengthl	λ_{central} (nm)	378	378	378
Gain	G	1-100		
Effective gain	G_{eff}	f(G) measured experimentally		
Gate width time	τ_{width}	1 μs - a few ms		
Number of accumulations	N_{acc}	1 - hundreds		
Exposure time	τ_{exp}	$\tau_{\text{exp}} = \tau_{\text{width}} \cdot N_{\text{acc}}$		
Line height (in pixels)	Δy_p			
Readout rate		2 or 8 MHz		

The above listed parameters have allowed to determine the coefficient $a(\lambda, T)$ given by the following equation:

$$a(\lambda, T) = \frac{S_0(\lambda, T)}{w_e \cdot G_{\text{eff}} \cdot \tau_{\text{exp}} \cdot \Delta y_p \cdot \alpha_T \cdot L_0(\lambda, T)} \quad (3.33)$$

It highlights that the sensitivity calibration of a spectrographic system has been done for the complete system, not separately for the individual components. $a(\lambda, T)$ has been obtained by the averaging of 21 spectra in case of the measurements for readout rate of 2 MHz and 15 spectra for 8 MHz. Then, $a(\lambda, T)$ has been estimated by the regression analysis, as follows:

$$E = \sum_{\lambda_i} \left(L_0^G(\lambda_i) - b \frac{L_0^{G_{\text{ref}}}(\lambda_i)}{G_{\text{ref}}} \right)^2 = 0 \quad (3.34)$$

where:

- $L_0^G(\lambda_i)$ is the spectral radiance of the tungsten strip lamp for given gain, G, and wavelength, λ ,
- G_{ref} the referential gain,
- b the estimated constant.

The presented Equation 3.34 is determined for the measurements obtained for variable gain, G . The same procedure has been applied to the results obtained for the following parameters: τ_{exp} , w_e . Figure 3.36 presents the measured exposure time, τ_{exp} , in a function of the theoretical τ_{exp} . It highlights the linear response of the ICCD detector.

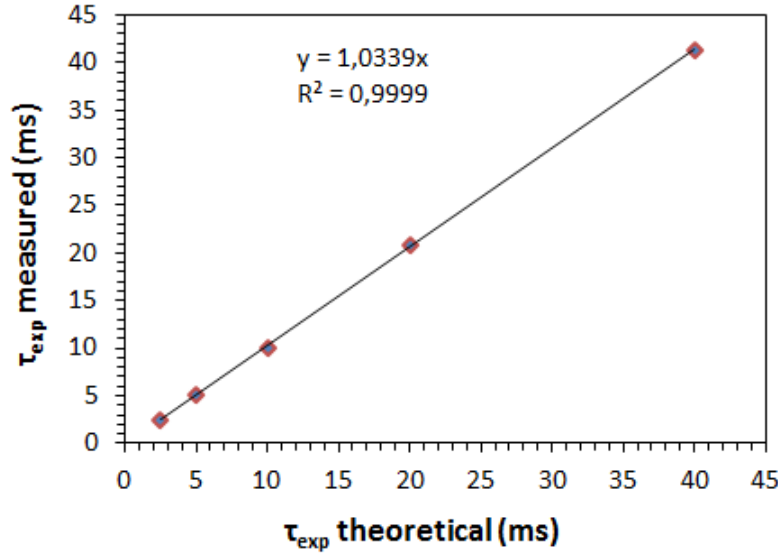


Figure 3.36: Calibration curve measured for variable exposure time τ_{exp} .

The same characteristics have been obtained for the slit width, w_e , and the gain. The calculation of the coefficient $a(\lambda, T)$ has allowed to define the calibrated radiance of plasma given by:

$$L_{plasma}(\lambda, T) = \frac{S_{plasma}(\lambda, T)}{a(\lambda, T)} \frac{1}{w_e' \cdot G_{eff}' \cdot \tau_{exp}' \cdot \Delta y_p'} \quad (3.35)$$

where w_e' , G_{eff}' , τ_{exp}' , $\Delta y_p'$ are parameters of the system for the plasma spectroscopic measurement.

III.3 Investigation of the plasma species

To determine the plasma temperature, the optical emission spectroscopy has to be applied to examine the species of the pulsed plasma jet produced by the "Mosquitorch". The pure nitrogen (N_2 2 slm) has been used as plasma forming gas, therefore, the spectroscopic studies have been focused on the identification of N_2 molecular emissions. In the previous paragraphs the partial energy level diagram based on the data of Gilmore *et al.* for N_2 , N_2^+ and N_2^- states versus their internuclear distance (R) in Figure 3.31 has been presented.

The use of this diagram allows to determine the following transitions in the nitrogen plasma:

- $N_2(C - B)$

The $N_2(C^3\Pi_u - B^3\Pi_g)$ system (the second positive system of nitrogen) with the vibrational branches ranged between 280 and 500 nm, where the head of the (0,0) vibrational transition is at 337 nm. The second positive system is often responsible for the dominant emission in air or N_2 -containing plasmas.

- $N_2^+(B - X)$

The $N_2^+(B^2\Sigma_u^+ - X^2\Sigma_g^+)$ system (the first negative system of nitrogen) is often observed in air and nitrogen-containing ionizing plasma. The (0,0) vibrational transition is usually the strongest band, observed at 391.4 nm. The rotational lines of this system are often used to determine the rotational and vibrational temperatures of the plasma, as presented in [89,90]. Therefore, initially, this system will be chosen to define the plasma temperature in the following experiments.

Figure 3.37 highlights the identification of the emission features in the plasma produced by the "Mosquitorch".

The spectra have been obtained by non-time-resolved acquisition, choosing the gate width time, τ_{width} , of 7 ms which is equal to 10 periods, T , of the pulsed plasma jet (T of 700 μs), what results in the average spectra of the modulated plasma. To determine a broad wavelength range of the spectra 300 g/mm gratings and the slit width of 75 μm have been chosen. Moreover, the function "step and glue" provided by LightField software has been used, what allows to measure large wavelength ranges. By this function the broad measurement range is divided to the series. After the acquisition of the particular spectral sequence, the grating moves to measure the other series and, then, the spectral measurements are glued together to create a single spectrum. It has to be mentioned that the intensity of the spectra has been normalized in order to compare the measurements.

The spectra have been obtained for different distances from the nozzle exit, where 0 mm corresponds to the exit of the torch. The analysis of the species performed by Speciar software and presented in Figure 3.37 highlights that the plasma jet from 0 to 10 mm contains mainly the transitions: $N_2(C - B)$ and $N_2^+(B - X)$. It has to be mentioned that the second positive system of N_2 and the first negative system of N_2^+ are frequently observed simultaneously. Moreover, at the nozzle exit the spectrum contains the atomic lines of nitrogen, what can be explained by the flow of N_2 plasma forming gas. In the spectrum measured in 10 mm CN violet system ($B^2\Sigma_u^+ - X^2\Sigma_g^+$) at 388 nm has been observed, what demonstrates the mixing of the plasma jet with the surrounding air that contains the trace of CO_2 .

III.4 Temperature measurements

As has been highlighted in the previous paragraphs the time-resolved optical emission spectroscopy has been applied in a newly developed system of the suspension phased injection in pulsed arc jet to determine the temperature of the modulated plasma. The gas temperature measurements are mainly obtained by emission spectroscopy from the population distribution in rotational levels, what is generally close to the kinetic gas temperature as presented in [89–92]. The previously highlighted investigation of the plasma species has shown the possibility of the use of the first negative $B^2 \Sigma_u^+ - X^2 \Sigma_g^+$ system of N_2^+ .

Therefore, the spectral measurements have been focused on $N_2^+(B^2 \Sigma_u^+ - X^2 \Sigma_g^+)$ system, which is a blue-degraded system with a head band at 391.4 nm. The 1200 g/mm grating has been used with the slit width of 300 μm corresponding to around 0.7 nm spatial resolution. The gate width, τ_{width} , has been regulated to 60 μs . Considering the plasma velocity of $\sim 50\text{m.s}^{-1}$, the plasma moves only by 3 mm during the time of 60 μs . Smaller values of τ_{width} have resulted in the increase of On-CCD accumulation number, N_{acc} , and also on the increase of the signal/noise ratio. Therefore, the compromise has to be found between the exposure time, i.e. the signal/noise ratio and the temporal window during which the plasma is observed for measurement with frozen properties.

III.4.1 Spectral simulations

In the frame of this thesis, the measured spectra have been analysed by Specair. It is a commercial software developed to simulate the radiative, molecular and atomic transitions in air plasma, including N_2 (second positive system), N_2^+ (first negative system), CN (violet system). Specair assumes that the rotational states are Boltzmann distributed at T_{rot} , defined by the equation (3.29). According to Bruggeman *et al.*, this condition is fulfilled if N_2 effective lifetime of the excited state, τ_{eff} , is longer than N_2 time of thermalization, τ_{therm} [91]. The latter can be evaluated by calculating the elastic collision frequency of N_2^+ and assuming about 10 collisions to reach the thermalization. In the range of expected temperature, $\tau_{\text{therm}} \simeq 10$ ns. The time τ_{eff} is defined as follows:

$$\tau_{\text{eff}} \simeq \frac{1}{\sum_v A_{Xv'}^{Bv'}} \quad (3.36)$$

where $A_{Xv'}^{Bv'}$ is the transition probability between $B^2 \Sigma_u^+$ and $X^2 \Sigma_g^+$ states of N_2^+ for the $\Delta v = 0$ vibrational bands, which can be found in [93]. It has been found that $\tau_{\text{eff}} \simeq 80$ ns.

Consequently, in the following measurements the Boltzmann distribution will be assumed and also $T_{\text{gas}} = T_{\text{rot}}$.

To define the rotational temperature, T_{rot} , the theoretical spectrum has to be simulated by Specair and compared to the measured one. This procedure consists of several stages. Firstly, the background subtraction has to be implemented. It is the method which minimizes the noise in the spectral measurements and thus makes small peaks more visible. The noise can be caused by the plasma continuum radiation or the dark current (background current that flows in a CCD camera system). Figure 3.38 presents two spectra of (N_2^+) first negative system: spectrum before the background subtraction (in red) and after that.

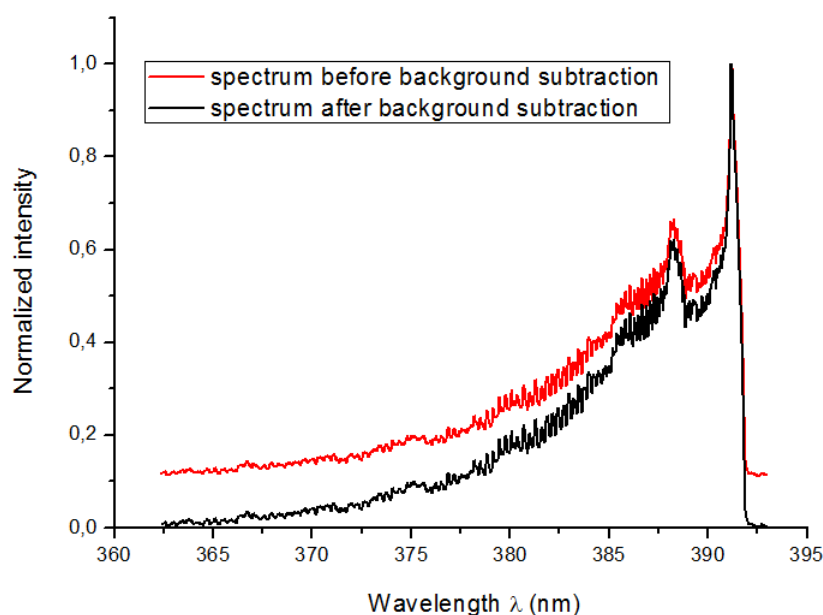


Figure 3.38: Effect of the background subtraction.

It can be noticed that the noise of the background is determined on the level of around 0.1. The background subtraction plays an important role in the intensity calibration procedure, where this noise signal can be magnified and deform spectral measurement, because the calibration function $a(\lambda, T)$ depends on λ . Therefore, during calibration procedure the background has been subtracted from the measurements. Moreover, it can be noticed that the obtained spectra have been normalized to a maximum value of 1 by Specair software due to different intensity levels. This procedure permits to compare the spectra.

The spectra presented in Figure 3.38 have been obtained before the calibration of the system of the wavelength axis. Therefore, they had to be also corrected in x (wavelength) scale. This procedure permits to recalculate the measured data in order to compare with other spectra or to define the unknown transitions in a spectrum by the Specair database.

Moreover, wavelength corrections are necessary to optimize the fitting of experimental spectra.

As has been presented above to obtain precise information about the plasma parameters as the gas temperature the calibration of the wavelength and intensity axis have to be performed.

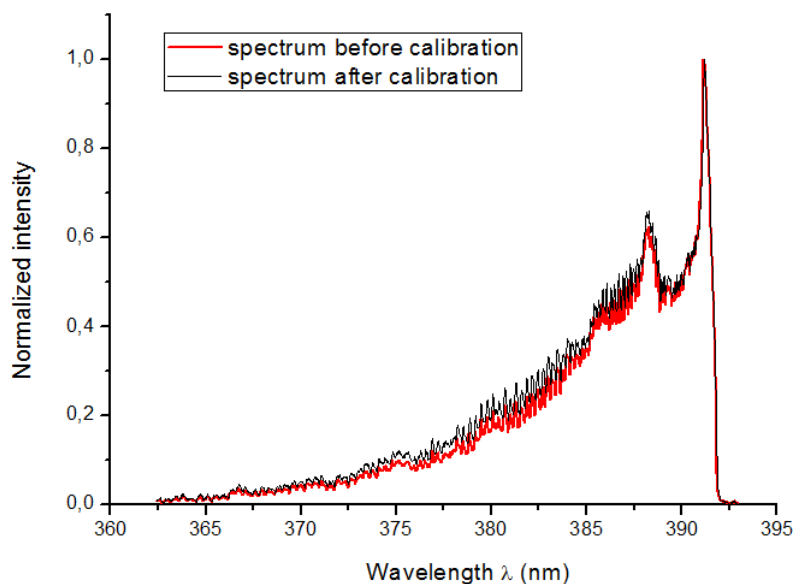


Figure 3.39: Effect of the calibration.

Figure 3.39 presents two measured spectra of (N_2^+) first negative system: spectrum before implying the calibration procedure (in red) and after that. As can be noticed the intensity levels of the rotational lines are lower in the case of non-calibrated spectrum. It has resulted in the difference of the temperature measurements: 7500 K defined for the spectrum obtained by the calibrated system and 6800 K measured in the case of the second spectrum. Therefore, it highlights that the calibration procedure has the importance in the spectral measurements.

The important parameter in the spectral simulation by Specair software is the determination of the instrumental function which defines the resolution of the collected data. The slit function represents the broadening caused by the spectrometer (slit width, pixel width, grating dispersion). The measured spectrum, I_{measure} , is the result of the convolution of the real emitted radiance, I_{plasma} , and the slit function SL as presented by the relation: $I_{\text{measure}}(\lambda) = \int_0^\infty I_{\text{plasma}}(\xi) SL(\lambda - \xi) d\xi$. To ameliorate the accuracy of the spectral measurements, two different slit functions have been chosen: the trapezoidal function, proposed in the literature [84,94] and presented in Figure 3.40, and the function determined by measuring Hg lamp at 404.7 nm.

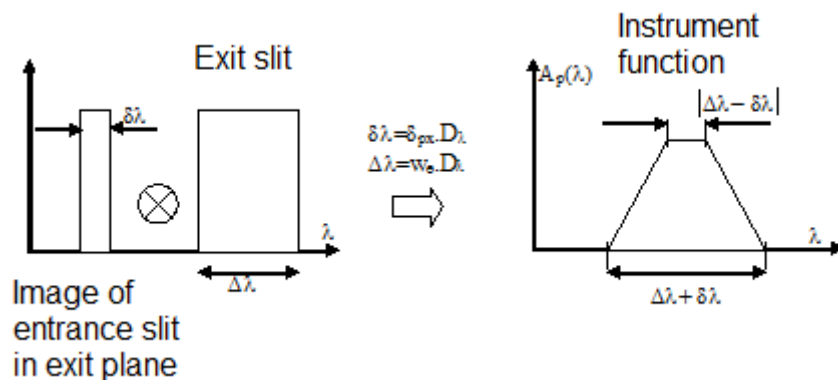


Figure 3.40: Slit function of the spectroscopy system.

Figure 3.40 illustrates the procedure of the determination of the trapezoidal slit function. The spectral width of the exit slit is presented as $\Delta\lambda$ and the width of the image of entrance slit in exit plane as $\delta\lambda$. It should be assumed that the width of the exit slit should be larger than $\delta\lambda$ in order to not lose any flux. While scanning the exit slit across the spectral image a trapezoidal shape of the recorded line is obtained, what represents the slit function for given settings of entrance and exit slits.

To compare the accuracy of spectrum fitting by Specair software, the alternative slit function has been determined by recording the line profile of the emission from a low-pressure Hg lamp at the wavelength of 404.7 nm, presented in Figure 3.41. It allows to obtain the slit function in good approximation due to a small line width of the lamp (~ 1 pm FWHM).

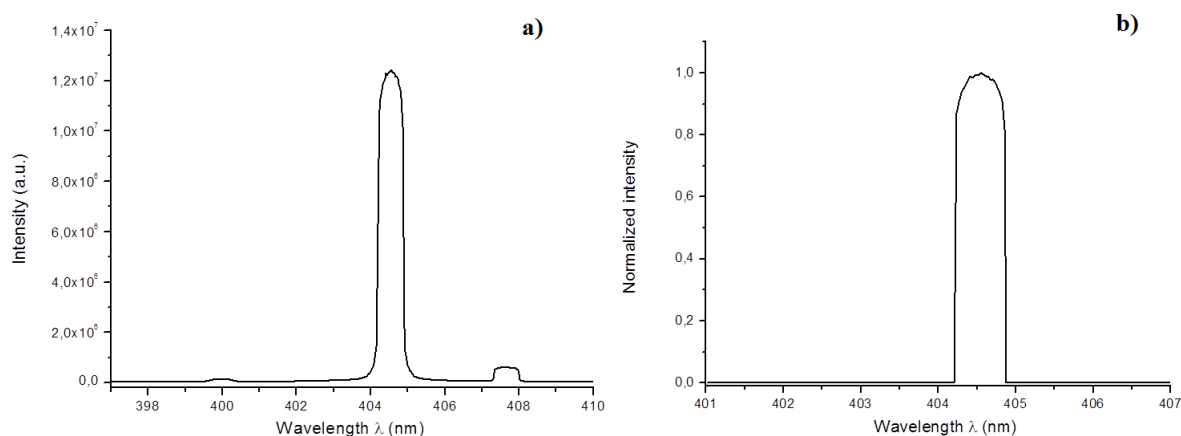


Figure 3.41: Slit function determined by measuring Hg lamp: a) measured spectrum, b) normalized spectrum to avoid the artifacts ($w_e = 300 \mu\text{m}$).

The measured spectrum, 3.41 a), has been normalized to the format given by Specair software, 3.41 b), to avoid the artifacts of the spectrum fitting. To ameliorate the accuracy, recorded line profile has been fitted to the rotational spectrum of the measured (N_2^+) first negative spectrum, presented in Figure 3.42.

Bruggeman *et al.* have shown that for a broad slit opening the trapezoidal instrumental function should be considered and for a small entrance slit the recorded line shape can be approximated by a measured function [91].

As has been mentioned the presented above spectra have been measured with a spectral slit width, w_e , of 300. Therefore, the trapezoidal instrumental function has been applied in the Specair simulations.

The apply of all procedure mentioned above permits to determine the rotational temperature of the plasma by numerical optimization routines provided by Specair software which lead to the adjustment of measured spectrum to that simulated by Specair. Figure 3.42 presents the comparison between the measured and simulated (N_2^+) first negative spectra.

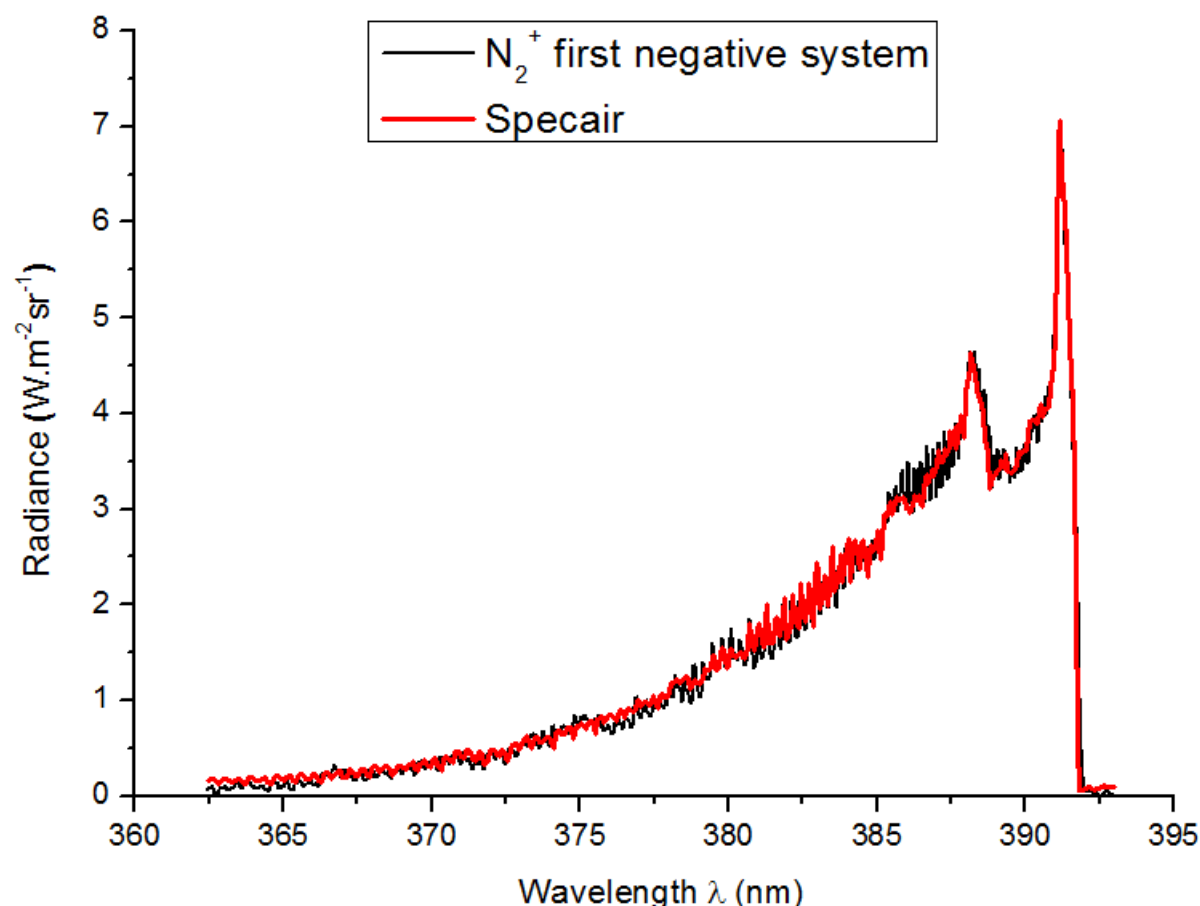


Figure 3.42: Comparison of the measured and simulated by Specair software (N_2^+) first negative spectra.

As can be observed, a good agreement between these two spectra has been obtained. This best correspondence of the simulated spectrum to that experimental provides the rotational temperature. All presented experimental procedures and simulations allow to precisely determine the temperature of the pulsed plasma jet, what will be highlighted in the following section.

III.4.1.1 Determination of the temperature of pulsed plasma jet

As has been shown in the previous paragraphs the time-resolved optical emission spectroscopy is used to determine the temperature of the pulsed plasma jet, characterized by high modulation of the specific enthalpy. To verify the temperatures of different stages of this modulated plasma, the time-resolved spectroscopy measurements have to be synchronized with the arc voltage signal, what is presented in Figure 3.43.

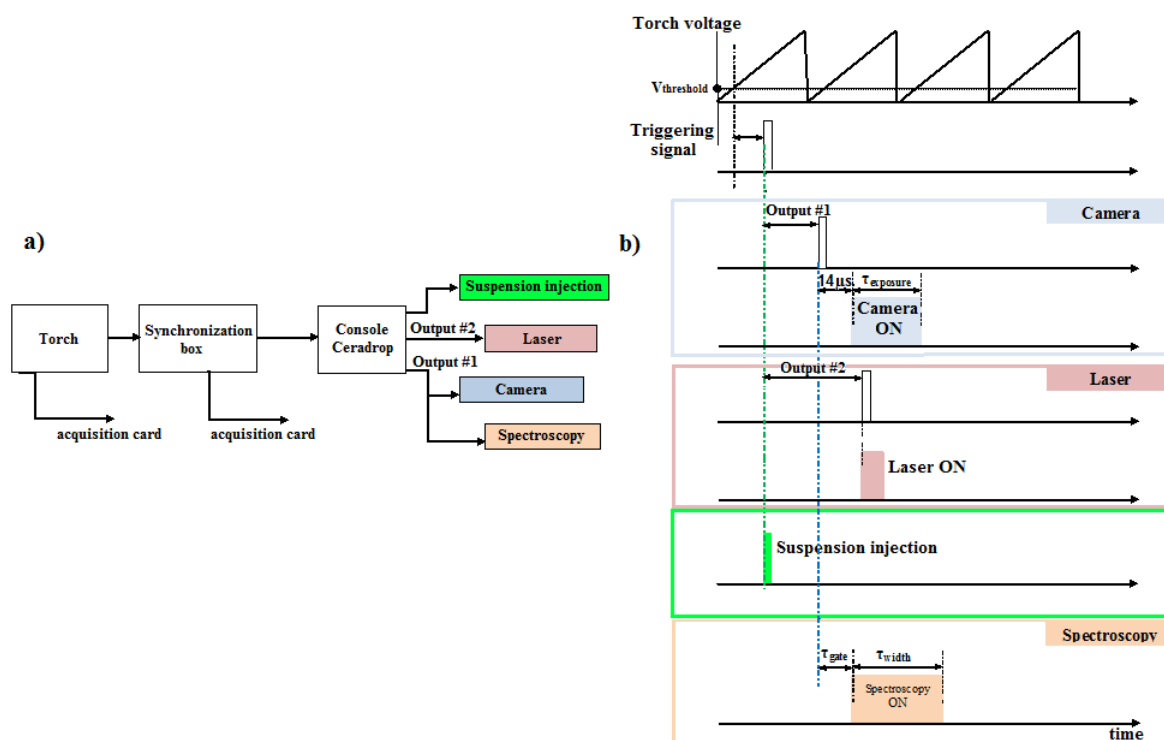


Figure 3.43: Schematic view of the synchronous time-resolved spectroscopy procedure: a) the experimental setup, b) the timing diagram.

The spectrograph has been connected to the output 1 of Ceradrop platform. The synchronization procedure is similar to this one of time-resolved imaging and suspension injection. The TTL signal formed from the arc voltage is sent to Ceradrop console which activates the spectroscopic measurements. The spectrograph is synchronized with the camera by adjusting the delay time, τ_{gate} , to 14 μs .

To verify the temperatures of different stages of the modulated plasma, four moments presented in Figure 3.44 have been chosen. The triggering signals have been formed from the arc voltage and sent to camera and TROES, as presented above, in order to obtain the synchronized measurements.

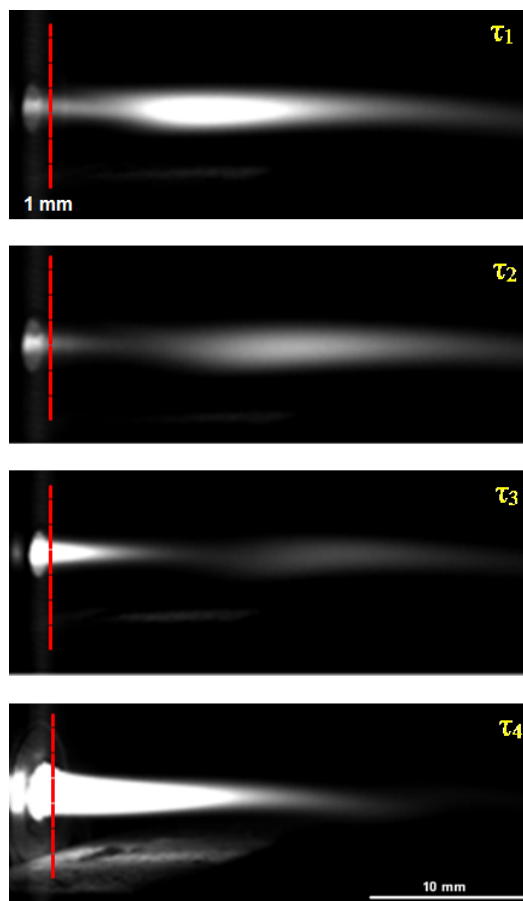


Figure 3.44: Time-resolved imaging of the spectral measured moments of the pulsed plasma jet: τ_1 to τ_4 . The spectra obtained 1 mm from the nozzle exit, marked on the photos.

The trigger time delays in one plasma period, τ_1 to τ_4 , have been adjusted by the synchronization box. The generated TTL signals have been sent to the camera and the spectrograph. Moreover, they have been recorded by LabView software, what is given in Figure 3.45. These measurements highlight that the moment of the pulsed plasma, τ_4 , corresponds to the maximum voltage signal, $U_{\max}(t) = 100$ V. In the comparison, τ_1 is obtained at $U(t) \simeq 60$ V.

The measured spectra, presented in Figure 3.46, have been processed by Specair software, by applying the procedures mentioned above, to obtain the plasma temperatures, indicated in Figure 3.46.

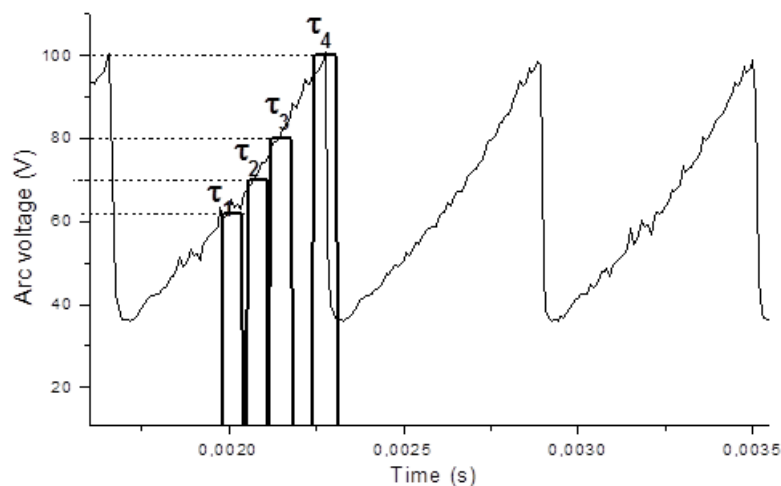


Figure 3.45: The trigger signals, τ_1 to τ_4 , of the pulsed plasma moments presented in Figure 3.44, sent to the Time-Resolved Optical Emission Spectroscopy.

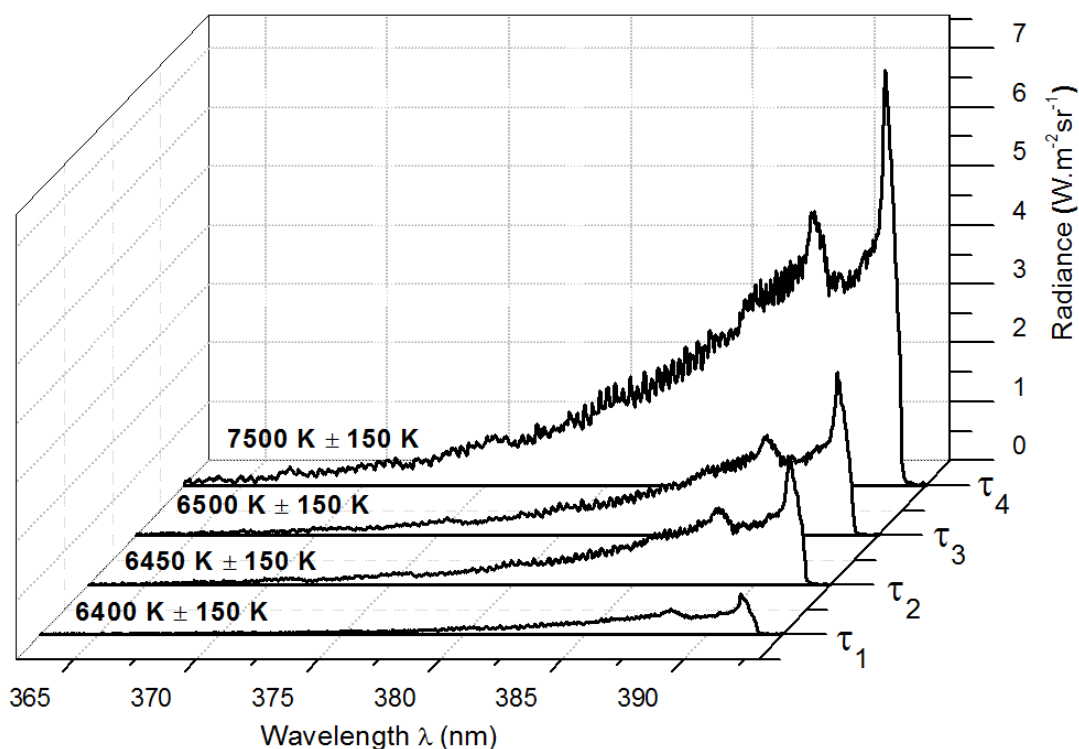


Figure 3.46: (N_2^+) first negative spectra for four different moments, τ_1 to τ_4 of the periodic arc voltage.

Analyzing the N_2^+ first negative system, it can be observed that the spectrum measured in the moment τ_4 is characterized by the highest value of the intensity comparing to the spectra obtained at τ_1 to τ_3 .

The spectroscopic estimation of the rotational temperature highlights that the gas temperature increases from $6400 \text{ K} \pm 150 \text{ K}$ to $7500 \text{ K} \pm 150 \text{ K}$ by changing the moment of a periodic arc voltage, as is presented in Figure 3.46. The obtained results can be compare

with the data of the specific enthalpy of the nitrogen plasma given in [17] and gathered in Figure 3.47. The region distinguished in the figure corresponds to the dissociation of N_2 molecule resulting in a steep change of the enthalpy in a small range of temperature.

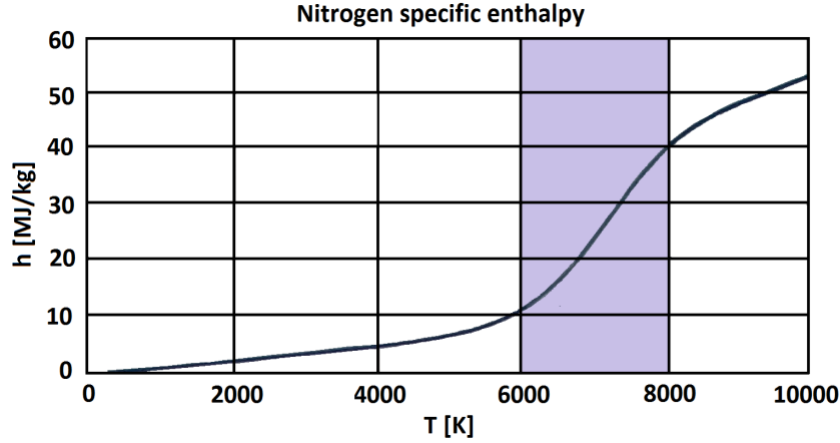


Figure 3.47: The nitrogen specific enthalpy based from the data given in [17].

The comparison of the obtained results with the nitrogen enthalpy data, shown in Figure 3.47, highlights that the plasma jet analyzed at the moment τ_4 is characterized by the enthalpy value of 35 ± 3 MJ/kg. To compare, at the moment τ_1 the enthalpy is of 15 ± 2 MJ/kg. It proves experimentally that the pulsed plasma jet is characterized by the enthalpy and the temperature modulated. However, the ratio of the enthalpy modulation $h_{\tau_4}/h_{\tau_1} \simeq 2.3$ obtained in this experiment is much lower than that presented in the previous section, $h_{\max}/h_{\min} \simeq 18$, determined by the energy balance measurements and the hypothesis about constant thermal voltage (36 V). This significant difference has led to the conclusion that the enthalpy modulation ratio of around 18 is overestimated because the thermal losses are not constant. The assumption of the fluctuating thermal losses has given the estimated ratio h_{\max}/h_{\min} of around 2.

Moreover, the presented method to determine the plasma temperature has encountered the difficulties in the spectroscopic measurements of the moment of the pulsed plasma jet, which corresponds to $U_{\min}(t) \simeq 40$ V. This instant of the jet is characterized by a weak plasma radiation, therefore the precise determination of the rotational temperature, in this case, following N_2^+ negative system is not relevant.

Furthermore, it has to be mentioned that despite the setup calibration and the determination of the instrumental function procedures, the errors in the temperature measurements have occurred, what is indicated in Figure 3.46. To improve the measurements, the researchers apply the Abel inversion technique to obtain radially resolved emission profile, from which the temperature profile can be deduced. However, this method requires the assumptions that the plasma jet is optically thin and it is

characterized by the axial symmetry. The results obtained by the pulsed plasma jet have highlighted that this kind of plasma does not meet these assumptions. As Tanaka and *et al.* have shown in this case the Abel inversion is not useful because can engender the higher error [95]. Moreover, the errors in the temperature measurements, highlighted above, do not influence significantly on the determination of the specific enthalpy.

As has been already mentioned, the purpose of plasma spraying is the production of the coatings. Therefore, the material injected to the plasma torch has to be melted, what requires the heat transfer. The following measurements have been performed to define the level of the enthalpy and the temperature of the plasma at the moment of the suspension injection to the plasma jet. Figure 3.48 indicates the location at which the suspension droplet is inserted, 5 mm. To compare the results the plasma has been also measured in the distance of 1 mm from the nozzle exit.

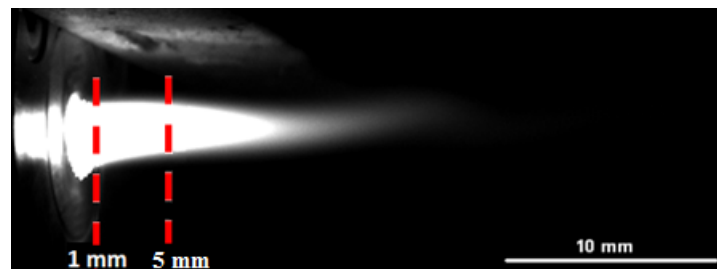


Figure 3.48: Time-resolved imaging of the spectral measured moment of the pulsed plasma jet, τ_4 in Figure 3.45. Two distances, 1 and 5 mm, from the torch exit indicated.

The same synchronization procedure, as mentioned above, has been applied. The moment of the pulsed plasma, which corresponds to the maximum voltage signal, $U_{\max}(t) = 100$ V, has been chosen.

Analyzing the obtained N_2^+ spectra, it can be observed that the spectrum measured in 1 mm is characterized by the higher value of the intensity than the spectrum detected in 5 mm.

It can be explained by analyzing the cross-section of the plasma jet in Figure 3.48. In the distance of 1 mm the radiance of the plasma is higher than in 5 mm. Moreover, the measured temperature decreases from $7500 \text{ K} \pm 150 \text{ K}$ to $6900 \text{ K} \pm 150 \text{ K}$, when the distance from the torch nozzle exit increases. It results in the decrease of the enthalpy from $35 \pm 3 \text{ MJ/kg}$ to $23 \pm 2 \text{ MJ/kg}$. However, the obtained enthalpy level is sufficient to obtain the material melted in this region of the plasma jet and to form the coatings, what will be presented in the next paragraph.

The presented sections have highlighted the possibility to use the time-resolved optical emission spectroscopy to measure the temperature of the pulsed plasma jet produced

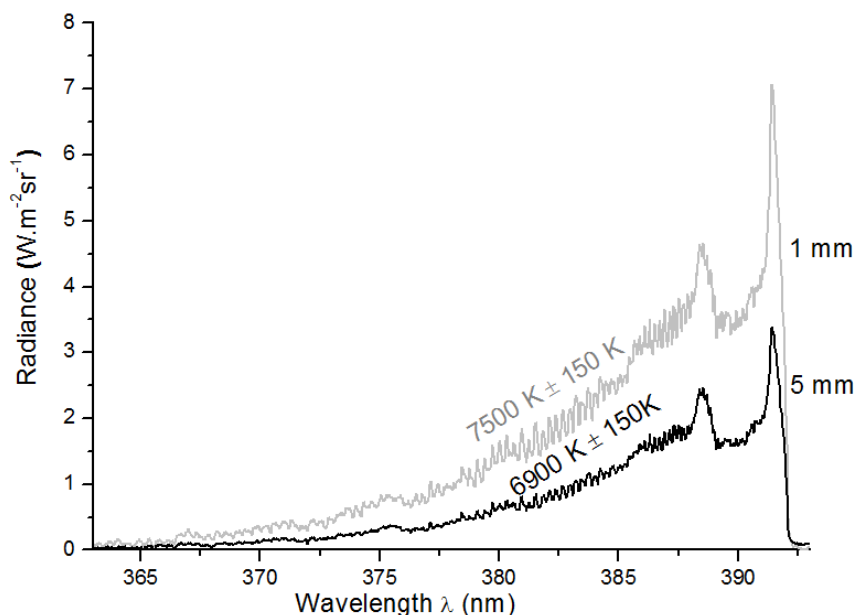


Figure 3.49: (N_2^+) first negative spectra measured at the distance of 1 mm and 5 mm from the nozzle exit.

by the "Mosquitorch". The results have highlighted that the careful choices of the experimental procedure and the spectral simulation process are the important parameters in the spectroscopic measurements. The selection of the system plays also the significant role in this type of the diagnosis. The use of the time-resolved optical emission spectroscopy has allowed synchronizing the system with the pulsed plasma jet what has resulted in the temperature measurements of different moments of this periodic plasma. Moreover, by analyzing the experimental results with the data of the nitrogen plasma it has been possible to obtain the local specific enthalpy of different moments of the plasma jet. The presented measurements have verified the high modulation of the specific enthalpy in the pulsed plasma. The following section will present the use of this periodic plasma to obtain the first coatings by a new system, the suspension phased injection in pulsed arc jet.

IV Material deposition

The following paragraph describes the first attempts to deposit the material by a new system, the suspension phased injection in pulsed arc jet.

In the conventional SPS method the spray parameters, as the plasma and suspension characteristics but also the spray distance, the substrate preparation and the substrate cooling, determine the properties of the obtained coatings. For several years, the researchers have been developing these parameters, what can be found in the large

number of works [3, 13, 14, 54, 96–98]. To obtain the first coatings by a new method it has been decided to follow the experimental conditions for the suspension plasma spraying. However, it can be noticed that the synchronized SPS with pulsed arc jet method differs from the conventional SPS process, what is presented in Table 3.7.

Table 3.7: Comparison of injection features for conventional SPS with the mechanical injection and the high power plasma torch (~ 35 kW) and for suspension phased injection with mosquitorch (~ 1 kW).

	Droplets diameter (μm)	Injection velocity (m.s^{-1})	Suspension flow rate (ml.min^{-1})	Powder mass flow rate (g.min^{-1})
Conventional SPS	~ 300	~ 25	~ 20	~ 3
Synchronized SPS	50	3.26	5.6×10^{-3}	3.4×10^{-4}

The suspension is injected with lower velocity. Moreover, the suspension and powder mass flow rates are much smaller than in the conventional system using the mechanical injection. On the other hand, the Mosquitorch is supplied by much lower power than the conventional torch. It has to be mentioned that this low power plasma torch, combined with the pure nitrogen characterized by good properties in thermal transfers, is sufficient to treat the materials, as the previous results have highlighted. Therefore, the following spray parameters have been chosen:

- the spray distance of 32 mm from the torch exit

The spray distance in the conventional plasma spraying using the powder is of around 100 mm. However, as Darut *et al.* have highlighted in the SPS method this parameter has to be drastically lowered to about 30 mm due to the significantly lower momentum and thermal inertia of the material particles [99].

- the substrate cooling

The rotating sample holder has been chosen, what allows to avoid the overheating of the substrate. The linear speed of the holder has been regulated to 1 ms^{-1} , by analyzing the studies presented in [100, 101].

- the substrate preparation

To collect the splats produced by SPS method the mirror-polished substrate is commonly used due to its low roughness. Therefore, the stainless steel substrates have been polished using water-cooled silicon carbide (SiC) papers with the grit sizes of 600, 1200, 2400 and $4000 \mu\text{m}$. Then, the final mirror-like surface has been obtained by using the velvet polishing pad and colloidal silica. The substrates before the spraying process have been cleaned in the ethanol and dried with the argon stream.

To obtain the deposition of the material the aqueous suspension of TiO_2 , described in

Table 3.2, has been used. In the experiments presented in the previous paragraphs the exact moment of the suspension emission synchronized with the periodic arc voltage signal has been studied. However, to obtain the coatings using the suspension phased injection in pulsed arc jet the moment of the suspension-plasma interaction has to be determined.

To protect the injector from the plasma heat flux it has been supported by a water-cooled screen and mounted in the distance of 5 mm from the plasma jet axis. Therefore, the time of the flight of suspension droplet from the injector to the plasma has to be defined. Knowing that the distance is 5 mm and taking into consideration the experimental result of the suspension droplet velocity equal to 3.26 m.s^{-1} , the material flight time, t_{flight} , is around $2 T$, where T is the arc voltage period. The obtained results highlight that the suspension is treated by the plasma two periods after the suspension droplet emission.

The characterization of the deposited material is an important step in plasma spraying method to e.g. select the parameters of the process, improve the method. Therefore, to study these first obtained coatings the basic measurements of the structural characteristics have been performed. To observe the structure of the coating and the particles of the diameters $d > 1 \mu\text{m}$ the optical microscopy has been used. To obtain the microstructure of the coating with better precision the Scanning Electron Microscopy (SEM) has been applied combined with Energy Dispersive Spectroscopy (EDS) which gives a spatially resolved compositional analysis of the coating. The following sections give the description of these methods and highlight the microstructure of the obtained splats.

IV.1 Optical microscopy

The optical microscopy examination allows for basic observations of the coatings structures. It should be a first instrument to be used for metallographic observations since it is faster and much less expensive than e.g. Scanning Electron Microscopy (SEM). Moreover, the optical microscopy compared to other techniques allows to observe large area of the sample. It is a type of microscope which uses visible light and a system of lenses to magnify images of small samples. In the frame of the thesis the coatings have been observed by polarizing microscope Eclipse LV 100 POL (Nikon, Japan) which permits to observe the samples with objective magnifications: 5x, 10x, 20x, 50x and 100x. One of the key parameters of the optical microscopy measurement is image contrast, which depends on the quality of the optics, coatings on lenses and reduction of flare and glare. The microscope Eclipse is equipped with a high intensity 50W halogen light source and a fly-eye lens design what gives brighter, clearer and higher contrast images.

The important parameter of optical microscopy is the image resolution which corresponds to the ability to see fine details, presented in Figure 3.50.

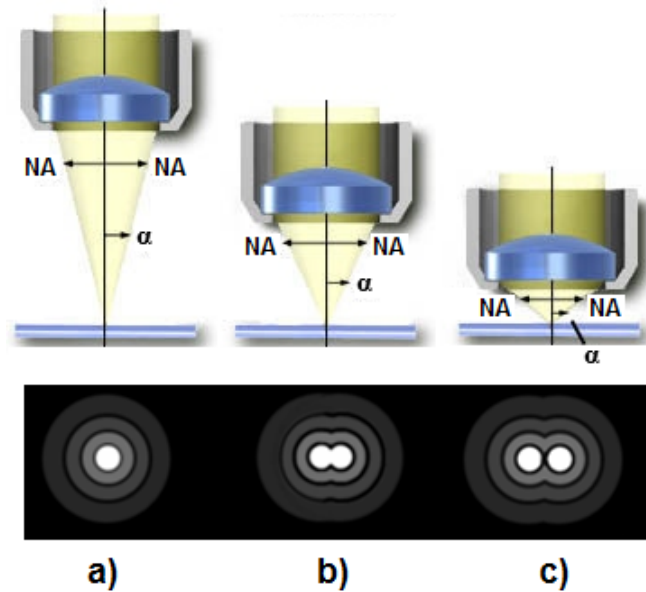


Figure 3.50: Resolving two adjacent points: a) $\alpha = 7^\circ$, $NA = 0.12$, b) $\alpha = 20^\circ$, $NA = 0.34$, c) $\alpha = 60^\circ$, $NA = 0.87$.

It is defined by the smallest distance, r , between two points which can be resolved, as follows:

$$r = 1.22 \frac{\lambda}{2NA_{obj}} \quad (3.37)$$

where:

λ is the wavelength of the light,

NA_{obj} the objective numerical aperture defined by equation:

$$NA_{obj} = n \cdot \sin \alpha \quad (3.38)$$

where:

α is a half-cone angle of light half captured by the objective lens,

n the lens refractive index.

The other important characteristic of optical microscopy is the depth of field, D , area in front of and behind the specimen that will be in acceptable focus. The depth of field is related to the wavelength of the light and to the numerical aperture (NA), as follows: $D = \lambda/NA^2$.

IV.2 Scanning electron microscope (SEM)

The Scanning Electron Microscopy is a method which uses electrons instead of light to form an image. The electron beam with an energy ranging from 0.5 to 40 keV is thermionically emitted from an electron gun, what is schematically presented in Figure 3.51. Then, the electron beam is focused by condenser lenses. In the final lens, the beam passes through pairs of scanning coils or deflector plates which deflect the beam in the x and y axes, what results in scanning over a rectangular area of the sample surface.

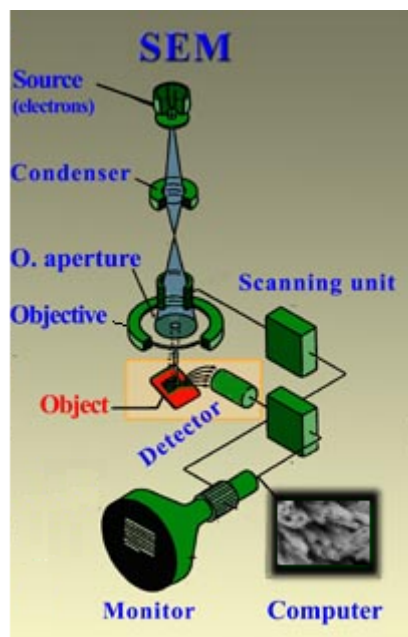


Figure 3.51: Schematic view of a Scanning Electron Microscope.

This electron beam carries significant amount of kinetic energy, what is dissipated as a variety of signals produced by electron-sample interactions. These signals include secondary electrons (which give SEM images), backscattered electrons (BSE), photons (X-rays which are used for elemental analysis, can be detected in SEM equipped with energy-dispersive X-ray spectroscopy), visible light (cathodoluminescence-CL) and heat. Secondary and backscattered electrons are commonly used for imaging the sample. Secondary electrons are most valuable for showing morphology and topography of the sample. Backscattered electrons are used for illustrating contrasts in composition in multiphase sample.

To characterize coatings produced in the frame of this thesis JEOL 7400F microscope has been used (JEOL, Tokyo, Japan). It is a scanning electron microscope equipped with a Cold Field Emission Gun (FEG). It is designed for the analysis of the physical and chemical microstructure of solid state materials at nanometer resolution (max. resolution: 1 nm). It additionally allows for spatially resolved compositional analysis by using the

PGT Energy Dispersive Spectroscopy (EDS).

As a consequence of the use of the vacuum conditions and electrons to form an image in SEM method, the samples have to be specially prepared. The metals as the conductive materials require no preparation before the measurement. All non-metal samples have to be covered by a thin layer of conductive material. The automatic sputter coater (Agar Scientific, Stansted, UK) has been used in the experiments to cover TiO₂ coatings with platinum.

IV.3 Microstructure of deposited material

The following section presents the first basic characterizations of the obtained coatings microstructures. The purpose of these studies is to verify the spraying parameters and develop the coatings deposition process.

The spray distance of 32 mm has been chosen by analyzing the results obtained by SPS method. Therefore, to verify this choice for synchronized SPS process this parameter has been increased to 42 mm.

Figure 3.52 shows the examination of the influence of the spray distance on the coatings microstructure. It has to be highlighted that it presents the basic study by the optical microscope.

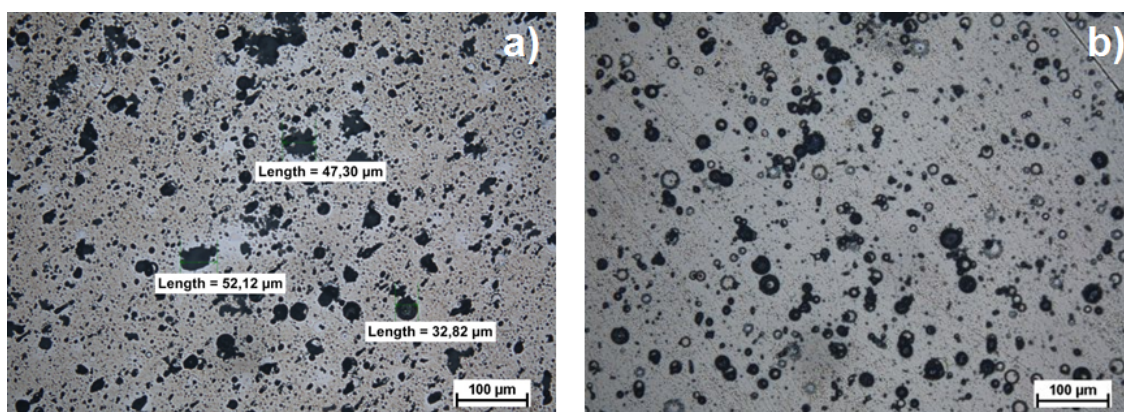


Figure 3.52: Microstructure of the coating obtained at the distance: a) 32 mm, b) 42 mm. The measurements performed by the optical microscope, using the objective magnification 20x.

The first photo, 3.52 a), gives the microstructure of the coating obtained at the distance of 32 mm. Figure 3.52 b) shows the results of increasing this spraying parameter to 42 mm. It has to be mentioned that both coatings have been produced by the injection of the suspension droplets at the moment of the pulsed plasma corresponding to maximum voltage signal. Figure 3.52 a) highlights that the coating is composed of two different zones: uniform light area which gives the impression of being fine and nanometric, the

dark elements of large sizes up to around $50 \mu\text{m}$. The increase of the spraying distance to 42 mm , presented in Figure 3.52 b), mainly results in dark elements which have different structures than these ones presented in Figure 3.52 a). Moreover, the characteristic feature of the substrate surface can be observed, what means that the distance between the torch and the substrate is too long and the resolidified particles can be mainly observed. The obtained results highlight the importance of the choice of the spraying distance, which will be regulated to 32 mm in the following experiment.

In the previous experiment the suspension droplet has been emitted at the maximum level of the arc voltage signal. To determine the influence on the coatings formation of the different moments of the pulsed plasma jet, two cases have been chosen related to the spectroscopic measurements of the plasma: the suspension emission at the maximum level of the arc voltage signal, presented in Figure 3.44 as τ_4 and the medium level, indicated in Figure 3.44 as τ_1 . Figure 3.53 presents the coatings characterizations performed by the optical microscope.

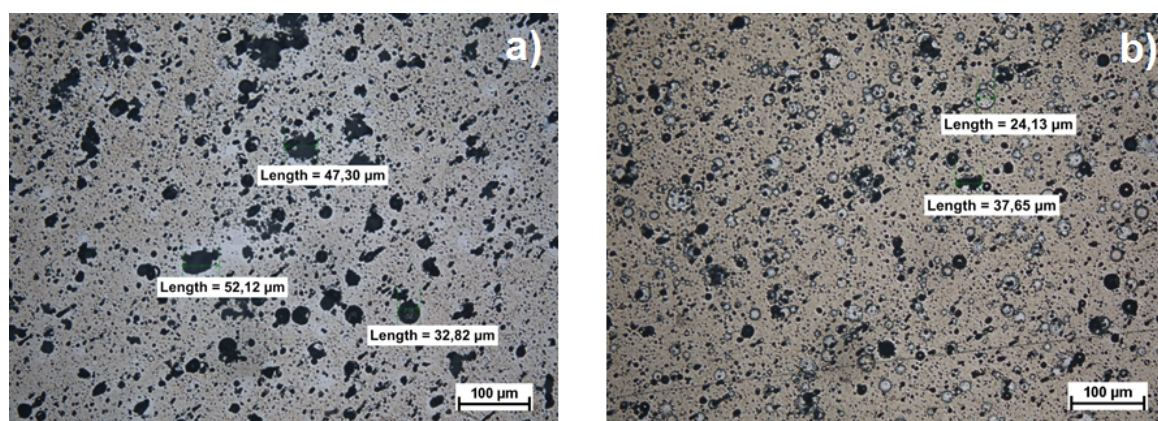


Figure 3.53: Microstructure of the coating obtained at the moment corresponding to: a) maximum voltage signal, b) medium level of arc voltage. The measurements performed by the optical microscope, using the objective magnification 20x.

It has to be mentioned that the injected suspension droplet at e.g. maximum voltage enters the plasma jet at maximum level of the signal as well but two periods later. Figure 3.53 a) presents the microstructure of the coating obtained at the maximum level of arc voltage and b) at the medium level. In the picture 3.53 a) and in smaller amount in b) it is possible to observe the dark structures with the diameters up to around $50 \mu\text{m}$, what corresponds to the diameter of the injected droplet. Moreover, as the analysis of the particle size distribution has highlighted, the suspension used in the experiments has the peak of the particle size distribution curve centered on 66 nm (d_{50}) and the dispersion size ($d_{90} - d_{10}$) equal to 48 nm . Therefore, the obtained large micro-metric structures can be the result of the agglomeration of the particles and they have been examined by SEM microscopy. In both coatings microstructures the uniform light area which seems

to be nanometric can be found. Therefore, it has been measured by SEM microscopy as indicated in Figure 3.54.

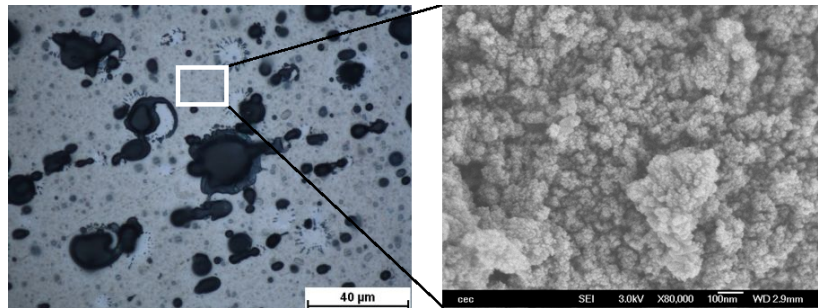


Figure 3.54: Coating obtained at the moment of maximum arc voltage, shown in Figure 3.53, measured by the optical microscope, using the objective magnification 100x, with the marked region measured by SEM and presented on the right.

The result obtained by the scanning electron microscopy measurement highlights that by using the suspension formulated of nano-sized powder particles it is possible to obtain the nano-sized layers of the coatings. However, the diameter of the particles composing this layer is much smaller than the size of TiO_2 powder in the suspension, what might be the result of the material vaporization. Moreover, the obtained layer is very thin. The energy dispersive spectroscopy (EDS) analysis presented the dominant quantity of nickel and chromium from the substrate than titanium from the coating.

In addition to this light zone in the coatings microstructures the dark elements have been found, what is indicated in Figure 3.55. Figure 3.55 presents the distinction of different features appeared in the coating produced at the maximum level of the arc voltage signal.

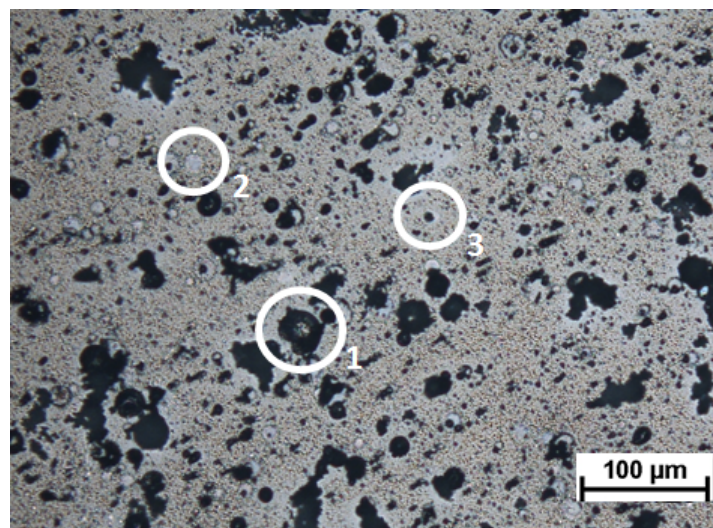


Figure 3.55: Coating obtained at the moment of maximal voltage signal, shown in Figure 3.53, measured by the optical microscope, using the objective magnification 100x, with the indicated features 1), 2), 3) and 4) measured by SEM.

Figure 3.56 shows the main structure appearing in the microstructure given in Figure 3.55. It has been highlighted in Figure 3.53 a) and b) that the diameters of these features are up to around $50\ \mu\text{m}$.

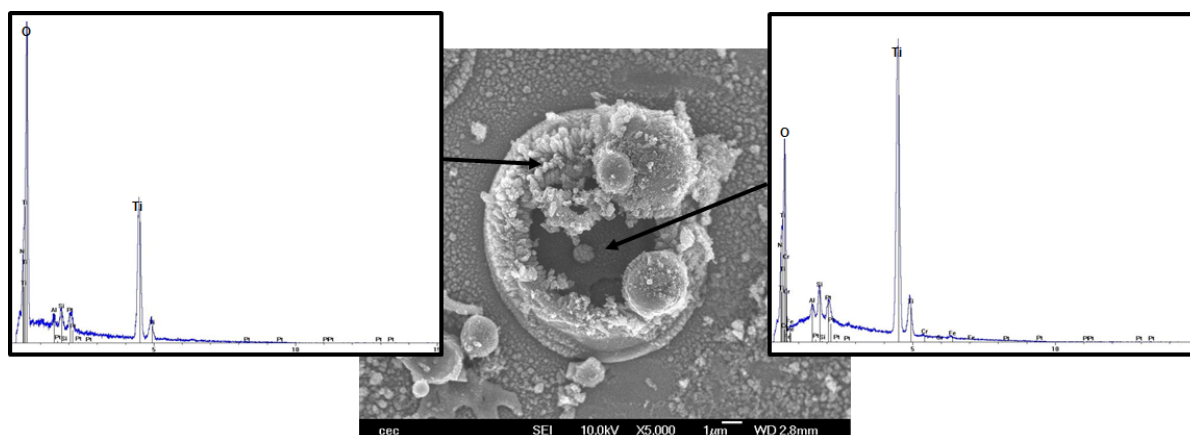


Figure 3.56: Feature 1) from Figure 3.55 measured by the scanning electron microscope and analyzed by EDS.

The measurement by SEM highlights that this structure contains the resolidified and agglomerated particles. The energy dispersive spectroscopy (EDS) analysis shows the interesting characteristic of this splat. The proportion of Ti and O detected in the external part corresponds to stoichiometric TiO_2 , what has been used as the powder to formulate the suspension. However, the measurement of the region inside this structure shows the dominant quantity of Ti.

Figure 3.57 highlights the structure occurring only in the case of the coating obtained at the moment of the maximal level of the arc voltage signal.

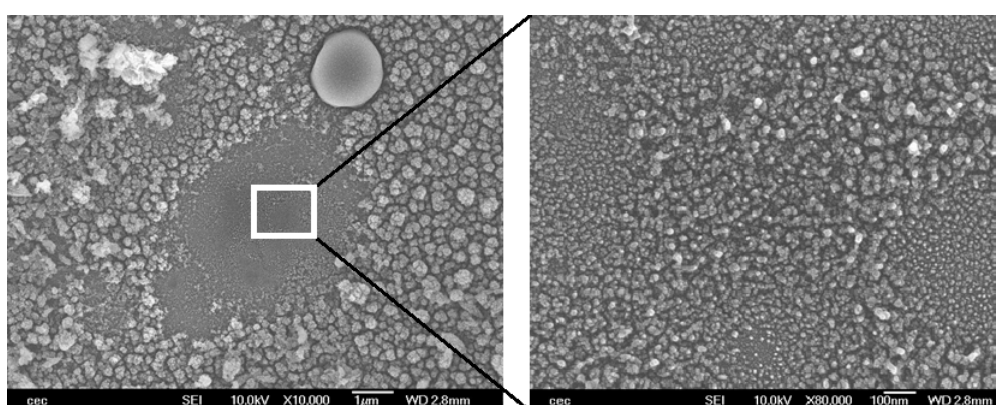


Figure 3.57: Feature 2) from Figure 3.55 measured by the scanning electron microscope.

Under high magnification (right sight of Figure 3.57), nanosized particles, incorporated into this structure, are revealed. The morphology of this feature is non-homogeneous compared to the result shown in Figure 3.58. The shape and the morphology of this

feature resembles the strongly melted or vaporized structure. It may be produced also by the impact of the molten particle on the substrate but the adhesion forces could be too weak to produce the bonding between this particle and the substrate.

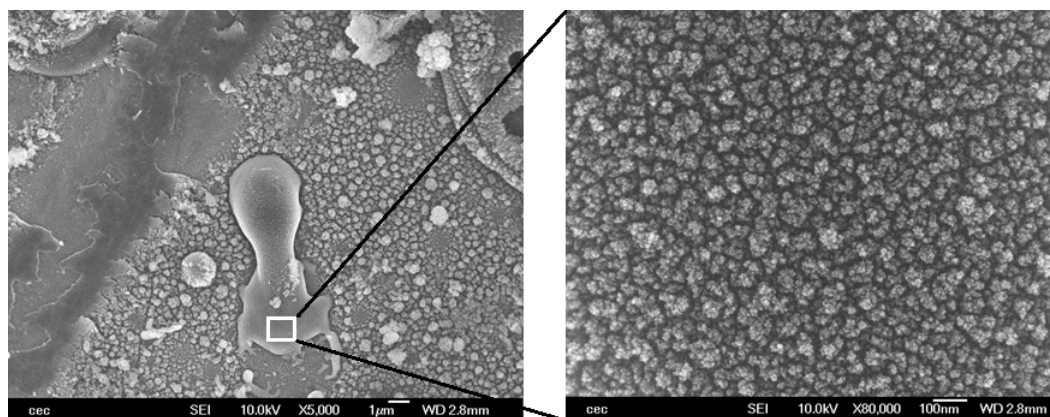


Figure 3.58: Feature 3) from Figure 3.55 measured by the scanning electron microscope.

Figure 3.58 presents the structure of molten particles, what has been found in all obtained coatings, in lower quantities in the case of 3.52 b). The high magnification of this structure has highlighted that it is characterized by homogeneous nano-sized particles.

In the case of the coating produced at the moment of the pulsed plasma corresponding to medium level of the voltage signal, Figure 3.53 b), the features indicated in Figure 3.59, in addition to the structures described above, have been found. They have been analyzed by the scanning electron microscope, what is presented in Figure 3.60.

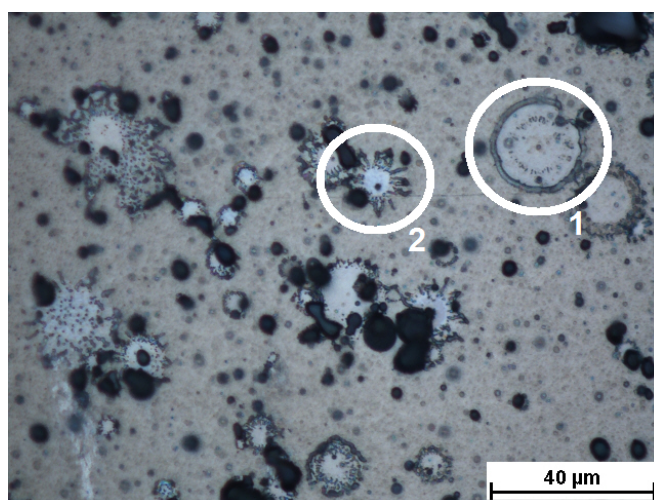


Figure 3.59: Coating obtained at the moment of the medium level of the arc voltage signal, shown in Figure 3.53, measured by the optical microscope, using the objective magnification 100x, with the indicated features 1) and 2) measured by SEM presented in Figure 3.60.

Figure 3.60 1) presents a ring structure with a distinct rim at the periphery. This increase of the material thickness in the external part of this structure may result from recoiling

process of the spread and flattened droplet, what is related to the wetting properties and surface tension of the liquid ceramics.

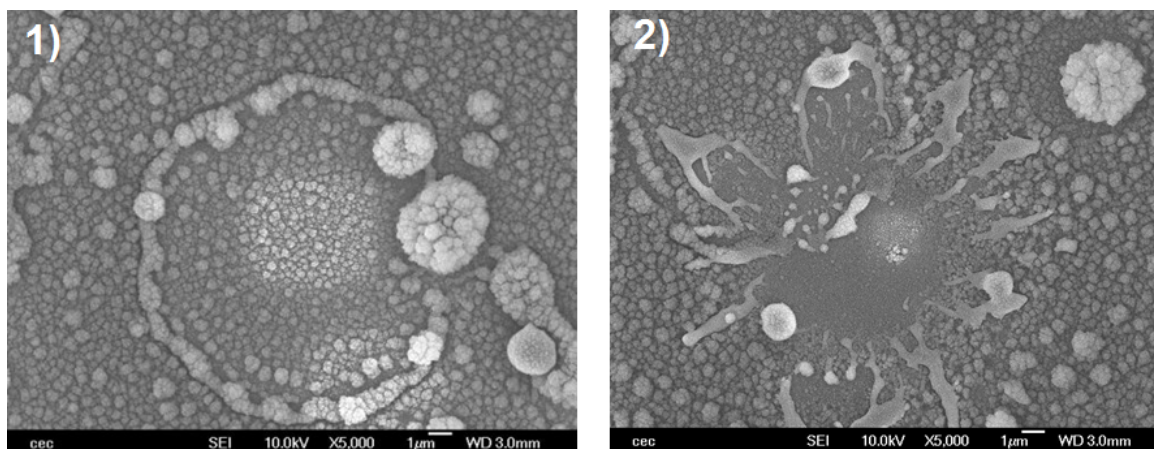


Figure 3.60: Features 1) and 2) from Figure 3.59 measured by the scanning electron microscope.

Figure 3.60 2) exhibits the structure characterized by the finger-like perturbations. The same feature has been observed in all obtained coatings. The studies presented in [102,103] have highlighted the dependence of the splats on the substrate temperature. The splats collected on the low temperature sample are distorted with the shape of the splashed fingers, what exhibits the splashing during droplet impact and spreading. Blazdell *et al.* have shown that preheating the substrate results in much more regular splats, what is presented in Figure 3.61 [46].

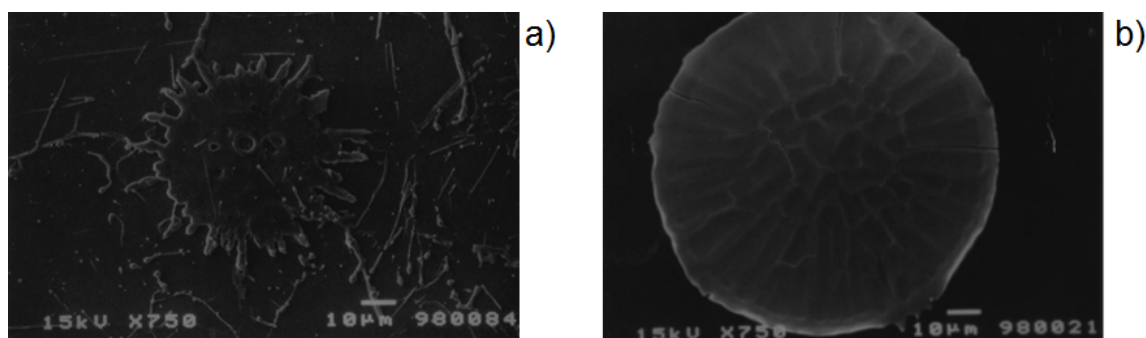


Figure 3.61: Zirconium suspension plasma spraying on a) cold substrate, b) hot substrate [46].

A more regular splat due to the preheating of the substrate might be obtained due to the increase of the solidification rate of the particle.

Moreover, in Figure 3.60 1) and 2) the spherical agglomerated structures with the diameter of around $3 \mu\text{m}$ can be observed. They highlight that in the case of using the plasma with low level of the enthalpy the thermal energy is sufficient to remove the solvent from the suspension droplets but is too low to ensure that they are still molten when they hit

the substrate. Consequently, the drops solidify and agglomerate in flight and land as the balls on the substrate.

The first attempts to produce the coatings by a new system have been highlighted. The results have shown that the choice of the spraying parameters plays the important role in the coatings formation. The spray distance influences on the microstructure of the coating, what has been presented in Figure 3.52. Too long distance has resulted in the observation of the resolidified particles collected on the substrate surface. Moreover, the coatings at the different levels of the pulsed plasma jet have been obtained. The measurements by the optical and scanning electron microscopes have highlighted the occurrence of different features depending on the level of this periodic plasma, thus, the specific enthalpy and temperature levels. The coating obtained at the medium level of the voltage signal has presented the necessity of the preheating of the substrate before the splats collection. However, the microstructure of the coating obtained at the maximal voltage level has not exhibited the structures characterized by the finger-like perturbations, what has to be studied in the future work. In addition, the synchronized suspension with the pulsed plasma has jet has allowed obtaining the coatings features which have not been observed in the conventional suspension plasma spraying. Therefore, the coatings production by a new method requires further investigation.

V Conclusions

The studies of the instabilities of the plasma produced by the conventional dc torch, presented in Chapter 2, have determined the parameters influencing the fluctuations modes, Helmholtz and restrike. It has led to a new approach to plasma fluctuations, the possibility of coupling these two modes together. This is achieved e.g. by the particular design of the plasma torch characterized by large cathode cavity and by using the nitrogen as plasma forming gas. This new resonant mode has been called "mosquito" mode, due to the sharp monotonic sound emitted by the torch, what resembles the noise produced by the mosquito. Therefore, the term "Mosquitorch" has been used to describe a newly designed torch. The plasma, produced in this "mosquito" mode, is a pulsed laminar plasma jet, characterized by the local specific enthalpy modulated with a ratio $h_{\max}/h_{\min} \simeq 18$, what has been presented by the obtained results. Moreover, this pulsed plasma has the modulated velocity and the local temperature, which has been measured by the time-resolved optical emission spectroscopy. This periodic structure of the plasma jet has been used to synchronize the plasma with the suspension injection. The droplets have been ejected using a piezoelectric device, ink-jet printer, triggered by

the voltage signal sampled at the torch connections. To synchronize the plasma jet with the suspension a new synchronization system has been developed. The time-resolved imaging system and time-resolved optical emission spectroscopy have been implemented to observe the moments of this modulated plasma and the interaction between the plasma and the suspension. The results have shown that the trajectories and thermal treatment of the material depend on the moment at which the droplets penetrate the plasma jet. Therefore, the method shows a great possibility of the control of dynamic and thermal interaction between the plasma pulses and the injected material. Moreover, the analysis of thermo-physical phenomena of the inserted material has shown that thermal treatment of the suspension in the plasma jet is governed by the heat transfer and vaporization. The fragmentation process does not occur compared to the conventional methods. Moreover, the first attempts of the coatings production have highlighted the interesting features which have not been observed in the microstructure of the conventional SPS coatings. However, it requires further investigation. First of all, instead of rotating sample holder, the water-cooled support has to be used. Furthermore, the measurement method of the substrate temperature should be applied, e.g. by using the pyrometer. In addition, the obtained coatings presented in this dissertation have highlighted the necessity of the preheating the substrates to obtain regular splats.

Part III

Résumé du chapitre 3

Ce chapitre présente l'application d'oscillations régulières de plasma produites en mode "mosquito" pour le traitement de la suspension et la synthèse de dépôts. Comme cela a été mis en évidence dans les chapitres précédents, la méthode conventionnelle SPS démontre des difficultés dues à l'absence de contrôle des trajectoires des particules et des transferts de chaleur, ce qui rend la maîtrise des propriétés des revêtements. Le but de ce travail est de développer un nouveau système qui peut permettre d'augmenter la reproductibilité et la fiabilité du procédé par l'utilisation des oscillations régulières de plasma synchronisées avec l'injection de la suspension. L'activation de l'émission de la gouttelette de suspension au moment choisi dans le cycle périodique d'oscillation du plasma, suivant les conditions pour le traitement thermique du matériau particulier, peut être capable d'améliorer le contrôle des transferts de chaleur et de quantité de mouvement entre le plasma et les matériaux. Par conséquent, il est important d'optimiser le système qui va permettre de synchroniser l'injection de la suspension avec le signal de tension d'arc. En outre, les différents types de méthodes de diagnostic, résolues en temps et synchronisées, sont nécessaires pour étudier les traitements thermiques et dynamiques de la matière dans le plasma oscillant. Par conséquent, un nouveau système a été développé dans le cadre de cette thèse. Il se compose de trois parties importantes:

I Le système d'imagerie résolue en temps

Il se compose d'une caméra et d'une diode laser pulsée. Cette partie du système nécessite de définir le choix des dispositifs appropriés pour observer et enregistrer le plasma oscillant de période de l'ordre de $700 \mu s$. En outre, des expériences doivent être réalisées pour obtenir la synchronisation de la caméra avec le laser.

II L'injection de suspension synchronisée

Les oscillations périodiques du plasma permettent d'obtenir une nouvelle approche de l'injection d'un matériau dans le jet de plasma d'arc. La goutte de suspension peut être injectée au moment choisi, ce qui peut conduire à la régulation de l'interaction dynamique et thermique entre le plasma et le matériau. Cependant, il nécessite un système d'injection capable de contrôler le moment de l'introduction de la matière dans le plasma. Cette condition a été trouvée dans une imprimante à jet d'encre piézoélectrique fournies par la Société Ceradrop (Limoges, France).

III La spectroscopie résolue en temps

Le chapitre 2 a mis en évidence que le plasma produit dans le mode "Mosquito" est caractérisé par une enthalpie modulée. Pour déterminer expérimentalement cette estimation la spectroscopie d'émission optique résolue en temps a été mise en œuvre. Cette méthode a été utilisée pour prendre les mesures de la température de rotation du plasma et de déterminer les espèces de plasma. Cependant, cette technique nécessite des méthodes d'étalonnage minutieuses, qui sont présentés avec les premières

mesures spectroscopiques du plasma périodique.

Pour observer les oscillations périodiques de plasma obtenues en mode "mosquitio", le système d'imagerie résolue en temps et synchrone a été mis en œuvre. Il se compose d'une caméra rapide, une diode laser de forte puissance et un filtre interférentiel (801 nm). Le laser et le filtre ont été combinés avec la caméra afin de permettre l'observation du traitement de la suspension dans le jet de plasma. Le principe est d'observer la pénétration de la suspension dans le jet de plasma par l'illumination des gouttelettes à l'aide du laser. Le filtre interférentiel (801 nm) centré sur la longueur d'onde de laser permet d'éliminer la lumière du plasma d'azote pur sur l'image. Pour observer les différents moments des oscillations de plasma, l'imagerie résolue en temps doit être synchronisée avec le signal de tension d'arc. De plus, les gouttelettes de suspension doivent être illuminées par le tir du laser lors de l'enregistrement par la caméra. Par conséquent, le laser et la caméra doivent être également synchronisés, ce qui signifie que le temps de réponse, t_d , de chaque dispositif doit être déterminé. Le temps de retard du laser a été déterminé par le fournisseur et égal à 36 ns. Le délai de réponse t_d de la caméra a été défini par l'expérience en utilisant deux générateurs, et est égal à 14 μ s.

Le système d'imagerie résolue en temps doit être synchronisé avec la tension d'arc. Pour obtenir cette synchronisation, le signal TTL est formé à partir de la tension d'arc, qui est mesurée par le pont diviseur connecté entre la cathode de la torche et la masse. Pour générer le signal TTL initial le dispositif de synchronisation est conçu et composé de:

- l'unité d'amplification-filtrage pour isoler la composante de mode de Helmholtz à partir du signal brut, V_{arc} ,
- l'unité de réglage de seuil qui se compose du comparateur pour régler le niveau de déclenchement, $V_{threshold}$,
- la génération de l'impulsion à la fréquence fondamentale, f_H , unité qui produit une impulsion TTL V_s (5 V, 10 μ s). Il permet de générer le signal avec un retard réglable, τ , par rapport au seuil.

Le signal TTL, généré par ce boîtier de synchronisation, par l'ajustement du niveau de seuil et le temps de retard, est ensuite envoyé au panneau de commande Ceradrop. Il génère deux signaux de déclenchement pour activer la caméra et le laser.

Le plasma pulsé a été observé par la caméra déclenché à un moment donné de ce jet périodique. Une période de cycle de tension est d'environ 700 μ s. Le temps d'ouverture de la caméra est réglé à 60 μ s et 75 images sont enregistrées dans chaque situation: à partir de a) à e) de la figure 3.10. L'image a) correspond à un déclencheur de 70 μ s après un front descendant de la tension. Les moments de b) à e) ont été prises avec des retards respectifs: 210, 310, 520 et 770 μ s, ce qui correspond à 70 μ s dans la prochaine

période. La Figure 3.10 a) présente le moment après le réamorçage. L'arc est très court et situé dans la partie arrière de la tuyère. Les photos b) - d) montrent le développement progressif de l'arc et la figure 3.10 e) représente une situation similaire à a), mais pour le cycle suivant. Cette séquence témoigne de la forte modulation du plasma. L'examen de la série des 75 images a montré une évolution très reproductible du plasma dans chaque cycle.

La Figure 3.11 est obtenue avec une caméra standard pour un temps d'exposition de 10^{-2} s, ce qui se traduit par la superposition de 13 cycles présentés dans la figure 3.10. Elle montre la caractéristique laminaire de l'écoulement plasma, ce qui peut être vérifié expérimentalement par le nombre de Reynolds, défini par l'équation (3.4). Le nombre de Reynolds permet de définir différents régimes d'écoulement, tels que l'écoulement laminaire ou turbulent. L'écoulement laminaire se produit à faibles nombres de Reynolds. La transition de l'écoulement laminaire à turbulent commence à propos de $Re > 2100$ et l'écoulement est considéré comme pleinement turbulent à $Re > 4000$. Pour les paramètres du plasma, donnés dans le tableau 2.12, le nombre de Reynolds est estimé à environ 70, ce qui définit l'écoulement laminaire du plasma.

Les oscillations périodiques de plasma nécessitent une méthode d'injection appropriée, capable de contrôler le moment de l'introduction de la matière dans le jet de plasma. L'analyse des différentes techniques d'injection, présentée dans la revue de la littérature dans le chapitre 1, a abouti à la sélection de l'imprimante à jet d'encre piézo-électrique, fourni par Ceradrop (Limoges, France), en raison de la possibilité de l'émission de chaque gouttelette déclenchée à la fréquence du plasma pulsé, c'est à dire 1.4 kHz. L'injecteur de type piézo-électrique avec une éjection de gouttes à la demande (Drop On Demand) a été utilisé. Le liquide est éjecté par de petits orifices (buses de 50 μm de diamètre) grâce à des impulsions de pression appliquées sur le liquide et générées par un matériau piézo-électrique. La déformation de celui-ci est contrôlée par l'application d'une impulsion de tension de l'ordre de 120 volts. La tête d'impression contient 128 buses indépendantes espacées de 0.5 mm et sont commandées par Labview. Les gouttes ont une vitesse variant de 2 à 10 $\text{m}\cdot\text{s}^{-1}$. La fréquence d'éjection peut être ajustée jusqu'à 20 kHz. La formulation de la suspension doit être optimisée en fonction de la nature et la quantité des différents composants (par exemple solvant, dispersant, liant, surfactant) et de la charge massique de matériau céramique afin d'éviter d'une part la sédimentation et le colmatage des buses, et d'autre part d'ajuster les propriétés rhéologiques de la suspension (viscosité, tension de surface).

Le principe de l'injection synchrone de la suspension consiste à injecter des gouttelettes de la matière au bon moment des oscillations périodiques de jet de plasma. Ce processus de synchronisation est possible lorsque la fréquence du mode de résonance de Helmholtz (égale à la fréquence de plasma) est égal à la fréquence de l'injection de la suspension:

$f_H = f_i$. L'émission de la gouttelette est déclenchée par le signal TTL formé à partir de la tension d'arc, en utilisant la boîte de synchronisation.

La suspension utilisée dans les expériences, préparée par Ceradrop (Limoges, France), est composée d'une poudre de dioxyde de titane (90% TiO_2 phases de rutile) et est constituée de 5 wt% de poudre et 95 wt% d'eau. La distribution de taille de particules a été déterminée en utilisant le Mastersizer 2000 (Malvern Instruments Ltd, Royaume-Uni), qui est basé sur la technique de diffraction laser. Le pic de la courbe de distribution de taille de particules de la suspension utilisée dans l'expérience est centré sur 66 nm (d_{50}). La taille de dispersion ($d_{90} - d_{10}$) est égale à 48 nm.

Dans les imprimantes à jet d'encre, la formulation de la suspension doit être optimisée afin d'éviter la sédimentation le bouchage des buses et être compatible avec la tête d'impression. De plus, l'injection d'une seule goutte calibrée est le paramètre important dans ce genre de procédé.

Pour obtenir l'émission d'une seule goutte deux conditions doivent être remplies:

- les propriétés rhéologiques de la suspension (par exemple, la viscosité, la tension de surface) doivent être ajustés pour obtenir le rapport $\text{Re}/\sqrt{\text{We}}$ variant entre 1 et 10
- le signal de tension envoyé à l'injecteur piézo-électrique doit être optimisé

La première condition nécessite la définition du rapport $\text{Re}/\sqrt{\text{We}}$. C'est le coefficient adimensionnel qui permet d'analyser le fluide. Il se compose de respectivement un nombre de Reynolds et Weber, définies par les équations (3.4) et (3.5). Ce rapport calculé pour la suspension utilisés dans les expériences est égale à $\text{Re}/\sqrt{\text{We}} = 5.98$. De plus, pour éliminer les gouttelettes satellites l'impulsion de tension envoyée à l'injecteur a été optimisée en collaboration avec Ceradrop. Une impulsion de tension de forme trapézoïdale, représentée sur la Figure 3.19, a été appliquée.

Ce système, présenté ci-dessus, contenant de l'injecteur, la caméra et le laser synchronisés avec le signal de la tension d'arc a permis d'observer l'injection de la suspension dans les différents moments du jet de plasma pulsé.

Sur la figure 3.23, l'imagerie résolue en temps des interactions dynamiques entre le jet de plasma et les gouttelettes est présentée. Les photos 3.23 a-d sont obtenues avec un objectif à faible grossissement (avec la résolution présentée dans la figure 3.4 c)) pour les différents retards sur une période. Pour obtenir les résultats fiables des centaines de photos liées à 3.23 a-d, déclenchées avec le même temps τ_j , ont été enregistrées. Le laser a été utilisé pour visualiser les particules solides restantes dans le jet après évaporation du solvant. L'analyse d'image a permis d'estimer les vitesses du centre de masse des "boules" de plasma, qui varient entre environ 30 m/s pour le cas présenté dans 3.23 a) et 50 m/s pour 3.23 c). L'expérience a montré sur les figures 3.23 a-d que les trajectoires et l'histoire thermique associée aux matériaux injectés dépend du moment où les gouttelettes

pénètrent dans le plasma. Dans le cas $\tau_1 = 0 \mu s$, la partie la plus importante de matériau voyagent en périphérie de plasma donnant lieu à grande dispersion des trajectoires (~ 10 mm) et la distance axiale de transport des matériaux est limitée ($\sim 40-60$ mm). Dans le cas $\tau_2 = 260 \mu s$, le traitement des matériaux dans le cœur du plasma est amélioré avec une dispersion radiale inférieure et une distance de transport légèrement augmentée. Sur la figure 3.23 c) ($\tau_3 = 480 \mu s$), une faible dispersion de la matière est observée correspondant à la distance de transport plus longue. Enfin, le cas de $\tau_4 = 620 \mu s$ ressemble le premier cas $\tau_1 = 0 \mu s$, car il est presque $700 \mu s$ de période.

Par ailleurs, l'influence du moment où une gouttelette pénètre le jet d'arc pulsé a été étudiée en utilisant la caméra avec l'objectif Infinimax (Figure 3.4 b). Les résultats sont présentés sur la figure 3.24. La caméra et le laser sont retardés par le même temps, après l'émission de gouttelettes mais la suspension pénètrent dans le plasma précédemment sur la figure 3.24 a) que sur b), ce qui a été obtenu en changeant τ_j . La goutte, observée par l'illumination du laser, pénètre dans le plasma 4 mm en aval de la sortie de tuyère. Les images a) et b) sont observées à travers le filtre interférentiel passe-bande centré sur la longueur d'onde du laser. Cette configuration permet d'éliminer la lumière provenant du plasma d'azote pur sur l'image. Par conséquent, la figure 3.24 montre simplement les boules de plasma, caractérisées par une forte augmentation de luminosité résultant de l'interaction du plasma avec le matériau contenu dans la goutte de suspension. Sur la figure 3.24 a) la gouttelette inférieure pénètre dans le plasma à un moment correspondant à une situation présentée sur la figure 3.10 d). Ce moment a été choisi en raison du niveau élevé de l'enthalpie spécifique locale. Par conséquent, la figure 3.24 b) correspond au plasma caractérisé par un faible niveau d'enthalpie, représentée sur la figure 3.10 a). Dans le cas présenté sur la figure 3.24 a), le processus de vaporisation instantanée de la goutte a été observé, ce qui diffère de la situation illustrée en b). Dans ce cas, le processus de vaporisation ne concerne pas la goutte injectée mais celle introduite une période antérieure générant la boule de plasma à droite dans la figure b).

L'effet de modulation de l'enthalpie sur les phénomènes de thermo-physiques des gouttelettes de suspension a été étudié. Le nombre de Weber calculé, dont le processus de fragmentation dépend, est compris entre 0.04 et 0.48. Il s'avère que le procédé de fragmentation n'apparaît pas dans le cas de l'injection de la suspension dans le jet de plasma pulsé. Le calcul du temps de vaporisation a mis en évidence que le choix de la temporisation d'injection peut avoir un effet sur la vaporisation du solvant, ce qui est vérifié par la figure 3.24. Les résultats obtenus par jet de plasma laminaire pulsé montrent la possibilité du contrôle du matériau injecté dans les différentes zones du plasma modulé. Ceci peut permettre de contrôler certains des procédés thermo-physiques se produisant à l'échelle de gouttelette, telles que l'évaporation.

Les paragraphes précédents ont montré que le jet de plasma pulsé est caractérisé par

l'enthalpie spécifique fortement modulée. Pour déterminer cette modulation de façon plus précise et locale, les mesures de température de plasma doivent être effectuées. Parmi toutes les techniques disponibles, la spectroscopie d'émission optique a été choisie. Le spectrographe Isoplane (Princeton Instruments, Trenton, New Jersey) équipé d'une tourelle de 3 réseaux de diffraction (300, 1200 et 2400 tr/mm) a été utilisé. L'acquisition des spectres a été réalisée en utilisant une caméra PI-MAX4 ICCD (Princeton Instruments) connectée à l'ordinateur et commandée par un logiciel LigthField. Pour obtenir des informations précises sur les paramètres du plasma, l'étalonnage du spectromètre a été effectué en longueur d'onde et en intensité.

Pour déterminer la température du plasma, la spectroscopie d'émission optique doit être appliquée pour examiner les espèces du plasma pulsé produit par la "Mosquitorch". L'azote pur (N_2 2 slm) a été utilisé comme le gaz plasmagène, par conséquent, les études spectroscopiques ont mis l'accent sur l'identification des émissions moléculaires de l'azote. L'analyse des espèces, montré sur la figure 3.37, présente que le jet de plasma de 0 à 10 mm contient principalement les transitions du second système positif de $N_2(C - B)$ et du premier système négatif de $N_2^+(B - X)$. Le premier système négatif $B^2 \sum_u^+ - X^2 \sum_g^+$ de l'ion moléculaire azote N_2^+ a été choisi pour mesurer la température de rotation du plasma jusqu'à une distance de 6 mm. Dans le cadre de cette thèse, les spectres mesurés ont été analysés par Specair. Il s'agit d'un logiciel commercial développé pour simuler le rayonnement, les transitions moléculaires et atomiques d'un plasma d'air, y compris les transitions N_2 (C-B) (second système positif), N_2^+ (B-X) (premier système négatif), et le système violet CN. Specair suppose que les états de rotation sont Boltzmann distribués à Trot, définie par l'équation (3.29). Selon Bruggeman *et al.*, cette condition est remplie si la durée de vie effective de l'état excité de N_2 , τ_{eff} , est plus long que le temps de thermalisation de N_2 , τ_{therm} [91], ce qui a été confirmé dans le jet de plasma pulsé par les calculs lorsque les mécanismes de quenching ne sont pas pris en compte. Les résultats ont donné que : $\tau_{\text{therm}} \simeq 10$ ns et $\tau_{\text{eff}} \simeq 80$ ns. Pour définir la température de rotation, T_{rot} , le spectre théorique doit être simulée par Specair et comparé à celui mesuré. Ce procédé comporte plusieurs étapes. Tout d'abord, la soustraction du bruit de fond continu doit être mise en œuvre. En outre, pour obtenir des informations précises sur la température du plasma, l'étalonnage en longueur d'onde et en intensité doivent être effectuées.

Le paramètre important dans la simulation spectrale par le logiciel Specair est la détermination de la fonction d'appareil qui définit la résolution des données obtenues. La fonction de fente d'entrée représente l'élargissement causé par le spectromètre (largeur de la fente, la largeur en pixels, la dispersion réseau). Pour améliorer la précision des mesures spectrales, deux fonctions de fente différentes ont été choisies: la fonction trapézoïdale, proposée dans la [84,94] et présenté dans la figure 3.40, et la fonction déterminée par la mesure d'une lampe au mercure à 404.7 nm.

Pour vérifier les températures des différents pulses de ce plasma modulé, les mesures de spectroscopie résolue en temps doivent être synchronisées avec le signal de tension d'arc. Les délais de déclenchement dans une période de plasma, τ_1 à τ_4 , ont été ajustés par la boîte de synchronisation, comme τ_4 correspond au signal de tension maximale, $U_{\max}(t) = 100$ V, τ_1 a été obtenu à $U(t) \simeq 60$ V. Les signaux TTL générés ont été envoyés à la caméra et au spectrographe. En analysant le premier système négatif de N_2^+ , on peut observer que le spectre mesuré dans l'instant τ_4 est caractérisé par la plus haute valeur de l'intensité en comparant les spectres obtenus à τ_1 de τ_3 . L'estimation spectroscopique de la température de rotation met en évidence que la température du gaz augmente de $6400 \text{ K} \pm 150 \text{ K}$ à $7500 \text{ K} \pm 150 \text{ K}$ en changeant le moment de déclenchement dans la tension d'arc périodique, comme cela est présenté sur la figure 3.46. Les résultats obtenus ont été comparés avec les données de l'enthalpie spécifique du plasma d'azote donné dans [17], ce qui montre que le jet de plasma analysés à l'instant τ_4 est caractérisé par la valeur enthalpie de 35 ± 3 MJ/kg. Pour comparer, au moment τ_1 l'enthalpie est de 15 ± 2 MJ/kg. Il s'avère expérimentalement que le jet de plasma pulsé est caractérisé par l'enthalpie et la température modulée. Cependant, le rapport de la modulation de l'enthalpie, $h_{\tau_4}/h_{\tau_1} \simeq 2.3$, obtenue dans cette expérience est beaucoup plus faible que celle présentée dans la section précédente, $h_{\max}/h_{\min} \simeq 18$, déterminée par les mesures du bilan d'énergie et l'hypothèse sur la tension thermique (36 V) constante. Cette différence significative a conduit à la conclusion que le rapport de la modulation de l'enthalpie de 18 est surestimé parce que les pertes thermiques ne sont pas constantes. L'hypothèse sur les pertes thermiques fluctuantes a donné le ratio h_{\max}/h_{\min} estimé d'environ 2.

Les premiers essais pour produire des revêtements par un nouveau système ont été présentés. Les paramètres de projection ont été choisis comme les paramètres de la méthode SPS conventionnelle:

- La distance de projection de 32 mm de la sortie de la torche
La distance de projection dans APS est de l'ordre de 100 mm. Cependant, Darut *et al.* ont mis en évidence dans la méthode SPS que ce paramètre doit être considérablement réduit à environ 30 mm en raison de l'inertie dynamique et thermique significativement plus faible des particules matérielles [99].
- Le refroidissement du substrat
Un porte-échantillon rotatif a été choisi, ce qui permet d'éviter la surchauffe du substrat. La vitesse linéaire de la porte a été réglée à 1 ms^{-1} , en analysant les études présentées dans [100, 101].
- La préparation du substrat
Pour recueillir les lamelles produites par la méthode SPS, le substrat poli-miroir est

couramment utilisé en raison de sa faible rugosité. Par conséquent, les substrats d'acier inoxydable ont été polis à l'aide du carbure de silicium (SiC) papiers avec les tailles de grain de 600, 1200, 2400 et 4000 μm refroidis à l'eau. Ensuite, la surface du miroir en forme finale a été obtenue en utilisant le pad de polissage en velours et la silice colloïdale. Les substrats avant projection ont été nettoyés à l'éthanol et séché avec le courant d'argon.

Pour produire les revêtements, la suspension aqueuse de TiO_2 , décrit dans le tableau 3.2, a été utilisée. Les caractérisations des revêtements ont été effectuées par la microscopie optique et la microscopie électronique à balayage (SEM en anglais) en combinaison avec la spectroscopie à dispersion d'énergie (EDS), qui donne une analyse de la composition résolue spatialement du revêtement.

La distance de projection de 32 mm a été choisie par l'analyse des résultats obtenus par la méthode SPS. Par conséquent, pour vérifier ce choix, ce paramètre a été augmenté à 42 mm. Les résultats ont montré que la distance de projection influence la microstructure du revêtement, ce qui a été présenté sur la figure 3.52. La distance trop longue a conduit à l'observation des particules resolidifiées recueillies sur la surface du substrat. Pour déterminer l'influence des différents moments du jet de plasma pulsé sur la formation des revêtements, deux cas ont été choisis liés à des mesures spectroscopiques du plasma: l'émission de la suspension au niveau maximum du signal de tension d'arc, présenté sur la figure 3.44 comme τ_4 et le niveau moyen, indiqué sur la figure 3.44 comme τ_1 . Les mesures effectuées par les microscopes optique et électronique à balayage ont mis en évidence la présence des caractéristiques différentes en fonction du niveau de ce plasma périodique, donc, les niveaux d'enthalpie et de température spécifiques. Le revêtement obtenu au niveau moyen du signal de tension a présenté la nécessité du préchauffage du substrat avant la collection des splats. Cependant, la microstructure du revêtement obtenu au niveau de tension maximal n'a pas présenté les structures caractérisées par des perturbations en forme de doigts, qui se trouvent dans le revêtement produit au niveau moyen. En outre, la suspension synchronisée avec le plasma pulsé a permis d'obtenir les caractéristiques des couches qui n'ont pas été observés dans la méthode SPS classique. Par conséquent, la production de revêtements par une nouvelle méthode nécessite l'examen plus approfondi.